QCD ON ANISOTROPIC LATTICES

By

Yannis Trimis

A DISSERTATION

Submitted to
Michigan State University
in partial fulfillment of the requirements
for the degree of

Physics—Doctor of Philosophy

2026

ABSTRACT

TABLE OF CONTENTS

LIST OF ABBREVIATIONS

aHISQ	anisotropic Highly Improved Staggered Quarks
ASQTAD	A-SQuare TADpole-improved
CG	Conjugate Gradient
FHKP	Fabricius-Haan-Kennedy-Pendleton
HISQ	Highly Improved Staggered Quarks
HMC	Hybrid Monte Carlo
IR	Infrared
LCRA	Line of Constant Renormalized Anisotropy
LHS	Left-Hand Side
MSU	Michigan State University
NRQCD	Nonrelativistic Quantum Chromodynamics
QCD	Quantum Chromodynamics
RG	Renormalization Group
RHMC	Rational Hybrid Monte Carlo
RHS	Right-Hand Side
UV	Ultraviolet

CHAPTER 1

INTRODUCTION

CHAPTER 2

QCD ON THE LATTICE

Lattice field theory allows for ab-initio computer simulations of quantum systems that are described by quantum field theories. This is possible because, after rotating to imaginary time, the path integrals that describe the theory resemble a canonical ensemble, which can be sampled with Monte Carlo methods.

2.1 Correlation functions and path integrals

The imaginary (Euclidean) time $\tau \equiv x_4$ is defined as $\tau = it$, where t is the real (Minkowski) time. For simplicity we will work with a theory that describes a real scalar field ϕ. Suppose we are after a 2-point correlation function between to operators, separated by time $t > 0$, say $\mathcal{O}_1(0)$ and $\mathcal{O}_2(t)$. These operators are functions of the fields ϕ. In Minkowski space at zero temperature we would be after:[1]

$$C_0^>(t) := \langle 0|\mathcal{O}_2(t)\mathcal{O}_1(0)|0\rangle = \langle 0|e^{itH}\mathcal{O}_2 e^{-itH}\mathcal{O}_1|0\rangle \tag{2.1}$$

where in the RHS we dropped the $t = 0$ argument and used the Heisenberg picture. By introducing path integrals, we can write this correlation function as:

$$C_0^>(t) = \frac{\int D\phi \mathcal{O}_2(t)\mathcal{O}_1(0)e^{iS[\phi]}}{\int D\phi e^{iS[\phi]}}, \quad t > 0 \tag{2.2}$$

where $S[\phi]$ is the Minkowski action with some interaction parametrized by $V(\phi)$

$$S[\phi] = \int dt d^3x \Big(\frac{1}{2}\partial_\mu\phi\partial^\mu\phi - \frac{m^2}{2}\phi^2 - V(\phi)\Big) \tag{2.3}$$

We assume the mostly-minus Minkowski metric tensor $g_{\mu\nu} = \mathrm{diag}(1, -1, -1, -1)$.

We now rotate to imaginary time, define the theory in a 4-dimensional box whose temporal extent is L_τ, and define the Euclidean correlator:

$$C_E(\tau) = \frac{1}{Z}\mathrm{tr}\Big(e^{-(L_\tau-\tau)H}\mathcal{O}_2 e^{-\tau H}\mathcal{O}_1\Big) \tag{2.4}$$

---

[1] The Wightman function $C^>(t)$ is equal to the usual time-ordered function $C(t)$ for $t > 0$. We use the Wightman function here by specifying $t > 0$ for later convenience.

with $Z = \mathrm{tr}\big(e^{-L_\tau H}\big)$ and H the Hamiltonian that results from the Minkowski action $S[\phi]$. From the knowledge of statistical mechanics of canonical ensembles, we can already identify the temporal extent L_τ of the box as inverse temperature: $L_\tau = 1/T$.

We can express the trace through a full set of eigenstates $|m\rangle$ of H, ordered as $E_0 \leq E_1 \leq E_2 \leq \dots$ and write:

$$C_E(\tau) = \frac{\sum_m \langle m|e^{-(L_\tau-\tau)H}O_2 e^{-\tau H}O_1|m\rangle}{\sum_m \langle m|e^{-L_\tau H}|m\rangle} \tag{2.5}$$

A first observation is that if we take the limit $L_\tau \to \infty$ then the vacuum state $|0\rangle$ dominates and the Euclidean correlator becomes:

$$\lim_{L_\tau\to\infty} C_E(\tau) = \langle 0|e^{\tau H}O_2 e^{-\tau H}O_1|0\rangle \equiv C_0^{>}(-i\tau) \tag{2.6}$$

This relation actually holds for all temperatures: $C_E(\tau) = C^{>}(-i\tau)$, but this is beyond our scope.[2] It is however important to mention that in momentum space Euclidean correlation functions may also be related to time-ordered ones through analytic continuation, thanks to the pole structure of the time-ordered propagators.

On the other hand, as one reads e.g. in [Rothe, 2012], the traces can be expressed as path integrals, and the Euclidean correlator $C_E(\tau)$ can be written as:

$$C_E(\tau) = \frac{\int_{\mathrm{per}} D\phi O_2(\tau)O_1(0)e^{-S_E[\phi]}}{\int_{\mathrm{per}} D\phi e^{-S_E[\phi]}} \tag{2.7}$$

where "per" indicates the periodic boundary condition for the scalar field in the temporal direction: $\phi(\mathbf{x},0) = \phi(\mathbf{x},T)$. For fermionic fields the boundary condition has to be antiperiodic. We furthermore defined the Euclidean action $S_E[\phi]$, which can be obtained from $S[\phi]$ by substituting t by $-i\tau$ and multiplying the resulting expression by i.

The expression (2.7) can be written more generally, for any operator $O = O[\phi]$:

$$\langle O\rangle := \frac{\int_{\mathrm{per}} D\phi O[\phi]e^{-S_E[\phi]}}{\int_{\mathrm{per}} D\phi e^{-S_E[\phi]}} \tag{2.8}$$

---

[2] For more details, see e.g. Chapters 2 and 3 by [Le Bellac, 2011].

This is a fundamental relation for lattice field theory, because it implies that we can generate field configurations $\phi(x)$, defined on a 4-dimensional lattice and weighted by the probability factors:

$$P[\phi] = \frac{1}{Z} e^{-S_E[\phi]}, \tag{2.9}$$

then measure the operator O on each configuration, and finally interpret the average as a Euclidean expectation value. How exactly this is done for the case of QCD we will see in the following sections.

2.2 Extracting energy levels

Let's see how we can extract energy levels from Euclidean correlators $C_E(\tau)$ that we have measured on lattice configurations.

Let $\overline{\Phi}(x)$ be an operator that creates a particle (elementary or composite) with specific quantum numbers from the vacuum, at the Euclidean spacetime position $x = (\mathbf{x}, x_4)$. We will leave the spatial dependence of the operators vague at this point, and return to it later. The Euclidean correlator that we will consider describes the propagation of a particle from imaginary time 0 to τ, and we can express it through Eq. (2.5):

$$\begin{aligned} \langle \Phi(\tau)\overline{\Phi}(0)\rangle &= \frac{\sum_m \langle m|e^{-(L_\tau-\tau)H}\Phi e^{-\tau H}\overline{\Phi}|m\rangle}{\sum_m \langle m|e^{-L_\tau H}|m\rangle} \\ &= \frac{\sum_{m,n} \langle m|e^{-(L_\tau-\tau)H}\Phi|n\rangle\langle n|e^{-\tau H}\overline{\Phi}|m\rangle}{\sum_m \langle m|e^{-L_\tau H}|m\rangle} \end{aligned} \tag{2.10}$$

where in the second line we inserted a resolution of identity in the numerator. Now we can expand numerator and denominator. For the denominator we will have:

$$\sum_m \langle m|e^{-L_\tau H}|m\rangle = e^{-E_0 L_\tau} + e^{-E_1 L_\tau} + e^{-E_2 L_\tau} + \dots \tag{2.11}$$

and for the numerator:

$$
\begin{aligned}
\sum_{m,n} \langle m| e^{-(L_\tau-\tau)H} \Phi |n\rangle \langle n| e^{-\tau H} \overline{\Phi} |m\rangle = {} & A_{00}\overline{A}_{00} e^{-L_\tau E_0} + A_{10}\overline{A}_{01} e^{-(L_\tau-\tau)E_1-\tau E_0} \\
& + A_{01}\overline{A}_{10} e^{-(L_\tau-\tau)E_0-\tau E_1} + A_{11}\overline{A}_{11} e^{-L_\tau E_1} \\
& + A_{20}\overline{A}_{02} e^{-(L_\tau-\tau)E_2-\tau E_0} + A_{02}\overline{A}_{20} e^{-(L_\tau-\tau)E_0-\tau E_2} \\
& + A_{21}\overline{A}_{12} e^{-(L_\tau-\tau)E_2-\tau E_1} + A_{12}\overline{A}_{21} e^{-(L_\tau-\tau)E_1-\tau E_2} \\
& + A_{22}\overline{A}_{22} e^{-L_\tau E_2} + \ldots
\end{aligned}
\tag{2.12}
$$

where we used the following notation for the amplitudes:

$$
A_{mn} = \langle m|\Phi|n\rangle, \quad \overline{A}_{mn} = \langle m|\overline{\Phi}|n\rangle \tag{2.13}
$$

The next step is to factor out the quantity $e^{-E_0 L_\tau}$ from numerator and denominator of Eq. (2.10). The vacuum energy E_0 is not an observable quantity, and only differences between this and energy levels of states have phyisical sense. We will call these differences $\Delta E_m = E_m - E_0$. Then Eq. (2.10) becomes:

$$
\langle \Phi(\tau)\overline{\Phi}(0)\rangle = \frac{A_{00}\overline{A}_{00} + A_{10}\overline{A}_{01} e^{-\Delta E_1 (L_\tau-\tau)} + A_{01}\overline{A}_{10} e^{-\Delta E_1 \tau} + \ldots}{1 + e^{-\Delta E_1 L_\tau} + \ldots} \tag{2.14}
$$

Finally, we can get rid of the factors like $A_{00}\overline{A}_{00}$ be considering only the connected part of our correlator, defined as:

$$
\langle \Phi(\tau)\overline{\Phi}(0)\rangle_c = \langle \Phi(\tau)\overline{\Phi}(0)\rangle - \langle \Phi\rangle\langle\overline{\Phi}\rangle \tag{2.15}
$$

This is true for temporal extents such that $\Delta E_n L_\tau \ll 1$.

We can also observe that terms that correspond to matrix elements between non-vacuum states, e.g. m and n, are suppressed compared to terms that couple the vacuum to these states, by terms proportional to $e^{-\Delta E_n L_\tau}$, if $E_n \leq E_m$.

If we now specify[3] that $\overline{\Phi} = \Phi^\dagger$, we can see that our connected correlator can be written as:

$$
\langle \Phi(\tau)\Phi^\dagger(0)\rangle_c = \sum_m |A_{0m}|^2 \Big(e^{-\Delta E_m \tau} + e^{-\Delta E_m (L_\tau-\tau)} \Big) \tag{2.16}
$$

---

[3] This can be done for fermions too, by using invariance of the correlator under charge conjugation, as we will see later.

The ground state, i.e. the one with $m = 1$, corresponds to the desired particle state by construction of the operator Φ, and the excited states with $m > 1$ are states that have quantum numbers compatible with Φ. Among these, one can at times detect some multiparticle scattering state.

2.3 An action for lattice QCD

The color degree of freedom in the description of the strong interaction came as a necessity in the 1960s, in order to describe phenomena in baryon spectroscopy, such as the existence of the Δ^{++} resonance. The reasoning behind the introduction of the Lie group $SU(3)_c$– c standing for color– as the correct local symmetry group to accommodate the color dynamics can be found, for example, in Chap. 14 of [Aitchison and Hey, 2013].

The continuum QCD action contains gluonic fields A transforming in the adjoint representation of $SU(3)_c$ and quark 4-spinors ψ transforming in the fundamental representation of $SU(3)_c$. It also contains a bare coupling g and bare quark masses m_i. We will jump right to the Euclidean formulation, since this will be relevant for lattice discretization. The continuum action can be broken into a gluonic and a fermionic part:

$$S[\psi,\bar{\psi},A] = S_G[A] + S_F[\psi,\bar{\psi},A] \tag{2.17}$$

where:

$$S_G[A] = \frac{1}{4}\int d^4x F^a_{\mu\nu}(x)F^a_{\mu\nu}(x) \tag{2.18}$$

and, with i counting the flavors of quarks:

$$S_F[\psi,\bar{\psi},A] = \int d^4x \sum_i \bar{\psi}_i(x)\Big(\gamma_\mu D_\mu + m_i\Big)\psi_i(x) \tag{2.19}$$

The latin index a is associated with color. The covariant derivative $D_\mu(x)$ is defined as:

$$D_\mu(x) = \partial_\mu + igA^a_\mu(x)T^a \tag{2.20}$$

with T^a being the generators of $SU(3)$, defined through Gell-Mann matrices, and the field strength F is defined as:

$$F^a_{\mu\nu}(x) = \partial_\mu A^a_\nu(x) - \partial_\nu A^a_\mu(x) - f^{abc}A^b_\mu(x)A^c_\nu(x) \tag{2.21}$$

by use of the structure constants f^{abc} of $SU(3)$. This action is invariant under $SU(3)_c$ transformations, which can be parametrized as $\Omega(x) = \exp(i\theta^a(x)T^a)$. With infinitesimal real parameters $\theta^a(x)$, these transformations act on the quark fields in the following way:

$$\psi(x) \longrightarrow \Omega(x)\psi(x) = \big(1 + i\theta^a(x)T^a + O(\theta^2)\big)\psi(x) \tag{2.22}$$

$$\bar{\psi}(x) \longrightarrow \bar{\psi}(x)\Omega^\dagger(x) = \bar{\psi}\big(1 - i\theta^a(x)T^a + O(\theta^2)\big) \tag{2.23}$$

and, of course, the action of $\Omega(x)$ on the gauge field $A^a_\mu(x)$ follows from the above and from the invariance of the action. We find:

$$A^a_\mu(x) \longrightarrow \Omega(x) * A^a_\mu(x) = A^a_\mu(x) - \frac{1}{g}\partial_\mu\theta^a(x) + A^a_\mu(x)\theta^b(x)f^{abc} + O(\theta^2) \tag{2.24}$$

where we introduced the action of $\Omega(x)$ on the gauge field with an abstract notation $*$, for now. We can introduce the $su(3)_c$ algebra element $A_\mu(x)$ as:

$$A_\mu(x) = \sum_a A^a_\mu(x)T^a \tag{2.25}$$

Its gauge transformation law is:

$$A_\mu(x) \longrightarrow \Omega(x)A_\mu(x)\Omega^\dagger(x) + i\big(\partial_\mu\Omega(x)\big)\Omega^\dagger(x) \tag{2.26}$$

With it we can show that the field strength tensor, which can now be written as:

$$F_{\mu\nu}(x) = \partial_\mu A_\nu(x) - \partial_\nu A_\mu(x) + ig[A_\mu(x), A_\nu(x)] \tag{2.27}$$

and the covariant derivative transform in a covariant fashion:

$$F_{\mu\nu}(x) \longrightarrow \Omega(x)F_{\mu\nu}(x)\Omega^\dagger(x) \tag{2.28}$$

$$D_\mu(x) \longrightarrow \Omega(x)D_\mu(x)\Omega^\dagger(x) \tag{2.29}$$

Since lattice simulations do not depend on some weak coupling expansion, we need not renormalize this action nor fix the gauge, introduce ghosts and so on. We can, in principle, discretize this action and perform simulations.

It is convenient to absorb the coupling g in the gauge fields $A_\mu^a(x)$, because by doing so the coupling becomes a prefactor of the gauge action. Specifically, if:

$$gA_\mu^a(x) = A'^a_\mu(x) \tag{2.30}$$

We see, by the way, that the noninteracting limit of the theory corresponds to $A'^a_\mu(x) = 0$ everywhere. Anyways, the field strength becomes:

$$\begin{aligned} F_{\mu\nu}^a(x) &= \frac{1}{g}\left[\partial_\mu A'^a_\nu(x) - \partial_\nu A'^a_\mu(x) - f^{abc} A'^b_\mu(x) A'^c_\nu(x)\right] \\ &= \frac{1}{g} F'^a_{\mu\nu}(x) \end{aligned} \tag{2.31}$$

and the gauge action becomes:

$$S_G[A] = \frac{1}{4g^2}\int d^4x F'^a_{\mu\nu}(x) F'^a_{\mu\nu}(x) \tag{2.32}$$

or, using $F_{\mu\nu}(x)$:

$$S_G[A] = \frac{1}{2g^2}\int d^4x \, \mathrm{tr}\big(F'_{\mu\nu}(x) F'_{\mu\nu}(x)\big) \tag{2.33}$$

where the trace is taken in the 3 × 3 color space. We will drop the primes from now on.

2.3.1 The fermion action and the need for gauge links

Discretizing S_G and S_F requires, first of all, the introduction of a 4-dimensional lattice with some lattice spacing a. We consider a lattice Λ with number of points (i.e. volume) equal to $|\Lambda| = N_x N_y N_z N_\tau$.

The discretization imposes a UV-cutoff of $\sim \pi/a$ on any loop momenta. Let us start with the fermion action S_F. We define the fermion fields on discrete points $x = (\mathbf{n}a, n_4 a)$ with integer n_μ. Because of discretzation, we have substituted the rotational symmetry of the continuum action by some hypercubic symmetry, but it can be shown that lattice correlation functions satisfy the original continuum rotational symmetry at the $a \longrightarrow 0$ limit. However, we cannot give up on gauge invariance, which should be exact even at finite a. The requirement of gauge invariance for S_F leads us to build the action using gauge links U:

$$U_\mu(x) = e^{iaA_\mu(x)} \tag{2.34}$$

and since $A_\mu(x)$ belong to the $su(3)_c$ algebra, the links belong to the $SU(3)_c$ group.

The noninteracting limit of the theory corresponds to $U_\mu(x) = 1_3$ everywhere. One can show that, based on the gauge transformation law of $A_\mu(x)$ of Eq. (2.26), the links $U_\mu(x)$ transform under Ω gauge transformations as:

$$U_\mu(x) \to \Omega(x) U_\mu(x) \Omega^\dagger(x+\hat{\mu}) \tag{2.35}$$

Therefore, any operator built as:

$$\bar{\psi}(x) C[U](x,y) \psi(y) \tag{2.36}$$

with $C[U](x,y)$ being a chain of links that connects the lattice point x with the lattice point y, is gauge invariant. The links, if the lattice is thought as embedded in a 4-dimensional space, are in fact gauge transporters.

Anyway, our naively discretized fermion action for one flavor is:

$$\begin{gathered} S_F[\bar{\psi},\psi,U] = \\ a^4 \sum_{x,y} \bar{\psi}(x) \Big(\sum_\mu \gamma_\mu \frac{U_\mu(x)\delta^{(4)}(y-x-\hat{\mu}) - U_\mu^\dagger(x-\hat{\mu})\delta^{(4)}(y-x+\hat{\mu})}{2a} + m\delta^{(4)}(x-y) \Big) \psi(y) \end{gathered} \tag{2.37}$$

If one expands this in a and takes the limit $a \to 0$, one retrieves the continuum action of (2.19). However, this action is not suitable for simulations, since it describes not 1, but 16 quarks. This is due to what is called doubling problem, and it can be seen through the free quark propagator in momentum space. Let $M_0(x,y)$ be the kernel of the free action $S_{F,0}[\bar{\psi},\psi]$:

$$M_0(x,y) = \sum_\mu \gamma_\mu \frac{\delta^{(4)}(y-x-\hat{\mu}) - \delta^{(4)}(y-x+\hat{\mu})}{2a} + m\delta^{(4)}(x,y) \tag{2.38}$$

From this we can define the momentum space kernel $M_0(p)$:

$$M_0(x,y) = \int_{-\pi/a}^{\pi/a} \frac{d^4p}{(2\pi)^4} K_0(p) e^{ip\cdot(x-y)} \tag{2.39}$$

such that:

$$S_{F,0}[\bar{\psi},\psi] = \int_p \int_q \bar{\psi}(p) \delta_P^{(4)}(p-q) M_0(p) \psi(q) \tag{2.40}$$

where $\delta_P^{(4)}$ is the 2π-periodic 4-dimesnional delta function.

From (2.39) we can find $M_0(p)$ by use of (2.38) and:

$$\delta(x-y) = a\int_{-\pi/a}^{\pi/a} \frac{dp}{2\pi} e^{ip\cdot(x-y)} \tag{2.41}$$

We find:

$$M_0(p) = \frac{i}{a}\sum_\mu \gamma_\mu \sin(ap_\mu) + m \tag{2.42}$$

which leads to a free quark propagator $G_0(p) = M_0^{-1}(p)$:

$$G_0(p) = \frac{-i\sum_\mu \gamma_\mu \sin(ap_\mu)/a + m}{\sum_\mu \sin^2(ap_\mu)/a^2 + m^2} \tag{2.43}$$

The doubling can be seen in the fact that if we take $m \longrightarrow 0$ then $G_0(p)$ has $2^4 = 16$ poles; for $p = (0,0,0,0)$ and for all the 15 positive corners of the Brillouin zone: $p = (\pi/a, 0, 0, 0)$, $(0, \pi/a, 0, 0)$ and so on. The doubling is essentially a consequence of the Dirac equation being of first order.

People have devised several ways to overcome the doubling problem and perform lattice simulations and measurements involving fermions. Perhaps the two most popular ones are the Wilson fermions [Wilson, 1975] and the Kogut-Susskind staggered fermions [Kogut and Susskind, 1975].

In the case of Wilson fermions, a dimension-5 operator[4] is added to S_F, which is chosen so that the doublers, i.e. all the poles except the one at $(0,0,0,0)$, become infinitely heavy as $a \longrightarrow 0$. The addition of that operator explicitly breaks the chiral symmetry of S_F.

In the case of staggered fermions, by means of a local transformation, the degeneracy is reduced from 16-fold to 4-fold. The result is an action that involves 1-component spinors $\chi(x)$, $\bar{\chi}(x)$, has therefore no gamma matrices but phases $\eta_\mu(x)$ and retains a subgroup of the original chiral symmetry group. The staggered action reads:

$$S_F[\chi,\bar{\chi},U] = \frac{1}{2}\sum_{x,\mu} \eta_\mu(x)\bar{\chi}(x)\big(U_\mu(x)\chi(x+\hat{\mu}) - U_\mu^\dagger(x-\hat{\mu})\chi(x-\hat{\mu})\big) + m\sum \bar{\chi}(x)\chi(x) \tag{2.44}$$

where

$$\eta_\mu(x) = (-1)^{\sum_{\nu<\mu} x_\nu} \tag{2.45}$$

---

[4] This means an operator which in physical units is proportional to a^5 and therefore vanishes as $a \longrightarrow 0$. In RG language, this is an irrelevant operator.

and the transformation from the naive action reads:

$$\psi(x) = \gamma_1^{x_1}\gamma_2^{x_2}\gamma_3^{x_3}\gamma_4^{x_4}\chi(x), \quad \bar{\psi}(x) = \bar{\chi}(x)\gamma_4^{x_4}\gamma_3^{x_3}\gamma_2^{x_2}\gamma_1^{x_1} \tag{2.46}$$

Up to some improvements, which will be introduced in Chap. 3, and the introduction of anisotropy, this is the action that we use for the quark sector in our simulations. Although all lattice fermion types have their advantages, the main reason to work with staggered fermions is their low computational cost, since they involve 1-component spinors and do not involve extra parameters, as in the Wilson case, that need to be tuned.

Another reason to work with staggered fermions is related to the remnant chiral symmetry of the staggered action. It leads to the existence of a massless Goldstone boson (in the $m = 0$ case) and to exclusively multiplicative renormalization of the quark mass– which has an additive component with Wilson fermions. This makes simulations at low quark masses easier and makes staggered fermions a more natural choice for the study of phenomena dominated by the chiral properties of quarks.

2.3.2 The gauge action

The gauge action S_G should, because of the gauge invariance obligation, be built out of gauge links. We observe that, because of the link gauge tranformation law (2.35), any closed loop made of links is gauge invariant. We can use the elementary loop, also called plaquette, to build an action. This is the first action ever used for a lattice gauge theory and is due to Wilson [Wilson, 1974].

We define the plaquette $P_{\mu\nu}(x)$ as:

$$\begin{aligned} P_{\mu\nu}(x) &= U_\mu(x)U_\nu(x+\hat{\mu})U_{-\mu}(x+\hat{\mu}+\hat{\nu})U_{-\nu}(x+\hat{\nu}) \\ &= U_\mu(x)U_\nu(x+\hat{\mu})U_\mu^\dagger(x+\hat{\nu})U_\nu^\dagger(x) \end{aligned} \tag{2.47}$$

where we used that

$$U_{-\mu}(x) = U_\mu^\dagger(x-\mu) \tag{2.48}$$

We can write the plaquette action as:

$$S_G[U] = \frac{6}{g^2}\sum_{x,\mu<\nu}\left(1 - \frac{1}{3}\mathrm{ReTr}P_{\mu\nu}(x)\right) \tag{2.49}$$

If we expand the links in the plaquette around $a = 0$:

$$U_\mu(x) = 1 + iaA_\mu(x) - \frac{a^2}{2}A_\mu^2(x) + O(a^3) \tag{2.50}$$

and interpret fields at neighboring points through Taylor expansions:

$$A_\mu(x + \hat{\nu}) = A_\mu(x) + a\partial_\nu A_\mu(x) + O(a^2) \tag{2.51}$$

we can then show, using the definition (2.27), that the plaquette action becomes:

$$S_G[U] = \frac{a^4}{2g^2}\sum_{x,\mu,\nu} \operatorname{tr}\big(F_{\mu\nu}(x)F_{\mu\nu}(x)\big) + O(a^2) \tag{2.52}$$

which is the action of Eq. (2.33) plus $O(a^2)$ corrections.

2.3.3 The continuum limit and the improvement of the gauge action

The lattice spacing a is not an input for simulations. Fields and parameters are redefined by absorbing powers of a, so that all become dimensionless and so that the lattice action is not a function of the lattice spacing. For example, from Eqs. (2.37) and (2.34):[5]

$$\hat{\psi}(x) = a^{3/2}\psi(x) \tag{2.53}$$

$$\hat{\bar{\psi}}(x) = a^{3/2}\bar{\psi}(x) \tag{2.54}$$

$$\hat{A}^a_\mu(x) = aA^a_\mu(x) \tag{2.55}$$

$$\hat{m} = am \tag{2.56}$$

$$\hat{g} = g \tag{2.57}$$

It has to be noted that g, being a renormalizable coupling in QCD, has mass dimension equal to 0.

In the case of QCD specifically, exactly because it is a physical theory, a lattice simulation at some bare parameters, say g and $\hat{m}$,[6] and a measurement of exactly two observables $\hat{O}_1 = \hat{O}_1(g, \hat{m})$ and $\hat{O}_2 = \hat{O}_2(g, \hat{m})$ can lead to the extraction of a and the tuning of $\hat{m}$ through:

$$a^{-d_1}\langle\hat{O}_1(g, \hat{m})\rangle = O_{1,ph} \quad a^{-d_2}\langle\hat{O}_2(g, \hat{m})\rangle = O_{2,ph} \tag{2.58}$$

---

[5] We will usually omit the hats in the following sections and chapters. It should be deduced by the context whether lattice or physical units are used.

[6] If there were no quark masses, then only one measurement would suffice for tuning. But since in our simulation we dealt with quark masses and anisotropies (to be defined later), it was decided that a not-so-trivial example is in order.

where $d_{1(2)}$ the mass dimension of $\hat{O}_{1(2)}(g, \hat{m})$, and $O_{1,ph},\ O_{2,ph}$ the physical obervables, extracted from e.g. experiment. The process of determining the lattice spacing is known as scale setting, and the process of determining the bare parameters of the action to achieve specific values for observables is known as tuning. We will revisit it in Chap. 5 where we will discuss it in the case of our simulations.

The fact that at $a \longrightarrow 0$ our lattice actions give the continuum QCD action does not guarantee that the results of our lattice simulations, when extrapolated to $a = 0$, will give continuum QCD results. The existence of the continuum limit and its coincidence with continuum QCD is a nontrivial matter, closely related to the Renormalization Group (RG) characteristics of the theory in study, in this case QCD.

Let M be the lowest mass in the spectrum of the lattice theory. For M to remain finite at $a \longrightarrow 0$ and resemble some continuum mass, the dimensionless mass $\hat{M} = aM$ should vanish at $a \longrightarrow 0$, which means that the associated correlation length ξ, along with all other correlation lengths of our lattice theory, which in essence is a classical statistical system, should diverge at $a \longrightarrow 0$. Therefore, the existence of a continuum limit implies the existence of a critical point for the lattice theory.

From an RG perspective, the existence of a continuum limit implies the existence of a fixed point. More specifically, the existence of a single UV fixed point means that all latice actions with the correct naive $a \longrightarrow 0$ limit will collapse to the same continuum action as one approaches the UV fixed point.

This is the case of QCD: the fixed point corresponds to zero bare coupling, $g = 0$, because of asymptotic freedom, and therefore the continuum limit of QCD is approached when one dials $g \longrightarrow 0$.

It has to be noted that other theories, such as the scalar ϕ^4 or the $U(1)$ gauge theory do not have similarly simple RG structure, and extracting continuum physics from lattice simulations is a difficult task and an open question.

Back to QCD. Let us ignore the quark masses and consider an observable $\Theta = \Theta(g, a)$. We can assume that for small enough a, its expectation value will approach the physical value Θ_{ph} in a flat fashion:

$$\langle\Theta(g,a)\rangle = \Theta_{ph}, \quad \text{for } a \longrightarrow 0 \tag{2.59}$$

This means that in that regime we can write:

$$\begin{aligned} \frac{d}{da}\langle\Theta(g,a)\rangle &= 0 \\ \Rightarrow \Big(\frac{\partial}{\partial a} + \frac{\partial g}{\partial a}\frac{\partial}{\partial g}\Big)\langle\Theta(g,a)\rangle &= 0 \\ \Rightarrow \Big(a\frac{\partial}{\partial a} - \beta(g)\frac{\partial}{\partial g}\Big)\langle\Theta(g,a)\rangle &= 0 \end{aligned} \tag{2.60}$$

where the beta function $\beta(g)$ is defined as:

$$\beta(g) = -a\frac{\partial g}{\partial a} \tag{2.61}$$

We can expand $\beta(g)$:

$$\beta(g) = -\beta_0 g^3 - \beta_1 g^5 + \dots \tag{2.62}$$

where β_0, i.e. the 1-loop coeffiecient, is universal (independent of scheme) and equal to $11/(16\pi^2)$ in the case of no quarks.[7] We can then expand $\langle\Theta(g,a)\rangle$ around $g = 0$ and by integrating Eq. (2.60) we can get an expression for $a(g)$:

$$a = \frac{1}{\Lambda_L}\big(\beta_0 g^2\big)^{-\beta_1/(2\beta_0^2)} e^{-1/(2\beta_0 g^2)}\big(1 + O(g^2)\big) \tag{2.63}$$

where Λ_L is an integration constant, with units of mass, and is an RG invariant. It is inherent to the $SU(3)_c$ theorya and, even in the absence of massive quarks, Λ_L provides a scale. It is related to equivalent continuum RG integration constants, such as Λ_{QCD} in the case of full continuum QCD. For more details see Chapters 9 and 15 of [Rothe, 2012], and Chapters 3 and 5 of [Montvay and Munster, 1997].

Eq. (2.63) has another important use for lattice practitioners: In the scaling regime, i.e. in the regime of couplings where the assumption (2.59) holds, (2.63) allows for fits of lattice observables against the coupling g (see [Allton, 1997]).

---

[7] β_1 is also universal if the quarks are massless.

In the light of all that, we can talk about improving a lattice setup in order to suppress the discretization effects and cause a measurement result to be closer to continuum. Naively, one would take an action, say the plaquette gauge action of Eq. (2.49), and try to remove the $O(a^2)$ errors. This is correct, but it is not the whole story.

As was pointed out in [Symanzik, 1983], and in [Weisz, 1983] for the case of gauge theories, Eq. (2.60) should be corrected:

$$\left(a\frac{\partial}{\partial a} - \beta(g)\frac{\partial}{\partial g}\right)\langle\Theta(g,a)\rangle = O\left(a^2\Lambda_L^2 \log a\Lambda_L\right) \tag{2.64}$$

Therefore improvement in reality means suppressing the corrections of the RHS of (2.64). In order to achieve that, one has to add higher-dimension operators O_i to the lattice action, expand $\Theta(g,a)$ around $g = 0$ and tune the coefficients c_i of the operators O_i in the action so that discretization errors of $\langle\Theta(g,a)\rangle$ vanish order by order in g. This procedure is usually referred to as Symanzik improvement program.

In the case of the $SU(3)_c$ gauge action, the improvement was studied at leading and next-to-leading order, that is, at tree-level and at 1-loop order, in [Weisz, 1983], [Weisz and Wohlert, 1984] and [Luscher and Weisz, 1985]. At tree level in particular, as shown in the above papers and discussed in a simpler language in [Lepage, 1997], one does not even have to consider an observable; It suffices to add rectangular Wilson loops, which are of dimension 6, to the plaquette action in order to suppress the $O(a^2)$ errors, and it can be shown that this way a number of observables, like e.g. the static potential, are improved at tree level. This corresponds to a classical improvement to the theory. The resulting action is the tree-level Symanzik-improved gauge action:

$$S_G[U] = \frac{6}{g^2}\sum_{x,\mu<\nu}\left(1 - \frac{1}{3}\mathrm{ReTr}\left(c_0 P_{\mu\nu}(x) + c_1 R_{\mu\nu}(x) + c_1 R_{\nu\mu}(x)\right)\right) \tag{2.65}$$

where $R_{\mu\nu(x)}$ and $R_{\nu\mu}(x)$ are the two different orientations for rectangles at given x and directions μ, ν. The coefficients are:

$$c_0 = \frac{5}{3}, \quad c_1 = -\frac{1}{12} \tag{2.66}$$

Up to the introduction of anisotropy, this is the action that we use for the gauge sector in our simulations.

2.4 Meson spectroscopy

2.4.1 Meson correlators in QCD and the quenched approximation

The expectation value of any observable $A[\psi, \bar{\psi}, U]$ on the lattice can be separated into a fermionic and a gauge part, that is, every path integral can be performed sequentially; first the quark integration, and then the link integration. Symbolically, this can be written as:[8]

$$\langle A[\psi, \bar{\psi}, U] \rangle = \langle \langle A[\psi, \bar{\psi}, U] \rangle_F \rangle_G \tag{2.67}$$

But let's look into this with more detail. From Eq. (2.7) we can write:

$$\begin{aligned} \langle A[\psi, \bar{\psi}, U] \rangle &= \frac{\int DUD\bar{\psi}D\psi A[\psi, \bar{\psi}, U] e^{-S_G[U]-S_F[\psi,\bar{\psi},U]}}{\int DUD\bar{\psi}D\psi e^{-S_G[U]-S_F[\psi,\bar{\psi},U]}} \\ &= \frac{1}{Z} \int DU e^{-S_G[U]} \langle A[\psi, \bar{\psi}, U] \rangle_F Z_F[U] \end{aligned} \tag{2.68}$$

where:

$$Z = \int DUD\bar{\psi}D\psi e^{-S_G[U]-S_F[\psi,\bar{\psi},U]} \tag{2.69}$$

$$Z_F[U] = \int D\bar{\psi}D\psi e^{-S_F[\psi,\bar{\psi},U]} \tag{2.70}$$

$$\langle A[\psi, \bar{\psi}, U] \rangle_F = \frac{1}{Z_F[U]} \int D\bar{\psi}D\psi A[\psi, \bar{\psi}, U] e^{-S_F[\psi,\bar{\psi},U]} \tag{2.71}$$

The fermionic path integrals (2.70) and (2.71) can usually be performed analytically, which is possible because of the quadratic form of the fermionic action even in the interacting case. Then, the gauge part is performed with Monte Carlo methods.

For spectroscopy, the expectation values considered are usually of the type of the ones encountered in Sec. 2.2, which can be written as $\langle \Phi(x)\overline{\Phi}(y) \rangle$, which represents a paricle of the Φ type created at spacetime point y ant destroyed at point x. If a meson is considered, for example the π^+, then Φ will have the form of a bilinear:

$$\Phi(x) = \bar{d}(x)\gamma_5 u(x) \tag{2.72}$$

---

[8] The notation is based on [Gattringer and Lang, 2010].

where u, d the fermionic fields for up and down quarks. This form is correct for Wilson quarks, but everything mentioned in this section can be slightly modified to fit staggered quarks. Anyway, to be more general, we can write:

$$\Phi(x) = \bar{\psi}_2(x)\Gamma\psi_1(x) \tag{2.73}$$

with Γ being some function. It usually has spin structure and can be space-independent, like γ_5, or it can be local, or it can even be nonlocal, in which case we would write: $\Phi(x_2, x_1) = \bar{\psi}_2(x_2)\Gamma(x_2, x_1)\psi_1(x_1)$. But this would not change the discussion much, so we will leave Γ as space-independent for now.

Let us deal with the fermionic path integral first. We can write:

$$\begin{aligned}
\langle\Phi(x)\overline{\Phi}(y)\rangle_F &= \langle\bar{\psi}_2(x)\Gamma\psi_1(x)\big(\bar{\psi}_2(y)\Gamma\psi_1(y)\big)^\dagger\rangle_F \\
&= \langle\bar{\psi}_2(x)\Gamma\psi_1(x)\psi_1^\dagger(y)\Gamma^\dagger\bar{\psi}_2^\dagger(y)\rangle_F
\end{aligned} \tag{2.74}$$

If Γ is product of gamma matrices, then we can write:

$$\Gamma^\dagger = \pm\gamma_4\Gamma\gamma_4 \tag{2.75}$$

and by using that $\bar{\psi} = \psi^\dagger\gamma_4$, Eq. (2.74) becomes:

$$\begin{aligned}
\langle\Phi(x)\overline{\Phi}(y)\rangle_F &= \pm\langle\bar{\psi}_2(x)\Gamma\psi_1(x)\bar{\psi}_1(y)\Gamma\psi_2(y)\rangle_F \\
&= \pm\langle\bar{\psi}_2(x)^a_\alpha\Gamma_{\alpha\beta}\psi_1(x)^a_\beta\bar{\psi}_1(y)^b_\gamma\Gamma_{\gamma\delta}\psi_2(y)^b_\delta\rangle_F \\
&= \pm\Gamma_{\alpha\beta}\Gamma_{\gamma\delta}\langle\bar{\psi}_2(x)^a_\alpha\psi_1(x)^a_\beta\bar{\psi}_1(y)^b_\gamma\psi_2(y)^b_\delta\rangle_F \\
&= \pm\Gamma_{\alpha\beta}\Gamma_{\gamma\delta}G_1(x;y)^{ab}_{\beta\gamma}G_2(y;x)^{ba}_{\delta\alpha}
\end{aligned} \tag{2.76}$$

where in the last step we used that the path integrals of fermions of different flavors factorize, and we defined the propagators of as:

$$G_i(x;y)^{ab}_{\alpha\beta} := \langle\psi_i(x)^a_\alpha\bar{\psi}_i(y)^b_\beta\rangle_F, \quad i = 1, 2 \tag{2.77}$$

An overall sign will not affect the spectrum, so from now on we will drop the ± in front.

We return to Eq. (2.71). We see that we still need $Z_F[U]$, but it is a standard Grassmann Gaussian integral:

$$
\begin{aligned}
Z_F[U] &= \int D\bar{\psi}_1 D\psi_1 e^{-\bar{\psi}_1 M_1[U]\psi_1} \int D\bar{\psi}_2 D\psi_2 e^{-\bar{\psi}_2 M_2[U]\psi_2} \\
&= \det M_1[U] \det M_2[U] \qquad (2.78)
\end{aligned}
$$

were we used that (for one flavor, to simplify the notation):

$$
S_F[\psi,\bar{\psi},U] = \bar{\psi}(x)^a_\alpha M(x,y)^{ab}_{\alpha\beta}\psi(y)^b_\beta \;\; \equiv \bar{\psi}(x)^a_\alpha\Big(D(x,y)^{ab}_{\alpha\beta} + m\delta^{(4)}(x-y)\delta^{ab}\delta_{\alpha\beta}\Big)\psi(y)^b_\beta \quad (2.79)
$$

For staggered fermions there would be no spin indices, but otherwise the form would be the same. Spacetime points x, y are also discrete on a lattice, but we treat them separately to make expressions more readable. Summation of repeated indices is implied.

So what we have to calculate is:

$$
\langle \Phi(x)\overline{\Phi}(y)\rangle = \frac{\int DU\Gamma_{\alpha\beta}\Gamma_{\gamma\delta}M_1^{-1}(x,y)^{ab}_{\beta\gamma}M_2^{-1}(y,x)^{ba}_{\delta\alpha}\det M_1 \det M_2 e^{-S_G[U]}}{\int DU \det M_1 \det M_2 e^{-S_G[U]}} \qquad (2.80)
$$

where we substituted the propagators G by their definition as M^{-1}.

With $|\Lambda|$ the 4-dimensional volume of the lattice, the Dirac matrix M has size $12|\Lambda| \times 12|\Lambda|$. In the case of staggered fermions, where there is no spin structure, the size is reduced to $3|\Lambda| \times 3|\Lambda|$. Inverting[9] M, which is a sparse matrix, is a computational problem that scales with $|\Lambda|$. Calculation of its determinant, however, is prohibitively expensive, as it scales with $|\Lambda|^3$.

One way to circumvent the need of determinant calculations is the so-called quenched approximation. In the quenched approximation, the quarks are heavy enough that the mass term dominates in the definition of M in Eq. (2.79). Then, the determinants will be factored out in Eq, (2.80) and will cancel each other out.

The quenched approximation corresponds to neglecting the effects of sea quarks, or, neglecting any Feynman diagram with virtual quark loops.

---

[9] In reality, we never invert M. Rather, we solve a linear system, as we will see immediately.

2.4.2 Building wall sources

Here we address the following problem. In order to have acceptable signal-to-noise ratio from our measurements or for other reasons, like measuring correlators of particles with well-defined spatial momenta, we would like to have access to the correlators $\langle\Phi(x)\overline{\Phi}(y)\rangle$ for a range of points x and y. Specifically, we would like to have access to the correlators for a range of spatial points $\mathbf{x}$ and $\mathbf{y}$, for fixed sink and source timeslices x_4 and y_4. We will start from Eq. (2.76), which we repeat here without the sign ambiguity:

$$\langle\Phi(x)\overline{\Phi}(y)\rangle_F = \Gamma_{\alpha\beta}\Gamma_{\gamma\delta}G_1(x;y)^{ab}_{\beta\gamma}G_2(y;x)^{ba}_{\delta\alpha} \tag{2.81}$$

We will consistently consider that y points correspond to the source at $y_4 = 0$ and x points to the sink at $x_4 = \tau$. If the meson is not flavor-diagonal then the two propagators G_1 and G_2 are different, but this would only complicate notation without changing things much.

Traditionally, a propagator is defined as the solution of:

$$M(x,y)^{ab}_{\alpha\beta}G(y;z)^{bc}_{\beta\gamma} = \delta^{(4)}(x-z)\delta^{ac}\delta_{\alpha\gamma} \tag{2.82}$$

or, symbolically:

$$G = M^{-1} \tag{2.83}$$

However, since it is impractical to solve the inversion problem as is, one prefers to calculate columns of the propagator, or, to put it more poetically, to calculate the propagator from one or from some points to all points. To do this, we introduce the source vector S:

$$M(y,x)^{ab}_{\alpha\beta}G^S(x)^{bc}_{\beta\gamma} = S(y)^{ac}_{\alpha\gamma} \tag{2.84}$$

where c is fixed to one of $1, 2, 3$, and γ to one of $1, 2, 3, 4$ which means that S is truly a vector and not a matrix. We will always assume that in the following, when talking about a propagator G_S coming from a source S. In other words, this notation implies the existence of $3 \times 4 = 14$ sources for Wilson and 3 sources for staggered quarks.

Eq. (2.84) can be solved numerically with some variation of the Conjugate Gradient (CG) method, and details about the method and its application in QCD problems can be found in

[Gattringer and Lang, 2010] and [DeGrand and Detar, 2006]. It is solved for each value of c and, e.g. for Wilson quarks, each value of γ because, as can be seen in Eq. (2.81), the color and spin trace requires knowledge of the propagators G for all their color and spin components.

We can replace the propagators G_1 and G_2 by some $G_1^{S_1}$ and $G_2^{S_2}$ in (2.81), calculated from sources S_1 and S_2 which need not be the same. We can see the correspondence between the G^{S_i} and the G_i by writing:

$$G_i^{S_i}(x)^{ab}_{\alpha\beta} = \sum_{y,c,\gamma} G_i(x;y)^{ac}_{\alpha\gamma} S_i(y)^{cb}_{\gamma\beta}, \quad i = 1, 2 \tag{2.85}$$

The backward-propagating G_2, which is needed in Eq. (2.81), can be obtained through the forward-propagating one, if the quarks are degenerate is mass. We write the fermion kernel M as:

$$M = D + m \tag{2.86}$$

where D is the discretization of $\gamma_\mu \partial_\mu$ and is called the Dirac operator and m is the mass term. D is γ_5-hermitian:

$$D^\dagger = \gamma_5 D \gamma_5 \tag{2.87}$$

and so is M. One therefore can, in case the particles ψ_1 and ψ_2 are degenerate in mass, use Eq. (2.87) to get both propagation with only one inversion.

The simplest example of a source is the point source, with which the propagator is calculated from a single spacetime point y_1 to everywhere else:

$$S(y)^{ab}_{\alpha\beta} = \delta^{(4)}(y - y_1)\delta^{ab}\delta_{\alpha\beta} \tag{2.88}$$

The use of the point source in Eq. (2.81) would give us $\langle \Phi(x)\overline{\Phi}(y_1)$.

Another simple example of a source can be constructed as follows:

$$S(y)^{ab}_{\alpha\beta} = \left[\delta^{(4)}(y - y_1) + \delta^{(4)}(y - y_2)\right] \delta^{ab}\delta_{\alpha\beta} \tag{2.89}$$

Using this source in (2.85) we get:

$$\begin{aligned} G^S(x)^{ab}_{\alpha\beta} &= \sum_{y,c,\gamma} G(x;y)^{ac}_{\alpha\gamma} \left[\delta^{(4)}(y - y_1) + \delta^{(4)}(y - y_2)\right] \delta^{cb}\delta_{\gamma\beta} \\ &= G(x;y_1)^{ab}_{\alpha\beta} + G(x;y_2)^{ab}_{\alpha\beta} \end{aligned} \tag{2.90}$$

If we now use this source for both propagators of (2.81), we will find that:

$$\begin{aligned}\langle\Phi(x)\overline{\Phi}(y)\rangle_F \to &\langle\Phi(x)\overline{\Phi}(y_1)\rangle_F + \langle\Phi(x)\overline{\Phi}(y_2)\rangle_F \\ &+ \Gamma_{\alpha\beta}\Gamma_{\gamma\delta}G_1(x;y_1)^{ab}_{\beta\gamma}G_2(y_2;x)^{ba}_{\delta\alpha} \\ &+ \Gamma_{\alpha\beta}\Gamma_{\gamma\delta}G_1(x;y_2)^{ab}_{\beta\gamma}G_2(y_1;x)^{ba}_{\delta\alpha}\end{aligned} \tag{2.91}$$

Let's examine these cross terms, e.g. the one in the middle line of Eq. (2.91). We can rewrite it:

$$\Gamma_{\alpha\beta}G_1(x;y_1)^{ab}_{\beta\gamma}\Gamma_{\gamma\delta}G_2(y_2;x)^{ba}_{\delta\alpha} = \Gamma_{\alpha\beta}\;\Gamma_{\gamma\delta}\langle\psi_1(x)^a_\beta\bar{\psi}_1(y_1)^b_\gamma\rangle_F\langle\psi_2(y_2)^b_\delta\bar{\psi}_2(x)^a_\alpha\rangle_F \tag{2.92}$$

This can be thought of as a correlation function:

$$\langle\bar{\psi}(x)^a_\alpha\Gamma_{\alpha\beta}\psi(x)^a_\beta\bar{\psi}(y_1)^b_\gamma\Gamma_{\gamma\delta}\psi(y_2)^b_\delta\rangle_F \equiv \langle\Phi(x)\overline{\Phi}'(\mathbf{y_1},0;\mathbf{y_2},0)\rangle_F \tag{2.93}$$

In the Coulomb gauge, this object can in principle give nonzero contribution after the gauge path-integration $\langle\ldots\rangle_G$ is performed. We can apply the usual trick and write:

$$\langle\Phi(x)\overline{\Phi}'(\mathbf{y_1},0;\mathbf{y_2},0)\rangle \sim \sum_n \langle 0|\Phi(\mathbf{x})|n\rangle\langle n|\overline{\Phi}'(\mathbf{y_1};\mathbf{y_2})|0\rangle e^{-E_n\tau} \tag{2.94}$$

These contributions will not spoil the energies E_n of a specific channel, with which (2.94) might have nonvanishing overlap, but it will spoil the amplitudes $\langle 0|\Phi(\mathbf{x})|n\rangle$. We will return to this point later.

We can expand this 2-point source to the whole $\tau = 0$ timeslice or a subset of it and create a wall source $S_\mathbf{Y}$:

$$S_\mathbf{Y}(y)^{ab}_{\alpha\beta} = \delta_{\alpha\beta}\delta^{ab}\sum_{\mathbf{y}_i\in\mathbf{Y}}\delta^{(4)}(y-y_i) \tag{2.95}$$

where $\mathbf{Y}$ is the subset of the source timeslice. The resulting propagator reads:

$$G^{S_\mathbf{Y}}(x)^{ab}_{\alpha\beta} = \sum_{\mathbf{y}_i\in\mathbf{Y}} G(x;\mathbf{y}_i,0)^{ab}_{\alpha\beta} \tag{2.96}$$

By using a wall source the noise in the spectrum measurements becomes significantly lower, equivalently to averaging many point-source spectrum measurements; Here, though, a single inversion is needed.

In most cases, after propagators G^S have been calculated and the index summation of (2.81) is performed, $\mathbf{x}$ is summed over the whole or a subset of the sink timeslice, to further enhance signal or to apply some operation.

2.4.3 Nonzero momentum mesons

Introduction of momentum is done through:

$$\Phi(\mathbf{p},\tau) = \frac{1}{\sqrt{|\Lambda_3|}} \sum_{\mathbf{z}\in\Lambda_3} \Phi(\mathbf{z},\tau) e^{-i\mathbf{p}\cdot\mathbf{z}} \tag{2.97}$$

where we define the spatial part of the lattice Λ as Λ_3. Then, we can have:

$$\langle \Phi(\mathbf{p},\tau)\overline{\Phi}(\mathbf{q},0)\rangle = \frac{1}{|\Lambda_3|} \sum_{\mathbf{x},\mathbf{y}\in\Lambda_3} \langle \Phi(\mathbf{x},\tau)\overline{\Phi}(\mathbf{y},0)\rangle e^{-i\mathbf{p}\cdot\mathbf{x}+i\mathbf{q}\cdot\mathbf{y}} \tag{2.98}$$

We define $\mathbf{r} = \mathbf{x} - \mathbf{y}$ and write:

$$\begin{aligned}
\langle \Phi(\mathbf{p},\tau)\overline{\Phi}(\mathbf{q},0)\rangle &= \frac{1}{|\Lambda_3|} \sum_{\mathbf{r},\mathbf{y}} \langle \Phi(\mathbf{y}+\mathbf{r},\tau)\overline{\Phi}(\mathbf{y},0)\rangle e^{-i\mathbf{p}\cdot\mathbf{y}+i\mathbf{q}\cdot\mathbf{y}-i\mathbf{r}\cdot\mathbf{p}} \\
&= \frac{1}{|\Lambda_3|} \sum_{\mathbf{r}} e^{-i\mathbf{r}\cdot\mathbf{p}} \sum_{\mathbf{y}} \langle \Phi(\mathbf{y}+\mathbf{r},\tau)\overline{\Phi}(\mathbf{y},0)\rangle e^{i\mathbf{y}\cdot(\mathbf{q}-\mathbf{p})} \\
&= \frac{1}{|\Lambda_3|} \sum_{\mathbf{r}} e^{-i\mathbf{r}\cdot\mathbf{p}} \langle \Phi(\mathbf{r},\tau)\overline{\Phi}(\mathbf{0},0)\rangle \sum_{\mathbf{y}} e^{i\mathbf{y}\cdot(\mathbf{q}-\mathbf{p})} \\
&= \frac{1}{\sqrt{|\Lambda_3|}} \sum_{\mathbf{x}} e^{-i\mathbf{x}\cdot\mathbf{p}} \langle \Phi(\mathbf{x},\tau)\overline{\Phi}(\mathbf{0},0)\rangle \delta^{(3)}(\mathbf{p}-\mathbf{q})
\end{aligned} \tag{2.99}$$

We used translation invariance of the correlation function in going from 2nd to 3rd line. As we can see in (2.99) operators of different momenta are orthogonal at an expectation-value level.

On the lattice, both Eqs. (2.98) and (2.99) can be used to measure nonzero momentum meson correlators. The latter can be implemented with a point source and the former with a wall source, while in both cases, summation over all spatial points should be applied at the sink. We can imagine that using (2.99) will yield more noise, as this relation is based upon an expectation-value level reasoning.

If the point source method is selected, then a collection of sources S_0 built:

$$S_0(y)^{ab}_{\alpha\beta} = \delta^{(4)}(y)\delta_{\alpha\beta}\delta^{ab} \tag{2.100}$$

Then, after calculating $G_1^{S_0}(\mathbf{x},\tau)^{ab}_{\alpha\beta}$ and $G_2^{S_0}(\mathbf{x},\tau)^{ab}_{\alpha\beta}$ for all b and β, phases $\exp(-i\mathbf{x}\cdot\mathbf{p})$ for all $\mathbf{x}$ are applied and the quantity

$$\Gamma_{\alpha\beta}\, e^{-i\mathbf{x}\cdot\mathbf{p}} G_1^{S_0}(\mathbf{x},\tau)^{ab}_{\beta\gamma}\Gamma_{\gamma\delta'}\left(\gamma_{5\delta\delta'}G_2^{S_0}(\mathbf{x},\tau)^{ba}_{\delta'\alpha'}\gamma_{5\alpha'\alpha}\right)^* = e^{-i\mathbf{x}\cdot\mathbf{p}}\langle\Phi(\mathbf{x},\tau)\overline{\Phi}(\mathbf{0},0)\rangle_F$$

is constructed by tying together the color and spin indices. Here we showed how γ_5-hermiticity is used in practice, in order to turn G_2^S into a backward propagator, as needed from Eq. (2.81). Finally, summation on $\mathbf{x}$ is performed and $\langle\Phi(\mathbf{p},\tau)\overline{\Phi}(\mathbf{p},0)\rangle_F$ is obtained. Note that only one of the propagators needs phases to be applied.

The wall-source construction based on (2.98) is slightly more complicated but leads to better signal. One has to construct two collections of wall sources, S_W and $S_{W\mathbf{p}}$, with momentum phases included in $S_{W\mathbf{p}}$:

$$S_W(y)^{ab}_{\alpha\beta} = \delta_{\alpha\beta}\delta^{ab}\sum_{\mathbf{y}'\in\Lambda_3}\delta^{(4)}(y-y') \tag{2.101}$$

$$S_{W\mathbf{p}}(y)^{ab}_{\alpha\beta} = \delta_{\alpha\beta}\delta^{ab}\sum_{\mathbf{y}'\in\Lambda_3}\delta^{(4)}(y-y')e^{i\mathbf{p}\cdot\mathbf{y}'} \tag{2.102}$$

We then build the respective propagators:

$$G^{S_W}(\mathbf{x},\tau)^{ab}_{\alpha\beta} = \sum_{\mathbf{y}'\in\Lambda_3} G(\mathbf{x},\tau;\mathbf{y}',0)^{ab}_{\alpha\beta} \tag{2.103}$$

$$G^{S_{W\mathbf{p}}}(\mathbf{x},\tau)^{ab}_{\alpha\beta} = \sum_{\mathbf{y}'\in\Lambda_3} e^{i\mathbf{p}\cdot\mathbf{y}'}G(\mathbf{x},\tau;\mathbf{y}',0)^{ab}_{\alpha\beta} \tag{2.104}$$

After doing that, we have to apply phases $\exp(-i\mathbf{x}\cdot\mathbf{p})$ at the sink and tie together with the gamma matrices, exactly like in the point source case above, and finally sum over $\mathbf{x}$. We can apply the phases $\exp(-i\mathbf{x}\cdot\mathbf{p})$ on whichever one of the two propagators we like.

2.4.4 The random color wall source

Whenever amplitudes have to be determined from correlator measurements, one either needs to use point sources, or find a way to suppress cross terms from wall sources, like the ones in Eq. (2.91). Roughly speaking, the way random color wall source achieves that is by assigning to every point in the source timeslice a random vector in the 3-dimensional color space and average over them. This way, all averages that involve different $\tau = 0$ points will be suppressed.

In order for the suppression to happen, one needs to create multiple sources, say n_r, and take the average– and, in principle, the more the sources, the better the suppression.

The random color wall sources have one conceptual difference to the ordinary wall sources. They are only collections in spin, but not in color indices, i.e. for Wilson quarks one builds $4n_r$ and not $12n_r$ sources, as the average will also suppress terms between different color indices, and the color-trace will be properly calculated.

To be more specific, the random color wall source is defined as:

$$S_r(y)^a_{\alpha\beta} = \delta_{\alpha\beta} \sum_{\mathbf{y}' \in \Lambda_3} \delta^{(4)}(y - y') \left(\delta^{a1} C^1(y') + \delta^{a2} C^2(y') + \delta^{a3} C^3(y')\right) \tag{2.105}$$

where $C(y)$ is a vector transforming under $SU(3)_c$ and each $C^b(y)$ is a random complex number that follows a Gaussian distribution, so that:

$$\overline{C^b(y'_1) C^c(y'_2)} = \delta^{bc} \delta^{(4)}(y'_1 - y'_2) \tag{2.106}$$

Here the line implies the average over the n_r sources created.

To see the effect of the random color wall source, let's again consider the 2-point source example:

$$\begin{aligned} S_r(y)^a_{\alpha\beta} &= \delta_{\alpha\beta}\delta^{(4)}(y - y_1)\Big(\delta^{a1} C^1(y_1) + \delta^{a2} C^2(y_1) + \delta^{a3} C^3(y_1)\Big) \\ &+ \delta_{\alpha\beta}\delta^{(4)}(y - y_2)\Big(\delta^{a1} C^1(y_2) + \delta^{a2} C^2(y_2) + \delta^{a3} C^3(y_2)\Big) \end{aligned} \tag{2.107}$$

With this source we build:

$$\begin{aligned} G^{S_r}(x)^a_{\alpha\beta} &= \sum_{y,c,\gamma} G(x;y)^{ac}_{\alpha\gamma} S_r(y)^c_{\gamma\beta} \\ &= \sum_{y,c,\gamma} G(x;y)^{ac}_{\alpha\gamma} \delta_{\gamma\beta}\Big(\delta^{(4)}(y - y_1) \sum_{b=1,2,3} \delta^{bc} C^b(y_1) + \delta^{(4)}(y - y_2) \sum_{b=1,2,3} \delta^{bc} C^b(y_2)\Big) \\ &= G(x;y_1)^{a1}_{\alpha\beta} C^1(y_1) + G(x;y_1)^{a2}_{\alpha\beta} C^2(y_1) + G(x;y_1)^{a3}_{\alpha\beta} C^3(y_1) \\ &+ G(x;y_2)^{a1}_{\alpha\beta} C^1(y_2) + G(x;y_2)^{a2}_{\alpha\beta} C^2(y_2) + G(x;y_2)^{a3}_{\alpha\beta} C^3(y_2) \end{aligned} \tag{2.108}$$

If we substitute this back into (2.81) we see that:

$$\begin{aligned}
\langle\Phi(x)\overline{\Phi}(y)\rangle_F \quad &\rightarrow \quad \overline{\left(C^1(y_1)\right)^2}\Gamma_{\alpha\beta}\Gamma_{\gamma\delta}G_1(x;y_1)^{a1}_{\beta\gamma}G_2(y_1;x)^{1a}_{\delta\alpha} \\
&+ \quad \overline{\left(C^2(y_1)\right)^2}\Gamma_{\alpha\beta}\Gamma_{\gamma\delta}G_1(x;y_1)^{a2}_{\beta\gamma}G_2(y_1;x)^{2a}_{\delta\alpha} \\
&+ \quad \overline{\left(C^3(y_1)\right)^2}\Gamma_{\alpha\beta}\Gamma_{\gamma\delta}G_1(x;y_1)^{a3}_{\beta\gamma}G_2(y_1;x)^{3a}_{\delta\alpha} \\
&+ \quad \overline{C^1(y_1)C^2(y_1)}\Gamma_{\alpha\beta}\Gamma_{\gamma\delta}G_1(x;y_1)^{a1}_{\beta\gamma}G_2(y_1;x)^{2a}_{\delta\alpha} \\
&+ \quad \text{similar mixed terms involving only } y_1 \\
&+ \quad \overline{\left(C^1(y_2)\right)^2}\Gamma_{\alpha\beta}\Gamma_{\gamma\delta}G_1(x;y_2)^{a1}_{\beta\gamma}G_2(y_2;x)^{1a}_{\delta\alpha} \\
&+ \quad \overline{\left(C^2(y_2)\right)^2}\Gamma_{\alpha\beta}\Gamma_{\gamma\delta}G_1(x;y_2)^{a2}_{\beta\gamma}G_2(y_2;x)^{2a}_{\delta\alpha} \\
&+ \quad \overline{\left(C^3(y_2)\right)^2}\Gamma_{\alpha\beta}\Gamma_{\gamma\delta}G_1(x;y_2)^{a3}_{\beta\gamma}G_2(y_2;x)^{3a}_{\delta\alpha} \\
&+ \quad \overline{C^1(y_2)C^2(y_2)}\Gamma_{\alpha\beta}\Gamma_{\gamma\delta}G_1(x;y_2)^{a1}_{\beta\gamma}G_2(y_2;x)^{2a}_{\delta\alpha} \\
&+ \quad \text{similar mixed terms involving only } y_2 \\
&+ \quad \overline{C^1(y_1)C^1(y_2)}\Gamma_{\alpha\beta}\Gamma_{\gamma\delta}G_1(x;y_1)^{a1}_{\beta\gamma}G_2(y_2;x)^{1a}_{\delta\alpha} \\
&+ \quad \text{similar mixed terms involving both } y_1 \text{ and } y_2 \\
&\xrightarrow{n_r>1} \quad \Gamma_{\alpha\beta}\Gamma_{\gamma\delta}G_1(x;y_1)^{ab}_{\beta\gamma}G_2(y_1;x)^{ba}_{\delta\alpha} \\
&+ \quad \Gamma_{\alpha\beta}\Gamma_{\gamma\delta}G_1(x;y_2)^{ab}_{\beta\gamma}G_2(y_2;x)^{ba}_{\delta\alpha} \\
&= \quad \langle\Phi(x)\overline{\Phi}(y_1)\rangle_F + \langle\Phi(x)\overline{\Phi}(y_2)\rangle_F
\end{aligned} \tag{2.109}$$

We see that cross terms are suppressed because of the averaging and therefore the problem illustrated in Eq. (2.91) is eliminated and we can use our measurements to access amplitudes. In practice, it is sufficient to set $n_r = 3$, in which case the number of inversions is at the end of the day equal to the one for ordinary wall sources.

2.5 Simulating a lattice $SU(3)$ gauge theory on the computer

Monte Carlo integration on the computer allows us to perform the path integral over the gauge links $U_\mu(x)$, as in Eq. (2.68). The probability distribution that we want to sample is, in the quenched case:

$$dP[U'] = \frac{DU'e^{-S_G[U']}}{\int DUe^{-S_G[U]}} \tag{2.110}$$

with U' denoting a specific gauge configuration. In the quenched case, where there is no fermionic determinant, we can use a local updating algorithm, that is, we can update one link at a time. Then, the new configuration U', which should be selected with a probability that follows Eq. (2.110), differs from the previous one in the Markov chain just by one link.

Perhaps the simplest local algorithm that one can apply is a Metropolis algorithm, where from each link U we construct a proposed link $U'_\mu(x)$:

$$U'_\mu(x) = X^\epsilon_\mu(x) U_\mu(x) \tag{2.111}$$

with $X^\epsilon_\mu(x)$ being a random $SU(3)$ matrix. The probability of acceptance of the new link is determined by the change in the action ΔS_G:

$$\Delta S_G = S_G[U'] - S_G[U] = -\frac{2}{g^2}\mathrm{ReTr}\left(\left(U'_\mu(x) - U_\mu(x)\right)A\right) \tag{2.112}$$

where A is the staple around the link in question, and its specific type depends on the choice of gauge action we are using. A stays constant during the update of the link. In order to control acceptance we have introduced a real number ϵ which determines how close the matrix $X^\epsilon_\mu(x)$ is to the identity.

In our simulations, in order to improve acceptance, we use what is known as the heatbath algorithm. As is the case with the Metropolis, the heatbath is a local updating algorithm, but it does not involve accept/reject step, since the new link $U'_\mu(x)$ is chosen directly from the desired probability distribution.

The heatbath algorithm for an $SU(2)$ gauge theory was shown in [Creutz, 1980] and the generalization for $SU(N)$ was made in [Cabibbo and Marinari, 1982]. The $SU(2)$ algorithm assumes a very simple form, because of the fact that any sum of $SU(2)$ elements is proportional to an $SU(2)$ element. If a specific link U is to be updated, then the relevant part of the probability density of Eq. (2.110) is:

$$dP(U) \sim dU \exp\left(\frac{2}{g^2}\mathrm{ReTr}(UA)\right) \tag{2.113}$$

with A the staple, which is proportional to an $SU(2)$ matrix V: $A = aV$. The measure dU, because of gauge invariance, is invariant under multiplication within the group, therefore $dU = d(UV)$. If we now call $X = UV$ then the probability density becomes:

$$dP(X) \sim dX \exp\left(\frac{2a}{g^2}\mathrm{ReTr}X\right) \tag{2.114}$$

With the usual representation that employs the Pauli matrices σ_i:

$$X = 1_2 x_0 + i\mathbf{x}\cdot\boldsymbol{\sigma} \tag{2.115}$$

the task of sampling the $SU(2)$ element X can be reduced to sampling three independent real variables, x_0, ϕ, θ, where the latter two define the direction of $\mathbf{x}$. Specifically, one can show that:

$$dP(X) \sim \frac{1}{2\pi^2} d\cos\theta d\phi dx_0 \sqrt{1-x_0^2}\exp\left(\frac{4a}{g^2}x_0\right) \tag{2.116}$$

and then the new link U' can be reconstructed as $U' = XV^\dagger$.

The pseudo-heatbath for $SU(3)$ is implemented by considering three $SU(2)$ subgroups of $SU(3)$ and by and performing three successive $SU(2)$ heatbaths, that produce three $SU(2)$ "links", called R, S, T. In the first heatbath, the role of the staple is played by UA, and R is sampled via:

$$dP(R) \sim dR \exp\left(\frac{2}{g^2}\mathrm{ReTr}(RUA)\right) \tag{2.117}$$

where the relevant 2×2 block of UA is considered in the exponent. In the second heatbath, the role of the staple is played by RUA and S is sampled, and in the third, the staple is $SRUA$ and T is sampled. Finally, the new $SU(3)$ link U' is constructed as $U' = TSRU$.[10]

In practice, the heatbath updating can be combined with overrelaxation steps [Creutz, 1987, Adler, 1988], which do not change the action but help decorrelate the gauge configurations produced by the heatbath. The configurations produced by the overrelaxation steps have the same probability of occurrence, and therefore they do not spoil the properties of the Markov chain. As with the heatbath, the $SU(3)$ algorithm can be constructed from $SU(2)$ subgroups, for which there is a simple choice of an overrelaxation step; One can utilize the matrix V that we defined above Eq. (2.113):

$$U' = V^\dagger U^\dagger V^\dagger \tag{2.118}$$

---

[10] See the quite pedagogical [Cabibbo and Marinari, 1982] for details and proof.

This leaves the action invariant:

$$\mathrm{Tr}\left(U'A\right) = \mathrm{Tr}\left(V^\dagger U^\dagger V^\dagger A\right) = a\mathrm{Tr}\left(V^\dagger U^\dagger V^\dagger V\right) = a\mathrm{Tr}\left(V^\dagger U^\dagger\right) = \mathrm{Tr}(UA) \tag{2.119}$$

2.6 Simulating lattice QCD with dynamical staggered quarks

When the fermion determinants are not set to 1 in the path integrals– see Eqs. (2.68) and (2.78)– but evaluated during the sampling of the gauge configurations, then one speaks of dynamical simulations. As mentioned, a direct evaluation of the fermion determinants per configuration would not be feasible. However, one can represent a determinant as a Gaussian integral over bosonic fields Φ, Φ^*:

$$\det M = \int D\Phi D\Phi^* e^{-\Phi^* M^{-1}\Phi} \tag{2.120}$$

If the Dirac operator is γ_5-hermitian, has exact lattice chiral symmetry[11] and there is a nonzero bare quark mass in M, then $\det M > 0$. This holds not because all the eigenvalues of M are positive, but because they are paired, i.e. if $i\lambda + m$ is an eigenvalue, then $-i\lambda + m$ is also an eigenvalue. This happens for staggered fermions too, although they are not exactly chirally symmetric.

However, since $\det M$ is to be used as a weight in the sampling of gauge fields, we need it to be strictly positive for every configuration. Therefore we always consider pairs of degenerate quark flavors, i.e. $(\det M)^2$. With use of the γ_5-hermiticity of M, we can write:

$$(\det M)^2 = \det M \det M^\dagger = \det\left(M^\dagger M\right) > 0 \tag{2.121}$$

where the strict inequality holds for staggered quarks. With staggered quarks, there is another advantage, namely that $M^\dagger M$ couples even to even and odd to odd lattice sites, so by defining $\Phi, \Phi^\dagger$ only on even sites we can avoid the extra doubling introduced by considering $M^\dagger M$.

The algorithm that we use for dynamical simulations is a global updating algorithm, in the sense that a proposed new gauge configuration in the Markov chain involves changes in all the links of the lattice. It is based on introducing momenta H conjugate to the links U and evolving them with molecular dynamics [Gottlieb et al., 1987].

---

[11] This is meant in terms of the Ginsparg-Wilson equation [Ginsparg and Wilson, 1982].

Before the introduction of momenta, we were dealing with the sum of the gauge action and the term coming from the pseudofermions $\Phi, \Phi^\dagger$, which can be seen as an effective action:

$$\begin{aligned} S_{eff}[U,\Phi,\Phi^\dagger] &= S_G[U] + \Phi^\dagger \left(M^\dagger M\right)^{-1} \Phi \\ &= S_G[U] + S_\Phi[U,\Phi,\Phi^\dagger] \end{aligned} \tag{2.122}$$

Then from Eq. (2.68):

$$\begin{aligned} \langle O \rangle &= \frac{\int DUD\Phi D\Phi^\dagger \langle O \rangle_F \exp\left(-S_{eff}[U,\Phi,\Phi^\dagger]\right)}{\int DUD\Phi D\Phi^\dagger \exp\left(-S_{eff}[U,\Phi,\Phi^\dagger]\right)} \\ &= \frac{\int DHDUD\Phi D\Phi^\dagger \langle O \rangle_F \exp\left(-\frac{1}{2}\mathrm{Tr}H^2 - S_{eff}[U,\Phi,\Phi^\dagger]\right)}{\int DHDUD\Phi D\Phi^\dagger \exp\left(-\frac{1}{2}\mathrm{Tr}H^2 - S_{eff}[U,\Phi,\Phi^\dagger]\right)} \end{aligned} \tag{2.123}$$

This allows us to form a Hamiltonian $\mathcal{H}_{\Phi,\Phi^\dagger}[U,H]$:

$$\mathcal{H}_{\Phi,\Phi^\dagger}[U,H] = \frac{1}{2}\mathrm{Tr}H^2 + S_{eff}[U,\Phi,\Phi^\dagger] \tag{2.124}$$

and to apply Hamilton's equations for evolution:

$$\dot{U} = H \tag{2.125}$$

$$\dot{H} = -f_\mu(x) = -\frac{\partial S_{eff}}{\partial U_\mu(x)} \tag{2.126}$$

We call $f_\mu(x)$ the force. The derivative in Eq. (2.126) is symbolic. It is properly defined as:

$$f_\mu(x) = \sum_a T^a S_{eff}\left[e^{isT^a} U_\mu(x)\right] \tag{2.127}$$

We can write the force as a sum of a gauge and a fermion contribution:

$$f_\mu(x) = f_\mu^G(x) + f_\mu^F(x) \tag{2.128}$$

The fermion force $f_{F,\mu}^F(x)$ is costly to calculate, since it involves inversions of the fermion matrix $M^\dagger M$ and, if the staggered action is improved, it is a nontrivial task to even write it down and implement it in a code. In the case of an unimproved staggered action one can start with:

$$\begin{aligned} f_\mu^F(x) &= \frac{\partial S_\Phi}{\partial U_\mu(x)} = \frac{\partial}{\partial U_\mu(x)} \Phi^\dagger \left(M^\dagger M\right)^{-1} \Phi \\ &= -\left(\left(M^\dagger M\right)^{-1}\Phi\right)^\dagger \left(\frac{M}{\partial U_\mu(x)} M^\dagger + M \frac{M^\dagger}{\partial U_\mu(x)}\right)\left(\left(M^\dagger M\right)^{-1}\Phi\right) \end{aligned} \tag{2.129}$$

and follow the steps of [Gottlieb et al., 1987].

Let us go back to the structure of the Hybrid Monte Carlo (HMC) algorithm, as it is called. The unit of evolution is called trajectory, and has unit length, but is divided in n steps of length ε, so that $n\varepsilon = 1$. At the beginning of every trajectory, the pseudofermion fields are sampled as required by Eq. (2.123), by sampling a complex Gaussian random vector R and then setting $\Phi = M^\dagger R$. The momenta H are sampled from a Gaussian distribution as well. Then, the n discrete molecular dynamics steps of length ε are performed, with leapfrog updating or some improved scheme that guarantees reversibility of the Markov chain. Finally, at the end of the trajectory, the new gauge configuration is accepted or rejected with a Metropolis step, which corrects the $O(\varepsilon^2)$ errors of the molecular dynamics evolution.

In order to cover the phase space faster and reduce autocorrelations, at the end of every trajectory the momenta H are redrawn from a Gaussian distribution. Also, in practice, since the gauge force is significantly cheaper and quantitatively more significant, it is updated more often than the fermion force.

Finally, a word about rooting is in order. It has been found that if N_f flavors of degenerate staggered quarks are to be simulated, then one can substitute:

$$\det(M^\dagger M) \rightarrow \left(\det(M^\dagger M)\right)^{N_f/4} \tag{2.130}$$

Then, this substitution can be made at the quark matrix level, and one can use:

$$S_\Phi = \Phi^\dagger \left(M^\dagger M\right)^{-1} \Phi \rightarrow \Phi^\dagger \left(M^\dagger M\right)^{-N_f/4} \Phi \tag{2.131}$$

In our simulations, since we have degenerate u, d quarks and heavier s, we need a square root for u, d and a fourth root for s.

Taking the root of the quark matrix is not well-defined in field theory, and at finite lattice spacing the eigenvalues of the quark matrix are not degenerate. However, despite both of these facts, there is no concrete evidence that rooting spoils fundamental properties of the theory,[12] and there are significant indications (theoretical and numerical) that rooting works fine.

---

[12] The objections to rooting are summarized in [Creutz, 2007]. See [Bernard et al., 2007] for some responses to these objections.

In order to implement rooting in the simulations, the Rational Hybrid Monte Carlo (RHMC) algorithm, was introduced in [Clark and Kennedy, 2004]. This algorithm is named after the fact that the root is approximated by a rational function, as in Eq. (4.18).

CHAPTER 3

STAGGERED QUARKS

In this chapter we will take a closer look at the staggered quark action. We will first investigate its symmetries, then study how to build mesonic operators with proper quantum numbers out of staggered quark fields. We will take a look at the renormalization of staggered quark mass, which as mentioned in Sec. 2.3, is multiplicative, and finally see how improved staggered actions work.

The main idea behind performing the transformation that produces the staggered-fermion action is that, if by some spacetime transformation the gamma matrices are diagonalized, then the fermion action will be a sum of 4 equivalent pieces, out of which we can pick one and that way reduce the number of doublers from 15 to only 3.

3.1 Symmetries of the staggered action

As we mentioned in Sec. 2.3 the staggered action reads:

$$S_F[\chi,\bar{\chi},U] = \frac{1}{2}\sum_{x,\mu}\eta_\mu(x)\bar{\chi}(x)\big(U_\mu(x)\chi(x+\hat{\mu}) - U^\dagger_\mu(x-\hat{\mu})\chi(x-\hat{\mu})\big) + m\sum\bar{\chi}(x)\chi(x) \tag{3.1}$$

where

$$\eta_\mu(x) = (-1)^{\sum_{\nu<\mu}x_\nu} \tag{3.2}$$

are the staggered phases, which appear as a result of the spin-diagonalization of the original fermion action with the use of the unitary local transformation:

$$\psi(x) = \gamma_1^{x_1}\gamma_2^{x_2}\gamma_3^{x_3}\gamma_4^{x_4}\chi(x), \quad \bar{\psi}(x) = \bar{\chi}(x)\gamma_4^{x_4}\gamma_3^{x_3}\gamma_2^{x_2}\gamma_1^{x_1} \tag{3.3}$$

From this definition we can also check that $\chi^\dagger(x)\eta_4(x) = \bar{\chi}(x)$.

Again, as mentioned before, this transformation, apart from diagonalizing the spin-structure, it also staggers the 4 remaining tastes of fermions in the four-dimensional spacetime. This complicates the symmetries of the action, as now shifts, hypercubic rotations, inversions and charge conjugation all involve taste.

For simplicity we will investigate the symmetries of the free staggered action, where all links $U_\mu(x)$ are set to 1. We will first write down the symmetries in position space[1]:

---

[1] We do not mention the obvious $SU(3)_c$ symmetry of the action.

1. Shifts S_μ

$$S_\mu : \quad \chi(x) \to \zeta_\mu(x)\chi(x+\mu) \tag{3.4}$$

where we have introduced the phases:

$$\zeta_\mu(x) = (-1)^{\sum_{\nu>\mu} x_\nu} \tag{3.5}$$

2. Hypercube rotations $R_{\kappa\lambda}$

$$R_{\kappa\lambda} : \quad \chi(x) \to \mathcal{R}_{\kappa\lambda}(R^{-1}_{\kappa\lambda}x)\chi(R^{-1}_{\kappa\lambda}x) \tag{3.6}$$

where $R_{\kappa\lambda}$ the ordinary vector-rotation matrix around the axis perpendicular to the $\kappa\lambda$ plane and:

$$\mathcal{R}_{\kappa\lambda}(x) = \frac{1}{2}\big(1 \pm \eta_\kappa(x)\eta_\lambda(x) \mp \zeta_\kappa(x)\zeta_\lambda(x) + \eta_\kappa(x)\eta_\lambda(x)\zeta_\kappa(x)\zeta_\lambda(x)\big) \tag{3.7}$$

3. Axis reversal $\hat{I}_\rho$

$$I_\rho : \quad \chi(x) \to (-1)^{x_\rho}\chi(I_\rho x) \tag{3.8}$$

where I_ρ the matrix that implements inversion in the ρ direction on a 4-dimensional vector.

4. Parities I_s and P

In the continuum, or on the lattice with non-staggered fermions, the inversion on all spatial directions is the parity. However, with staggered fermions, the spatial inversion I_s defined as:

$$I_s : \quad \chi(x) \to (-1)^{x_1+x_2+x_3}\chi(I_1 I_2 I_3 x) \equiv \eta_4(x)\chi(I_s x) \tag{3.9}$$

cannot be interpreted as parity, since it involves taste[2], and thus cannot be used when we later match to quantum numbers of continuum particle states. We will see how to create a sensible parity transformation P a bit later.

5. Fermion number Ω_q

This is a global $U(1)$ symmetry:

$$\Omega_q : \quad \chi(x) \to e^{iq}\chi(x) \quad \bar{\chi}(x) \to \bar{\chi}(x)e^{-iq} \tag{3.10}$$

---

[2] The taste transformation is hidden inside $I_s x = (-\mathbf{x}, x_4)$

6. Chiral transformation $\Omega_\beta(x)$

This is a remnant of the chiral symmetry that the massless naive fermion action exhibits. We will discuss its implications later. It is a local $U(1)$ symmetry and it reads:

$$\Omega_\beta(x): \quad \chi(x) \to e^{i\beta\epsilon(x)}\chi(x) \quad \bar{\chi}(x) \to \bar{\chi}(x)e^{i\beta\epsilon(x)} \tag{3.11}$$

The phases $\epsilon(x)$ as defined as:

$$\epsilon(x) = (-1)^{x_1+x_2+x_3+x_4} \tag{3.12}$$

7. Charge conjugation C_0

$$C_0: \quad \chi(x) \to \epsilon(x)\bar{\chi}^T(x) \quad \bar{\chi}(x) \to -\chi^T(x)\epsilon(x) \tag{3.13}$$

We would like to write these symmetry transformations in a way that the effect they have on taste is explicit, and not intertwined with spacetime transformations. This is only possible in momentum space. Let us investigate S_μ as an example.

First we rewrite the phases $\zeta_\mu(x)$ as:

$$\zeta_\mu(x) = e^{i\pi_{\zeta_\mu}\cdot x} \tag{3.14}$$

where we defined four 4-vectors π_{ζ_μ} as:

$$\begin{aligned} \pi_{\zeta_1} &= (0,\pi,\pi,\pi) \\ \pi_{\zeta_2} &= (0,0,\pi,\pi) \\ \pi_{\zeta_3} &= (0,0,0,\pi) \\ \pi_{\zeta_4} &= (0,0,0,0) \end{aligned} \tag{3.15}$$

Then we can rewrite Eq. 3.4, with the Brillouin zone BZ as $(-\pi,\pi]$ in every direction:

$$\begin{aligned} &\int_{p\in BZ} e^{ip\cdot x}\chi(p) \to \int_{p\in BZ} e^{i\pi_{\zeta_\mu}\cdot x+ip\cdot x+ip_\mu}\chi(p) = \int_{p\in BZ} e^{ip\cdot x+ip_\mu}\chi(p+\pi_{\zeta_\mu}) \\ &\Rightarrow \chi(p) \to e^{ip_\mu}\chi(p+\pi_{\zeta_\mu}) \end{aligned} \tag{3.16}$$

We used a variable shift, the 2π-periodicity of $\chi(p)$ and the fact that $\pi_{\zeta_\mu} \cdot \mu = 0$. For reasons that will become apparent later we make two steps. The first is to move the BZ by $\pi/2$ to the right in every direction, so that $p_\mu \in (-\pi/2, 3\pi/2]$. The second is to divide the new BZ into 16 hypercubes, each centered around one of the 16 vectors $\pi_A = (0,0,0,0),\ (\pi,0,0,0),\ (0,\pi,0,0),\ldots,(\pi,\pi,\pi,\pi)$, and express p as an expansion around those centers:

$$p = k + \pi_A, \quad A = 1,\ldots,16 \tag{3.17}$$

where now $k_\mu \in (-\pi/2, \pi/2]$. Later we will see that the poles of the staggered propagator will be located at $p = \pi_A$ or equivalently $k = 0$. We can also rename:

$$\phi_A(k) := \chi(k + \pi_A) \tag{3.18}$$

We can now rewrite Eq. (3.16) as:

$$\begin{aligned}
&\chi(k+\pi_A) \longrightarrow e^{ik_\mu + i(\pi_A)_\mu} \chi(k + \pi_A + \pi_{\zeta_\mu}) \\
&\Rightarrow \phi_A(k) \longrightarrow e^{ik_\mu} e^{i(\pi_A)_\mu} \delta_P^{(4)}(\pi_B + \pi_{\zeta_\mu} + \pi_A)\phi_B(k) \\
&\Rightarrow \phi_A(k) \longrightarrow e^{ik_\mu} S_\mu^A \delta_P^{(4)}(\pi_B + \pi_{\zeta_\mu} + \pi_A)\phi_B(k)
\end{aligned}$$

which means that in momentum space:

$$S_\mu : \quad \phi_A(k) \longrightarrow e^{ik_\mu} (\Xi_\mu)_{AB} \phi_B(k) \tag{3.19}$$

where we first used the 4-dimensional 2π-periodic delta function $\delta_P^{(4)}$ and used its periodicity to flip some signs, then defined $S_A^\mu = e^{i(\pi_A)_\mu}$ and finally defined the 16×16 matrices Ξ_μ:

$$(\Xi_\mu)_{AB} = S_\mu^A \delta_P^{(4)}(\pi_{\zeta_\mu} + \pi_A + \pi_B) \tag{3.20}$$

By using the position-space action of S_μ as in Eq. (3.4) with Eqs. (3.14), (3.15), one can implement sequential shifts $S_\mu S_\nu$ and $S_\nu S_\mu$ on fields $\chi(x)$, and show that:

$$\{S_\mu, S_\nu\} : \quad \chi(x) \longrightarrow 2\delta_{\mu\nu} \chi(x + \mu + \nu) \tag{3.21}$$

which means that shifts over two lattice spacings wipe out any phases. But it also leads to:

$$\{\Xi_\mu, \Xi_\nu\} = 2\delta_{\mu\nu} \times 1_{16} \tag{3.22}$$

This means that the Ξ_μ generate a group isomorphic to $\mathbf{\Gamma}_4$, which is the group generated by the Dirac γ_μ matrices. We will return to this point later.

Let us now pause the discussion on the symmetries for a bit and address the following question: How can we see that the staggered action leads to 4 degenerate quark excitations?

We define a different kind of shift operator, called T_μ, which is not a symmetry of the staggered action, but plays a role nevertheless:

$$T_\mu : \quad \chi(x) \rightarrow \eta_\mu(x)\chi(x+\mu) \tag{3.23}$$

One can now follow the same steps as for S_μ, define 4-vectors π_{η_μ} as:

$$\begin{aligned} \pi_{\eta_1} &= (0,0,0,0) \\ \pi_{\eta_2} &= (\pi,0,0,0) \\ \pi_{\eta_3} &= (\pi,\pi,0,0) \\ \pi_{\eta_4} &= (\pi,\pi,\pi,0) \end{aligned} \tag{3.24}$$

to write:

$$\eta_\mu(x) = e^{i\pi_{\eta_\mu}\cdot x} \tag{3.25}$$

and show that:

$$T_\mu : \quad \phi_A(k) \rightarrow e^{ik_\mu}(\Gamma_\mu)_{AB}\phi_B(k) \tag{3.26}$$

with:

$$(\Gamma_\mu)_{AB} = S_\mu^A \delta_P^{(4)}(\pi_{\eta_\mu} + \pi_A + \pi_B) \tag{3.27}$$

Again, by using position space, we can show that:

$$\{\Gamma_\mu, \Gamma_\nu\} = 2\delta_{\mu\nu} \times 1_{16} \tag{3.28}$$

$$[\Gamma_\mu, \Xi_\nu] = 0 \tag{3.29}$$

Thus, the Γ_μ also generate a group isomorphic to $\mathbf{\Gamma}_4$, and they commute with Ξ_μ. In order to see the quark excitations of the theory, we have to write down the free quark propagator in momentum space– and this is why Γ_μ are needed– and identify the poles.

One can read the free propagator in momentum space by writing the action in momentum space and then identifying the free propagator as the inverse of the kernel of the action. By writing the free version of Eq. (2.44) together with Eq. (3.25) one can write the free staggered action S_0 in momentum space:

$$S_{F,0}[\bar{\chi},\chi] = \frac{1}{2}\int_p \int_q \bar{\chi}(p)\big(\sum_\mu \delta_P^{(4)}(q-p+\pi_{\eta_\mu})(e^{iq_\mu}-e^{-ip_\mu}) + m\delta_P^{(4)}(q-p)\big)\chi(q) \tag{3.30}$$

By writing the $\delta_P^{(4)}$ as a product of four δ_P functions, one will see that, since $(\pi_{\eta_\mu})_\mu = 0$, one has $p_\mu = q_\mu$. Therefore:

$$S_{F,0}[\bar{\chi},\chi] = \int_p \int_q \bar{\chi}(p)\big(\sum_\mu \delta_P^{(4)}(q-p+\pi_{\eta_\mu}) i\sin(q_\mu) + m\delta_P^{(4)}(q-p)\big)\chi(q) \tag{3.31}$$

We see here that the action is not diagonal in the momenta p, q. This can be made possible through the expansion of Eq. (3.17):

$$q = k + \pi_A, \quad p = l + \pi_B, \quad A, B = 1, \ldots, 16 \tag{3.32}$$

Since $q - p \in (-\pi/2, 3\pi/2]$, we have $k_\mu - l_\mu \in (-\pi/2, \pi/2]$ and we can write:

$$\delta_P^{(4)}(q-p+\pi_{\eta_\mu}) \equiv \delta_P^{(4)}(k-l+\pi_A-\pi_B+\pi_{\eta_\mu}) = \delta_P^{(4)}(k-l)\delta_P^{(4)}(\pi_A-\pi_B+\pi_{\eta_\mu}) \tag{3.33}$$

By flipping signs of π vectors and by using that $\sin(q_\mu) \equiv \sin(k_\mu + \pi_A) = e^{i(\pi_A)_\mu}\sin(k_\mu) = S_\mu^A \sin(k_\mu)$ we write the action as:

$$\begin{aligned} S_{F,0}[\bar{\chi},\chi] &= \int_p \int_q \bar{\phi}_A(l)\delta_P^{(4)}(k-l)\big(\sum_\mu S_\mu^A \delta_P^{(4)}(\pi_A+\pi_B+\pi_{\eta_\mu}) i\sin(k_\mu) + m\delta_{AB}\big)\phi_B(k) \\ &= \int_p \int_q \bar{\phi}_A(l)\delta_P^{(4)}(k-l)\big(\sum_\mu i(\Gamma_\mu)_{AB}\sin(k_\mu) + m\delta_{AB}\big)\phi_B(k) \end{aligned} \tag{3.34}$$

which leads to a free staggered quark propagator $G_0(k)$:

$$G_0^{-1}(k) = \sum_\mu i(\Gamma_\mu)\sin(k_\mu) + m \tag{3.35}$$

This propagator has only 1 pole, since $k_\mu \in (\pi/2, \pi/2]$, but the action (3.34) involves the 16-component fields ϕ. However, since Γ_μ furnish a representation of $\mathbf{\Gamma}_4$, we can find a unitary transformation V that turns Γ_μ into a direct product of matrices in irreducible representations (irreps) of $\mathbf{\Gamma}_4$. This group has 16 one-dimensional irreps and one 4-dimensional one, which is spanned by products of Dirac γ_μ. It turns out[3] that we can write:

$$V\Gamma_\mu V^\dagger = \gamma_\mu \times 1_4 \tag{3.36}$$

We can then define 4-dimensional spinors:

$$\psi(k) = V\phi(k), \quad \bar{\psi}(k) = \bar{\phi}(k)V^\dagger \tag{3.37}$$

and write the staggered action as:

$$S_{F,0}[\bar{\psi}_i, \psi_i] = \sum_{i=1,2,3,4} \int_p \int_q \bar{\psi}_i(l)\delta_P^{(4)}(k-l)\Big(\sum_\mu i\gamma_\mu \sin(k_\mu) + m\Big)\psi_i(k) \tag{3.38}$$

which corresponds to an action of 4 degenerate quarks. An inspection of Eqs. (3.34), (3.38) allows us to deduce that Γ_μ correspond to the spin and Ξ_μ to the taste degrees of freedom. Therefore, the shifts $\hat{S}_\mu$ involve a taste transformation and the shifts $\hat{T}_\mu$ involve a spin transformation.

3.2 Mesons with staggered quarks

Having discussed the symmetries of the staggered action, we can address the problem of building operators to perform meson spectroscopy with staggered quarks. This problem was first solved in [Golterman, 1986b], following an earlier treatment of baryons [Golterman and Smit, 1985]. Since the taste adds a layer of complexity to the problem, we can first talk about a simpler system, namely the pure $SU(3)$ theory and the glueball excitations.

3.2.1 Glueball spectroscopy

Glueballs are the hypothetical, i.e. not experimentally observed, gluonic massive physical states within the pure Yang-Mills $SU(3)$ theory. They have been, and still remain, the topic of several lattice studies, since they are supposed to occur at strong couplings. Our discussion is based on [Berg and Billoire, 1983].

---

[3] Formally, one needs to project the basis vectors of the 16-dimensional representation of Γ_μ into the 4-dimensional representation of γ_μ, and use these new vectors as columns to build the basis transformation V (see Chapter 3-18 of [Hamermesh, 1962]). A clever way to bypass this process and build the matrix V is given in [van den Doel and Smit, 1983].

The goal is to build gluonic gauge-invariant lattice operators, which excite lattice states that can be related to the desired continuum glueball states. Then, by measuring correlation functions of these operators, one can draw conclusions about the continuum states, such as their mass.

As explained in [Weinberg, 2005], the continuum states can be labeled by J^{PC}, where J labels the angular momentum $SU(2)_s$, P the parity and C the charge conjugation.

The lattice gauge action is not invariant under the full Lorentz group, but only under hypercubic rotations by $\pi/2$ and discrete translations. A lattice operator therefore will not correspond to an irreducible representation (irrep) of $SU(2)$, labeled by a specific value of J, but of to an irrep of the cubic group $\mathbf{O}$. However, $\mathbf{O}$ is a subgroup of $SU(2)$ and one can perform what is called subduction, that is, one can express the irreps of $SU(2)$ that correspond to the subgroup $\mathbf{O}$ as a direct sum of irreps of $\mathbf{O}$.

Since we are interested in glueball states, only bosonic irreps of $SU(2)$ and $\mathbf{O}$ are relevant. The subduction of bosonic irreps was performed in [Altmann and Cracknell, 1965] and, up to $J = 5$ it reads[4]:

$$\begin{aligned}
D_0^{\mathbf{O}} &= A_1 \\
D_1^{\mathbf{O}} &= T_1 \\
D_2^{\mathbf{O}} &= E \oplus T_2 \\
D_3^{\mathbf{O}} &= A_2 \oplus T_1 \oplus T_2 \\
D_4^{\mathbf{O}} &= A_1 \oplus E \oplus T_1 \oplus T_2 \\
D_5^{\mathbf{O}} &= E \oplus 2T_1 \oplus T_2
\end{aligned} \tag{3.39}$$

By looking at these relations, we can see that if e.g. we build an operator that transforms as A_2, then the lowest state that we can access with a correlation function corresponds to $J = 3$. Now, this is not the whole story, since we have to include P and C, so let's see how this is done.

The full lattice Yang-Mills symmetry group is:

$$G(S_\mu, R_{\kappa\lambda}, P, C) \tag{3.40}$$

---

[4] See also Chapter 9-4 of [Hamermesh, 1962].

where S_μ are the shifts, $R_{\kappa\lambda}$ the rotations, P the parity and C the charge conjugation. The notation $G(A_1, A_2, \dots)$ means a group generated by the operators $A_1, A_2, \dots$. The subgroup that interests us for operator classification is the Rest Frame (RF_{YM}) subgroup:

$$\begin{aligned} RF_{YM} &= G(R_{kl}, P, C) \\ &= \mathbf{O} \times \{1, P\} \times \{1, C\} \\ &= \mathbf{O}_h \times \{1, C\} \end{aligned} \tag{3.41}$$

Let's start with $\mathbf{O}_h$ and consider spatial Wilson loops of size 4 (i.e. plaquettes) denoted by $O_i^{(1)}$. If one disregards orientations of the loops, there are 3 such loops, 1 in each plane of the 3-dimensional space. By acting on all $O_i^{(1)}$ with all 48 elements of $\mathbf{O}_h$, we see that they transform among themselves and we can build a 3-dimensional representation of $\mathbf{O}_h$, which is reducible. Then, we can consider plane rectangular Wilson loops, dentoted by $O_i^{(2)}$. There are 6 of those, so by using them we can build a 6-dimensional reducible representation of $\mathbf{O}_h$, and so on for Wilson loops of higher length.

Incorporating C is straightforward, given the following observation. We know that gauge fields A_μ behave under charge conjugation C in the following way:

$$A_\mu \xrightarrow{C} -A_\mu^T \tag{3.42}$$

Therefore for any Wilson loop of some shape s, $O_i^{(s)}$, we find:

$$O_i^{(s)} \xrightarrow{C} (O_i^{(s)})^\dagger \tag{3.43}$$

We can therefore extend the representations of $\mathbf{O}_h$ to RF_{YM} by considering:

$$\begin{aligned} &O_i^{(s)} + (O_i^{(s)})^\dagger \quad \text{for } \tau = +1 \\ &O_i^{(s)} - (O_i^{(s)})^\dagger \quad \text{for } \tau = -1 \end{aligned} \tag{3.44}$$

where τ is the eigenvalue of C. This means that with plaquettes we can build a 6-dimensional representation of RF_{YM}, with rectangles a 12-dimensional one etc.

One then has to reduce these representations into their irreducible contents, and see which irreps they involve. Using the orthogonality of characters, we can show that the positive integer a_μ that defines the contribution of the irrep μ to the given reducible representation is:

$$a_\mu = \frac{1}{g} \sum_i g_i (\chi_i^\mu)^* \chi_i \tag{3.45}$$

where g is the number of elements of the group, g_i the number of elements in the i-th conjugacy class, χ_i^μ the character of the i-th class in the μ-th irrep, and χ_i the character of the i-th class in the reducible representation that we started with.

For example, as we read from [Berg and Billoire, 1983], the 12-dimensional representation that is built from rectangles, involves the irreps $A_1^{++}, A_2^{++}, E^{++}, T_1^{+-}, T_2^{+-}$, where the R^{PC} denotes the R^P irrep of $\mathbf{O}_h$ and the 1-dimensional irrep (eigenvalue) of C.

The next step towards operator construction is the projection of the basis of the initial reducible representation into the space of the desired irrep. Say, for example, that we want to build an operator that transforms according to E^{++} out of rectangular Wilson loops. Since this irrep is 2-dimensional, there will be 2 such operators, which we can denote by $\psi[E^{++}]_i$, for $i = 1, 2$. We need any one vector ψ from the basis of the initial, reducible representation (there are 12 of them, for rectangles), together with the knowledge of the action of all RF_{YM} elements R on it ($\psi \longrightarrow \hat{R}\psi$). We also need the diagonal elements $D[E^{++}]_{ii}(R)$ of the irrep for all R. Then the projection reads:

$$\psi[E^{++}]_i = \frac{n[E^{++}]}{g} \sum_R D[E^{++}]_{ii}(R)\hat{R}\psi \tag{3.46}$$

where $n[E^{++}] = 2$ is the dimension of the irrep, and g is the number of group elements (for RF_{YM} it equals 96).

Finally, if one is interested in states with zero spatial momentum, one has to sum the resulting operator over the entire timeslice.

By measuring correlation functions of $\psi[E^{++}]_i$ one can extract energy levels of the continuum glueball state $J^{PC} = 2^{++}$, as can be seen from Eq. (3.39). Now, whether building the operator out of rectangles and not out of plaquettes or Wilson loops of higher size is the right choice has to do with the signal-to-noise behavior of the correlator.

3.2.2 Staggered mesons

The complexity for hadrons composed of staggered fermions stems, of course, from the coupling between taste and spacetime transformations.

The relevant part of the full staggered symmetry group, as described at the beginning of the chapter, is:

$$G(S_\mu, R_{\kappa\lambda}, I_s, C_0, \Omega_q) \tag{3.47}$$

We are specifically interested in the subgroup that corresponds to states of zero spatial momentum. There are two ways of finding this subgroup and its irreps. The first one is the formal way, through induction and the use of the corresponding little group, presented in [Golterman, 1986a] and in [Kilcup and Sharpe, 1987]. The second one, used in [Golterman and Smit, 1985] and [Golterman, 1986b], is tailored for zero momentum and is more intuitive; its equivalence to the formal construction is shown in [Golterman, 1986a].

In order to sketch the second way, we need to define translation operators $\mathcal{T}_\mu$ that do not involve taste. These can be defined as the squares of the shifts S_μ, $\mathcal{T}_\mu = S_\mu^2$, which commute, as seen in Eq. (3.21). One can use the $\mathcal{T}_\mu$, for example, to define zero-momentum quark fields, which, as we know, result from summing over all $\chi(\mathbf{x}, \tau)$ on a timeslice with trivial phases:

$$\sum_{\mathbf{m}} \mathcal{T}_1^{-m_1}\mathcal{T}_2^{-m_2}\mathcal{T}_3^{-m_3}\chi(\mathbf{x}, \tau)\mathcal{T}_1^{m_1}\mathcal{T}_2^{m_2}\mathcal{T}_3^{m_3} = \sum_{\mathbf{m}} \chi(\mathbf{x} + 2\mathbf{m}a, \tau) \equiv \chi_A(\tau) \tag{3.48}$$

where the index $A = 1, \ldots, 8$ labels the corners of the elementary cube that $\mathbf{x}$ runs over.

We can decouple taste transformations from shifts by defining the taste transformation operators Ξ_μ as:

$$\Xi_\mu = S_\mu \mathcal{T}_\mu^{-1/2} \tag{3.49}$$

The objects $\hat{\mathcal{T}}_\mu^{-1/2}$ are non-local in position space and their definition is more natural in momentum space. First, by using Eq. (3.19), we can write:

$$\begin{aligned} \mathcal{T}_i : &\quad \phi_A(k) \rightarrow e^{2ik_i}\phi_A(k) \quad \text{and} \\ \mathcal{T}_4 : &\quad \phi_A(k) \rightarrow e^{-2E}\phi_A(k) \end{aligned} \tag{3.50}$$

where $\mathcal{T}_4$, the transfer matrix, is defined with the Minkowski space energy E.[5]Then one can define:

$$\mathcal{T}_i^{-1/2}: \quad \phi_A(k) \to e^{-ik_i}\phi_A(k) \quad \text{and} \tag{3.51}$$

$$\mathcal{T}_4^{-1/2}: \quad \phi_A(k) \to e^{E}\phi_A(k) \tag{3.52}$$

which in turn leads to:

$$\Xi_i: \quad \phi_A(k) \to (\Xi_i)_{AB}\phi_B(k) \quad \text{and} \tag{3.53}$$

$$\Xi_4: \quad \phi_A(k) \to (\Xi_4)_{AB}\phi_B(k) \tag{3.54}$$

Using the Ξ_μ we can can define the Rest Frame (RF) subgroup of the staggered group as:

$$RF = G(\Xi_\mu, R_{kl}, I_s, C_0, \Omega_q) \tag{3.55}$$

We observe, from the definitions in Eqs. (3.49) and (3.50), that at zero momentum the spatial shifts S_m coincide with the taste transformations Ξ_m. This means that in Eq. (3.48) applying a shift to $\chi_A(\tau)$ only rearranges the A-components and attaches phases inside the **m**-sum, exactly in the way that a taste transformation does. This simplifies operator construction, as we will see later.

The task is to express the group RF in the simplest possible form, so that the construction of its irreps becomes easy. The quark number $U(1)$ transformations Ω_q act as in the continuum, so we can disregard them. For baryons, we can also disregard C_0.

If we want to further simplify the group, we need to define a taste-independent parity P (which will also help with labeling continuum states), since I_s does not commute with Ξ_μ. To see this, and to see how P should be defined, we have to look at the momentum-space action of I_s. From Eq.

---

[5] See Chapter 1 of [Montvay and Munster, 1997].

(3.9) we find:

$$\begin{aligned}
I_s : \quad \chi(x) &\to \eta_4(x)\chi(-\mathbf{x}, x_4) \\
\Rightarrow \int_{p\in BZ} e^{ip\cdot x}\chi(p) &\to \int_{p\in BZ} e^{-i\mathbf{p}\cdot\mathbf{x}+p_4x_4+i\pi_{\eta_4}\cdot x}\chi(p) \\
\Rightarrow \chi(p) &\to \chi(\hat{I}_s p + \pi_{\eta_4}) \\
\Rightarrow \phi_A(k) &\to \phi_C(\hat{I}_s k)\delta^{(4)}(\pi_A + \pi_C + \pi_{\eta_4}) \\
&= e^{i(\pi_B)_4}e^{-i(\pi_B)_4}\delta^{(4)}\delta(\pi_B + \pi_A)(\pi_B + \pi_C + \pi_{\eta_4})\phi_C(\hat{I}_s k) \\
&= e^{i(\pi_A)_4}\delta^{(4)}\delta(\pi_A + \pi_B)(\Gamma_4)_{BC}\phi_C(\hat{I}_s k) \\
&= e^{i(\pi_A)_4}\delta^{(4)}\delta(\pi_A + \pi_B + \pi_{\zeta_4})(\Gamma_4)_{BC}\phi_C(\hat{I}_s k) \\
&= (\Xi_4)_{AB}(\Gamma_4)_{BC}\phi_C(\hat{I}_s k) \qquad (3.56)
\end{aligned}$$

where we used the 2π-periodicity multiple times and, in the last step, the fact that π_{ζ_4} has all 4 components equal to 0.

Therefore, all we need to do is define the parity as:

$$P = \Xi_4 I_s = I_s \Xi_4 \qquad (3.57)$$

and thus its action in momentum space is:

$$P : \quad \phi_A(k) \to (\Gamma_4)_{AB}\phi_B(I_s k) \qquad (3.58)$$

For completeness, although without proof, let us give the momentum space action of spacetime rotations:

$$R_{\mu\nu} : \quad \phi_A(k) \to e^{\frac{\pi}{4}\Gamma_\mu\Gamma_\nu}\Big|_{AB} e^{\frac{\pi}{4}\Xi_\mu\Xi_\nu}\Big|_{BC}\phi_C(R^{-1}_{\mu\nu}k) \qquad (3.59)$$

chiral transformations:

$$\begin{aligned}
\Omega_\beta : \quad \phi_A(k) &\to e^{i\beta\Gamma_5\Xi_5}\Big|_{AB}\phi_B(k) \qquad (3.60) \\
\bar{\phi}_A(k) &\to \bar{\phi}_B(k)e^{i\beta\Gamma_5\Xi_5}\Big|_{BA} \qquad (3.61)
\end{aligned}$$

and of charge conjugation:

$$C_0: \quad \phi_A(k) \to (\Gamma_5)_{AB}(\Xi_5)_{BC}\bar{\phi}_C(-k) \tag{3.62}$$

$$\bar{\phi}_A(k) \to -(\Gamma_5)_{AB}(\Xi_5)_{BC}\phi_C(-k) \tag{3.63}$$

All of the above are momentum dependent, since they act on the label of the hypercube corner.

In order to further study RF we need to mention that, as with $\mathbf{O}_h$, it has fermionic and bosonic representations. In the fermionic representations the taste transformations $D(\Xi_\mu)$ anticommute, whereas in the bosonic representations they commute. With q being the quark number, we can write:

$$D(\Xi_\mu)D(\Xi_\nu) = e^{i\pi q}D(\Xi_\nu)D(\Xi_\mu) \tag{3.64}$$

In the case of baryons, we know that $q = 3$, and we disregard Ω_q transformations. We can furthermore disregard C_0, since in fermionic representations it anticommutes with P and therefore we can only pick one of those two to label baryonic states. We end up with the Geometric Rest Frame group denoted by GRF, which is the relevant subgroup for baryon state classification:

$$\begin{aligned} GRF &= G(\Xi_\mu, R_{kl}, I_s) \\ &\cong G(\Xi_\mu, R_{kl}, P) \\ &= G(\Xi_\mu, R_{kl}) \times \{1, P\} \end{aligned} \tag{3.65}$$

where we used Eq. (3.57).

In the case of mesons we have $q = 0$, but we cannot disregard C_0, since in bosonic representations it commutes with parity P and therefore should be well defined in mesonic states. We can define the bosonic taste transformations $X_\mu = D(\Xi_\mu)$ which commute, and this property is inherited by all other operators that involve taste transformations. We denote the mesonic Rest Frame group by RF_m:

$$RF_m = (X_\mu, R_{kl}, I_s, C_0) \tag{3.66}$$

Before we mention anything else about irreps of RF_m, we have to say some things about mesonic states and mesonic operators. Regarding the states, we need to find a maximal set of commuting operators within RF_m in order to properly label them. We want one of these operators to be X_4, for reasons that will become apparent in a bit. As for the other operators in the set, we can identify them by rewriting RF_m:

$$\begin{aligned}
RF_m &= G(X_\mu, R_{kl}, I_s) \times \{1, C_0\} \\
&= G(X_\mu, R_{kl}) \times \{1, P\} \times \{1, C_0\} \\
&= G(X_m, R_{kl}) \times \{1, X_4\} \times \{1, P\} \times \{1, C_0\} \\
&= G(X_i X_j, R_{kl}) \times \{1, X_1 X_2 X_3\} \times \{1, X_4\} \times \{1, P\} \times \{1, C_0\} \\
&\equiv \overline{RF} \times \{1, X_1 X_2 X_3\} \times \{1, X_4\} \times \{1, P\} \times \{1, C_0\}
\end{aligned} \tag{3.67}$$

where the first, third and fourth steps are unique to bosonic representations and commuting X_μ. The only step that would be relevant for fermions too is the second one, since we can always trade I_s for P, which commutes with all Ξ_μ and R_{kl}. So we can label the state as $|E\ \bar{\mathbf{r}}^{\sigma_t \sigma_{123}}, \sigma, \tau_0\rangle$, where:

$$\begin{aligned}
H|E\ \bar{\mathbf{r}}^{\sigma_t \sigma_{123}}, \sigma, \tau_0\rangle &= E|E\ \bar{\mathbf{r}}^{\sigma_t \sigma_{123}}, \sigma, \tau_0\rangle \\
\Xi_1 \Xi_2 \Xi_3 |E\ \bar{\mathbf{r}}^{\sigma_t \sigma_{123}}, \sigma, \tau_0\rangle &= \sigma_{123}|E\ \bar{\mathbf{r}}^{\sigma_t \sigma_{123}}, \sigma, \tau_0\rangle \\
\Xi_4 |E\ \bar{\mathbf{r}}^{\sigma_t \sigma_{123}}, \sigma, \tau_0\rangle &= \sigma_t|E\ \bar{\mathbf{r}}^{\sigma_t \sigma_{123}}, \sigma, \tau_0\rangle \\
P|E\ \bar{\mathbf{r}}^{\sigma_t \sigma_{123}}, \sigma, \tau_0\rangle &= \sigma|E\ \bar{\mathbf{r}}^{\sigma_t \sigma_{123}}, \sigma, \tau_0\rangle \\
C_0|E\ \bar{\mathbf{r}}^{\sigma_t \sigma_{123}}, \sigma, \tau_0\rangle &= \tau_0|E\ \bar{\mathbf{r}}^{\sigma_t \sigma_{123}}, \sigma, \tau_0\rangle
\end{aligned} \tag{3.68}$$

where $\bar{\mathbf{r}}$ denotes the irrep of $\overline{RF}$.

The mesonic operators that we aim to find are defined on a time slice and transform according to the Geometrical Time Slice group (GTS), defined as:

$$GTS = G(\Xi_m, R_{kl}, I_s) \tag{3.69}$$

Specifically for bosonic representations, where C_0 is relevant, the group becomes:

$$\begin{aligned}
GTS_m \times \{1, C_0\} &= G(X_m, R_{kl}, I_s) \times \{1, C_0\} \\
&= \overline{RF} \times \{1, X_1 X_2, X_3\} \times \{1, I_s\} \times \{1, C_0\}
\end{aligned} \tag{3.70}$$

and therefore we can construct time slice operators $\Phi(t)$ which transform as $(\bar{\mathbf{r}}^{\sigma_s \sigma_{123}}, \tau_0)$. Since from Eq. (3.57) we know the relation between I_s, P and Ξ_4 eigenvalues, we can write:

$$\langle E\ \bar{\mathbf{r}}^{\sigma_t \sigma_{123}}, \sigma, \tau_0 | \Phi(t) | 0 \rangle = 0, \quad \text{unless } \sigma_t = \sigma \sigma_s \tag{3.71}$$

Since we are limited to building operators $\Phi(t)$ that transforms as irreps of GTS_m and not RF_m, we expect them to excite mesonic states with both values of σ, and we will see this in more detail in a bit.

Determining the irreps $\bar{\mathbf{r}}^{\sigma_s \sigma_{123}}$ of GTS_m comes down to determining irreps $\bar{\mathbf{r}}$ of $\overline{RF}$, since $GTS_m = \overline{RF} \times \{1, X_1X_2, X_3\} \times \{1, I_s\}$. Then, by taking appropriate linear combinations of the operators $\Phi(t)$ that transform within those $\bar{\mathbf{r}}$, one can accommodate I_s and $X_1X_2X_3$, as with C in the glueball case.

The group $\overline{RF}$ has the structure of a semidirect product, in which the taste transformations X_iX_j (i.e. shifts S_iS_j, in case of zero momentum) are the normal subgroup. It has 96 elements (which can be immediately seen, since $G(R_{kl})$ has 24 and $\{1, X_1X_2, X_1X_3, X_2X_3\}$ has 4 elements) that are contained in 10 classes. Therefore it has 10 nonequivalent irreps. The method of finding irreps of groups with a semidirect-product structure is explained in [Jansen and Boon, 1967], and specifically for crystal groups in [Birman, 1984].

As with Wilson loops of fixed shape in the case of glueballs, we need to find classes of operators that transform among themselves when acted upon with elements of GTS_m, so that we can use them as a basis of a representation. Such classes can be generated by using the operators:

$$\begin{aligned}
O_0 &= \sum_{\mathbf{m}} \bar{\chi}(2\mathbf{m}) \chi(2\mathbf{m}) \\
O_1 &= \sum_{\mathbf{m}} \bar{\chi}(2\mathbf{m}) D_1 \chi(2\mathbf{m}) \\
O_{12} &= \sum_{\mathbf{m}} \bar{\chi}(2\mathbf{m}) D_1 D_2 \chi(2\mathbf{m}) \\
O_{123} &= \sum_{\mathbf{m}} \bar{\chi}(2\mathbf{m}) D_1 D_2 D_3 \chi(2\mathbf{m})
\end{aligned} \tag{3.72}$$

as starting points. Here we have used the central difference:

$$D_i \chi(x) = \frac{1}{2}(\chi(x + a\hat{i}) - \chi(x - \hat{a}i) \tag{3.73}$$

The classes can be generated by acting on these operators with spatial rotations, spatial shifts and spatial inversions. Then, one has to project the operators of a class, just like Eq. (3.46), into irreps of GTS_m. The irreps that we expect to find in mesonic states are 20, that is, 5 irreps of $\overline{RF}$ dressed with four combinations of σ_{123}, σ_s each. Specifically, with **8** being the (fermionic) fundamental representation of GTS, one finds:

$$\mathbf{8} \times \mathbf{8} = \sum_{\sigma_{123},\sigma_s} (\mathbf{1}^{\sigma_{123}\sigma_s} + \mathbf{3}^{\sigma_{123}\sigma_s} + \mathbf{3}''^{\sigma_{123}\sigma_s} + \mathbf{3}''''^{\sigma_{123}\sigma_s} + \mathbf{6}^{\sigma_{123}\sigma_s}) \tag{3.74}$$

where the bold numbers of the RHS denote irreps of $\overline{RF}$ with the corresponding dimensionality. The primes help differentiate between irreps of the same dimensionality. It has to be mentioned that the bosonic irreps of GTS are the only irreps of GTS_m, therefore, when we talk about irreps of GTS in the context of mesons we equivalently talk about irreps of GTS_m.

One will, however, observe that with the use of the operators listed in Eqs. (3.72), per combination of $\bar{\mathbf{r}}$, σ_s, σ_{123} only one value of τ_0 is accessible, so one can access only half of the relevant irreps. For the other half, one should consider operators that are time-split, i.e. $\bar{\chi}$ is separated by χ by one step in the temporal direction– but this is not important to us at this stage.

We now need to discuss how we should interpret the measurements of the staggered meson correlation functions. We are interested in the connected correlation function $\langle \Phi(\tau)\overline{\Phi}(0)\rangle_c$. We can use S_4 to express $\Phi(\tau)$, on a periodic lattice with a temporal extent equal to L_τ:

$$\Phi(\tau) = S_4^{L_\tau - \tau}\Phi(0)S_4^{\tau} \tag{3.75}$$

With the arguments of Sec. 2.2, we can here assume that the vacuum energy is zero and we can express the connected correlator as a trace, while remembering that operators Φ can couple to states with two pairs of values of σ and σ_t, such that $\sigma\sigma_t = \sigma_s$:

$$\begin{aligned}\langle \Phi(\tau)\overline{\Phi}(0)\rangle_c = &\sum_{E,\sigma} \langle E\ \bar{\mathbf{r}}^{\sigma_t\sigma_{123}}, \sigma, \tau_0 | S_4^{L_\tau-\tau}\Phi S_4^{\tau}|0\rangle\langle 0|\overline{\Phi}|E\ \bar{\mathbf{r}}^{\sigma_t\sigma_{123}}, \sigma, \tau_0\rangle \\ &+ \sum_{E,\sigma} \langle 0|S_4^{L_\tau-\tau}\Phi S_4^{\tau}|E\ \bar{\mathbf{r}}^{\sigma_t\sigma_{123}}, \sigma, \tau_0\rangle\langle E\ \bar{\mathbf{r}}^{\sigma_t\sigma_{123}}, \sigma, \tau_0|\overline{\Phi}|0\rangle\end{aligned} \tag{3.76}$$

From the third of Eqs. (3.68), along with Eqs. (3.49), (3.50) we can write:

$$S_4|E\ \bar{\mathbf{r}}^{\sigma_t\sigma_{123}}, \sigma, \tau_0\rangle = \sigma_t e^{-E}|E\ \bar{\mathbf{r}}^{\sigma_t\sigma_{123}}, \sigma, \tau_0\rangle \tag{3.77}$$

Therefore:

$$\begin{aligned}\langle\Phi(\tau)\overline{\Phi}(0)\rangle_c &= \sum_{E,\sigma}\langle E\,\bar{\mathbf{r}}^{\sigma_t\sigma_{123}},\sigma,\tau_0|\Phi|0\rangle\langle 0|\overline{\Phi}|E\,\bar{\mathbf{r}}^{\sigma_t\sigma_{123}},\sigma,\tau_0\rangle\sigma_t^{L_\tau-\tau}e^{-E(L_\tau-\tau)}\\ &+\sum_{E,\sigma}\langle 0|\Phi|E\,\bar{\mathbf{r}}^{\sigma_t\sigma_{123}},\sigma,\tau_0\rangle\langle E\,\bar{\mathbf{r}}^{\sigma_t\sigma_{123}},\sigma,\tau_0|\overline{\Phi}|0\rangle\sigma_t^{\tau}e^{-E\tau}\end{aligned}\tag{3.78}$$

In order to proceed we have to use the fact that this correlation function should be invariant under charge conjugation.

As we can see from the definition (3.13), and as we also know from continuum,[6] application of C_0 involves a phase chosen by convention. For fields Φ and $\overline{\Phi}$ we can write:

$$C_0\Phi C_0^{-1}=\tau_0\overline{\Phi},\quad C_0\overline{\Phi}C_0^{-1}=\bar{\tau}_0\Phi\tag{3.79}$$

For the fields χ and $\bar{\chi}$ themselves, these phases would be $\epsilon(x)$ and $-\epsilon(x)$ respectively. However, the application of C_0^2 does not depend on convention and the resulting phase is $\sigma_c=\tau_0\bar{\tau}_0=(-1)^q$, i.e. $+1$ for bosons and -1 for fermions. We therefore have, using Eq. (3.79):

$$\begin{aligned}&\langle C_0^{-1}\Phi(\tau)C_0C_0^{-1}\overline{\Phi}(0)C_0\rangle_c\equiv\sigma_c\langle\overline{\Phi}(\tau)\Phi(0)\rangle_c\\ &=\sigma_c\sum_{E,\sigma}\langle E\,\bar{\mathbf{r}}^{\sigma_t\sigma_{123}},\sigma,\tau_0|\overline{\Phi}|0\rangle\langle 0|\Phi|E\,\bar{\mathbf{r}}^{\sigma_t\sigma_{123}},\sigma,\tau_0\rangle\sigma_t^{L_\tau-\tau}e^{-E(L_\tau-\tau)}\\ &+\sigma_c\sum_{E,\sigma}\langle 0|\overline{\Phi}|E\,\bar{\mathbf{r}}^{\sigma_t\sigma_{123}},\sigma,\tau_0\rangle\langle E\,\bar{\mathbf{r}}^{\sigma_t\sigma_{123}},\sigma,\tau_0|\Phi|0\rangle\sigma_t^{\tau}e^{-E\tau}\end{aligned}\tag{3.80}$$

By demanding that (3.78) and (3.80) be equal, we find:

$$\langle E\,\bar{\mathbf{r}}^{\sigma_t\sigma_{123}},\sigma,\tau_0|\Phi|0\rangle\langle 0|\overline{\Phi}|E\,\bar{\mathbf{r}}^{\sigma_t\sigma_{123}},\sigma,\tau_0\rangle=\sigma_c\langle E\,\bar{\mathbf{r}}^{\sigma_t\sigma_{123}},\sigma,\tau_0|\overline{\Phi}|0\rangle\langle 0|\Phi|E\,\bar{\mathbf{r}}^{\sigma_t\sigma_{123}},\sigma,\tau_0\rangle\tag{3.81}$$

---

[6] See, for example, Chap. 3 of [Peskin and Schroeder, 1995].

and so Eq. (3.78) becomes:

$$
\begin{aligned}
\langle \Phi(\tau)\overline{\Phi}(0)\rangle_c &= \sum_{E,\sigma} \langle 0|\Phi|E\ \overline{\mathbf{r}}^{\sigma_t\sigma_{123}}, \sigma, \tau_0\rangle\langle E\ \overline{\mathbf{r}}^{\sigma_t\sigma_{123}}, \sigma, \tau_0|\overline{\Phi}|0\rangle \\
&\quad \times \left[\sigma_t^\tau e^{-E\tau} + \sigma_c \sigma_t^{L_\tau-\tau} e^{-E(L_\tau-\tau)}\right] \\
&= \sum_{E,\sigma} \mathcal{A}_\sigma(E_\sigma\ \overline{\mathbf{r}}^{\sigma_t\sigma_{123}}, \tau_0) \\
&\quad \times (\sigma\sigma_s)^\tau \left[e^{-E_\sigma\tau} + \sigma_c(\sigma\sigma_s)^{L_\tau-2\tau} e^{-E_\sigma(L_\tau-\tau)}\right] \\
&= \sum_{E_+} \mathcal{A}_+(E_+\ \overline{\mathbf{r}}^{\sigma_t\sigma_{123}}, \tau_0)\sigma_s^\tau \left[e^{-E_+\tau} + e^{-E_+(L_\tau-\tau)}\right] \\
&\quad + \sum_{E_-} \mathcal{A}_-(E_-\ \overline{\mathbf{r}}^{\sigma_t\sigma_{123}}, \tau_0)(-1)^\tau\sigma_s^\tau \left[e^{-E_-\tau} + e^{-E_-(L_\tau-\tau)}\right]
\end{aligned}
\tag{3.82}
$$

where we explicitly indicated the dependence of the energy E on the parity σ, and we assumed even number of lattice points in the temporal direction.

Eq. (3.82) is exactly the functional form that we use to fit temporal correlators for staggered mesons. We can observe that, because of the factor $(-1)^\tau$, depending on the sign of σ_s, one of the two channels of (3.82) will have an oscillating behavior, but we will talk more about all that in Sec. 5.3.

In the continuum, as we can read from Eq. (3.34), the staggered action with 2 degenerate flavors of quarks is invariant under $SO(4)_r \times SU(8)_{f+t}$, where r indicates 4-dimensional Euclidean rotations and $f + t$ indicates the combined flavor and taste symmetry. However, since for physical mesonic states the 4-fold taste degeneracy is not interesting, we can consider the $SU(2)_f \times SU(4)_t$ subgroup of $SU(8)_{f+t}$, of which the $SU(2)_f$ part is handled as in the continuum.[7] We are therefore interested in classifying states with respect of the continuum rest frame group $RF_{m,cont}$, which involves the spin-$SU(2)$ and the taste-$SU(4)$:

$$
RF_{m,cont} = SU(2)_s \times SU(4)_s \times \{1, P\} \times \{1, C\} \tag{3.83}
$$

where C the continuum charge conjugation, which is related to C_0 in a well-defined way but let us

---

[7] By doing this, we ignore a class of states where flavor and taste are intermixed, but correspond to correct continuum states. But this is not a problem, if one is after basic spectroscopic calculations.

not get into this. Its irreps can be denoted by:

$$\big(J, R\big)^{\sigma\tau} \tag{3.84}$$

with τ the eigenvalue of C, J the label of the $SU(2)_s$ irrep, R the label of the $SU(4)_t$ irrep, which is either the singlet S or the adjoint A, and σ the P eigenvalue.

In order to map the lattice RF_m states to continuum $RF_{m,cont}$ states, we need to perform subductions, like the ones of Eqs. (3.39). Only, now, because of the existence of taste, one needs to perform a chain of subductions, by following a chain of subgroups that leads from $RF_{m,cont}$ to $\mathbf{O}$, and since the subduction of RF_m with respect to $\mathbf{O}$ is unique[8], this chain will give the subduction of $RF_{m,cont}$ with respect to RF_m.

The issue is the embedding of $\mathbf{O}$ into $SU(2)_s \times SU(4)_t$ is not unique, so one has to find the proper way. One observes in Eq. (3.59) that the spatial lattice rotations are a discreet subgroup of the diagonal $SU(2)_{diag}$ subgroup of $SU(2)_s \times SU(2)_t$. It is diagonal in the sense that the spin and the taste parts of the rotations of Eq. (3.59) are identical. Now, as it is claimed in [Golterman and Smit, 1985], this $SU(2)_t$ is embedded in $SU(4)_t$ in a block diagonal way[9], and one can therefore consider the following chain of subgroups:

$$SU(2)_s \times SU(4)_t \supset SU(2)_s \times SU(2)_t \supset SU(2)_{diag} \supset \mathbf{O} \tag{3.85}$$

where parity and charge where omitted because the lattice counterparts have a direct continuum interpretation.

For taste-singlet states, $(j, S)^{\sigma\tau}$, there is a shortcut: Since continuum tastes are blind to taste, one can perform the subduction directly between $SU(2)_s$ and $\mathbf{O}$, as in the glueball case. For taste-adjoint states, there is a different simplification, as one can express them as:

$$(J, S)^{\sigma_1\tau_1} \times (0, A)^{\sigma_2\tau_2} = (J, A)^{\sigma_1\sigma_2\ \tau_1\tau_2} \tag{3.86}$$

so that one can utilize the existing taste-singlet subduction and perform the remaining subduction with only $J = 0$ taste-adjoint representations.

---

[8] See Table 1 of [Golterman, 1986b].

[9] In the language of [Golterman and Smit, 1985], the fundamental representation of $SU(4)$ is expressed as $\mathbf{4} = \mathbf{\frac{1}{2}} + \mathbf{\frac{1}{2}}$.

Let us here mention an example of a mesonic operator O_{S4T4}:

$$O_{S4T4} = \sum_{\mathbf{x}\text{: even}} \eta_4(x)\zeta_4(x)\bar{\chi}(x)\chi(x) \tag{3.87}$$

This operator will appear from the class of O_0 of Eqs. (3.72). It transforms as $\mathbf{1}^{+-}$ of GTS, and excites two states of opposite parity σ. To see which ones they are, we need to go to momentum space, where we see that O_{S4T4} corresponds to:

$$\bar{\phi}_A\,(\Gamma_4\Xi_4)_{AB}\,\phi_B \tag{3.88}$$

which, after diagonalization, can be written as:

$$\bar{\psi}^t_\alpha\,(\gamma_4)_{\alpha\beta}\,(\xi_4)_{tt'}\,\psi^{t'}_\beta \tag{3.89}$$

and we can denote this state by $\gamma_4\xi_4$. Now, when we go to momentum space we make the operator non-local in time and we solve the ambiguity by implicitly choosing a parity. This one corresponds to $\sigma = +1$, by looking at the action of parity in momentum space in Eq. (3.58). The $\sigma = -1$ state can be identified as follows: We find an operator that commutes with all operators involved in RF except P. This, by inspection of Eqs. (3.53), (3.54), (3.58), (3.59), (3.62), (3.63), should be $\Gamma_4\Gamma_5\Xi_4\Xi_5$. Therefore the two states that O_{S4T4} excites are, in spin-taste notation, $\gamma_4\xi_4$ and $\gamma_5\xi_5$. In the continuum the correspond, respectively to $(0,A)^{+-}$ and $(0,A)^{-+}$.

There is something interesting about both of these states. Regarding $\gamma_5\xi_5$, it corresponds to the chiral transformation $\Omega_\beta(x)$ defined in Eqs. (3.11), (3.62), (3.63). In a 2-flavor massless theory, the staggered action is invariant under the chiral transformation:

$$\chi(x) \rightarrow e^{i\beta\epsilon(x)\tau_i}\chi(x) \tag{3.90}$$

$$\bar{\chi}(x) \rightarrow \bar{\chi}(x)e^{i\beta\epsilon(x)\tau_i} \tag{3.91}$$

where now $\chi(x)$ is a doublet and τ_i the $SU(2)$ generators. We can show[10] that in the interacting staggered theory, the conserved current associated to this symmetry is:

$$J^5_{i,\mu}(x) = \frac{1}{4}\eta_\mu(x)\epsilon(x)\left(\bar{\chi}(x+\hat{\mu})\tau_i U^\dagger_\mu(x)\chi(x) + \bar{\chi}(x)\tau_i U_\mu(x)\chi(x+\hat{\mu})\right) \tag{3.92}$$

---

[10] Probably the most complete description of conservation laws in the context of lattice gauge theories is in [Montvay and Munster, 1997].

As we can read from the phases, the spin-taste structure of this current is $\tau_i \gamma_\mu \gamma_5 \xi_5$. Therefore, from Goldstone's theorem, each of these 3 currents can create a massless pion from the vacuum:

$$\langle 0 | J^5_{i,\mu}(x) | \pi_i(p) \rangle = i p_\mu f_\pi e^{-ip\cdot x} \tag{3.93}$$

with f_π being the pion decay constant. Since $\gamma_4\gamma_5\xi_5$ has the same C, P quantum numbers as $\gamma_5\xi_5$, this state will correspond to a Goldstone particle, which, in absence of explicit mass terms, will be massless. If a mass term is present in the staggered action, this state will still be the lightest state in the spectrum. It can be seen in Eq. (3.93) that at zero spatial momentum, the three currents with $\mu = 1, 2, 3$ do not excite the Goldstone pions from the vacuum.

We now turn to the $\gamma_4\xi_4$ state. It can be proven that $\gamma_\mu\xi_4$ is the spin-taste structure of a conserved current J_μ in the staggered theory, and corresponds to a symmetry which is not spontaneously broken. Therefore the charge Q defined as:

$$Q = \int d^3x J_4(x) \tag{3.94}$$

destroys the vacuum. Since a zerom-momentum operator that corresponds to $\gamma_4\xi_4$ is proportional to Q, it cannot excite a state and we expect our lattice operator O_{S4T4} to couple to only the $\sigma = -1$ state at zero momentum, which is the Goldstone pion.

3.3 Mass renormalization of staggered quarks

In order to study the renormalization of the quark mass, which enters the action as in Eq. (2.44), we need to study the quark self energy $\Sigma(p)$. In addition to the continuum-type sunset diagram, there is, as is usually the case on the lattice, a p-independent tadpole contribution. The evaluation of these was done in [Golterman and Smit, 1984] and in papers cited there, and a simplified description is offered in the lecture notes [Golterman, 2024]. The method used was splitting the momentum integration in two regions, $|k| < \delta$ and $|k| > \delta$. In the inner region, we can expand around small a and we get a continuum-like expression with a logarithmic divergence in the cutoff δ. In the outer region, we get, as expected, the same divergence with the opposite sign, together with terms:

$$g^2 \left(p_\mu X_\mu + \frac{1}{a} Y_0 + mY \right) \tag{3.95}$$

By demanding that $\Sigma(p)$ be invariant under the symmetries of the action, we can constrain the three coefficients X_μ, Y_0, Y. The symmetry under shifts S_μ causes the three coefficients to not contain any Ξ_μ matrices. Then, symmetry under inversions I_s means that X_μ is proportional to Γ_μ. The scalar Y_0, on the other hand, can only be a number since it cannot contain Ξ_μ and since $\Gamma_\mu\Gamma_\mu = 1$. Now, the self energy should be invariant under the chiral transformations of Eqs. (3.60), (3.61). If we write $\Sigma_{AB}(p)$ as $\langle\phi_A(-p)\bar{\phi}_B(p)\rangle$ then an infinitesimal chiral transformation will cause:

$$\Sigma \to \Sigma + i\beta\Gamma_5\Xi_5\Sigma + i\beta\Sigma\Gamma_5\Xi_5 \tag{3.96}$$

and therefore invariance of Σ means anticommutation with $\Gamma_5\Xi_5$. This requires Y_0 to be zero and therefore the only renormalization of the mass is of the continuum type, that is, multiplicative.

3.4 Improved staggered actions

As in the case of the Wilson gauge action, discussed in Sec. 2.3.3, improvement means removing cutoff effects to bring observables closer to the scaling regime, in the language of Eq. 2.64. The improvement, as mentioned, affects both the action and the observable, however, improving the action alone reduces part of the cutoff effects.

With staggered fermions, specifically, a major source of cutoff effects is the taste breaking, that is, the exchange of gluons of momentum π/a that have a taste-changing effect on the quarks, since the poles of the quark propagators are located at the 16 corners of the Brillouin zone. The taste breaking is manifested e.g. in the pion taste splittings: A pion with spin taste structure $\gamma_5\xi_X$, where ξ_X can be any product of ξ_μ matrices, will have different mass for different ξ_X at finite a because of the gluon exchanges. This will be studied in more detail in Chap. 5.

If one writes down the Feynman rules for the staggered theory, one will see that there are two types of quark-gluon vertices: The 2-quark, 1-gluon vertex V and the 2-quark, 2-gluon vertex W, which vanishes in the continuum. We can already see that in order for taste changing to happen, there have to be two quark lines connected by gluons. At tree level this can only happen with two V vertices, so we will disregard W at tree level.

In order to write Feynman rules and do perturbation theory, we need to restore the coupling g

in the links U (lattice units are assumed, and no powers of a appear):

$$U_\mu = e^{igA_\mu} = 1 + igA_\mu - \frac{1}{2}g^2A_\mu^2 + O(g^3) \tag{3.97}$$

and of course remove it from in front of the gauge action. The interaction term of the action that involves the vertex V reads:

$$S_V[\bar{\chi}, \chi, A] = \int_{p,q,k} \bar{\chi}(q)V_\mu(p, q, k)A_\mu(k)\chi(p) \tag{3.98}$$

with

$$V_\mu(p, q, k) = -ig\delta_P^{(4)}(p + k - q + \pi_{\eta_\mu})\frac{e^{ip_\mu} + e^{-iq_\mu}}{2} \tag{3.99}$$

If $k_\mu = \pi$ then $q_\mu = p_\mu + \left(\pi_{\eta_\mu}\right)_\mu + \pi = p_\mu + \pi$ and V becomes proportional to $\sin(p_\mu)$ which is small for small (i.e. physical) p_μ. Therefore, vertices with gluons A_μ with longitudinal momentum equal to π are suppressed by construction.

The contribution from gluons with hard transverse momenta can be suppressed by suppressing the field $A_\mu(k)$ itself for these values of k, with a process introduced in [Blum et al., 1997], [Orginos and Toussaint, 1999], [Orginos et al., 1999], [Lepage, 1999], with increasing complexity.

Let k have all components physical except k_{ν_1}, $\nu_1 \neq \mu$, for which $k_{\nu_1} = \pi$. If we smear the links U_μ with the higher-order 3-staples:

$$\begin{aligned} U_\mu(x) \to U_\mu(x) + \frac{1}{4}\sum_{\nu\neq\mu} \Big(& U_\nu(x)U_\mu(x + \hat{\nu})U_\nu^\dagger(x + \hat{\mu}) \\ & + U_\nu^\dagger(x - \hat{\nu})U_\mu(x - \hat{\nu})U_\nu(x - \hat{\nu} + \hat{\mu}) - 2U_\mu(x)\Big) \end{aligned} \tag{3.100}$$

then we can see that the gluon fields A_μ are replaced by:

$$\begin{aligned} A_\mu(k) \to A_\mu(k) + \frac{1}{4}\sum_{\nu\neq\mu} \big(& 2A_\mu(k)\left(\cos(k_\nu) - 1\right) \\ & + 4\sin(k_\mu/2)\sin(k_\nu/2)A_\nu(k)\big) \end{aligned} \tag{3.101}$$

and if one carries out the algebra, one can see that indeed $A_\mu(k)$ is suppressed. This smearing process is also known as Fat3. By then performing 5-staple and 7-staple smearing, one can suppress gluons two and with all three transverse momentum components being hard. The total smearing is called Fat7.

In order to achieve an $O(a^2)$ improvement to the staggered action, there are two more steps, beyond the Fat7 smearing. Firstly, one extra smearing has to be implemented, to remove the effect introduced by the 3-staple, which is of $O(a^2)$. This planar 5-staple is known as Lepage term, as it was introduced in [Lepage, 1999]. Secondly, the derivative of the Dirac operator itself has to be corrected, by adding the Naik term [Naik, 1989], producing the so-called fat links and the long links.

Another issue has to be mentioned here, although no detail will be given. In unimproved lattice QCD simulations, the links are not close to 1, so Eq. (3.97) is not a good approximation. This was studied in [Lepage and Mackenzie, 1993], where the tadpole factors u_0 were introduced. If one divides all links U by u_0, one brings the expansion of Eq. (3.97) closer to the truth and if this correction is implemented in an action then this action is called tadpole-improved.[11] If the tadpole improvement is used in the Fat7+Lepage+Naik, then the resulting action is called ASQTAD. In the ASQTAD action the taste-breaking effects of $O(a^2)$ are removed, and they are pushed to $O(\alpha_s a^2)$.

Schematically, if U_μ is the original link and $\mathcal{F}^{F7L}$ the smearing operator that implements Fat7+Lepage, we can write:

$$V_\mu = \mathcal{F}^{F7L} U_\mu \tag{3.102}$$

Then, for the Naik improvement, the lattice covariant derivative acting on a fermionic field χ is modified as:

$$\begin{aligned}\nabla_\mu[V]\chi(x) &= \frac{1}{2}\Big(V_\mu(x)\chi(x+\hat{\mu}) - V_\mu^\dagger(x-\hat{\mu})\chi(x-\hat{\mu})\Big)\\ &\to \left(1+\frac{1}{8}\right)\Big(V_\mu(x)\chi(x+\hat{\mu}) - V_\mu^\dagger(x-\hat{\mu})\chi(x-\hat{\mu})\Big)\\ &+ \frac{1}{48}\Big(U_\mu(x)U_\mu(x+\hat{\mu})U_\mu(x+2\hat{\mu})\chi(x+3\hat{\mu})\\ &- U_\mu^\dagger(x-\hat{\mu})U_\mu^\dagger(x-2\hat{\mu})U_\mu^\dagger(x-3\hat{\mu})\chi(x-3\hat{\mu})\Big)\end{aligned} \tag{3.103}$$

---

[11] In language of Feynman diagrams, the lattice tadpoles are the ones to be blamed, since they are suppressed only by the coupling and not the lattice spacing. Hence the name of the improvement.

These products of 3 links that appear are the long links, and as we can see, the original links U are used in their construction. The tadpole factors are have to be properly accounted for, but this is of secondary importance and can be found in [Lepage, 1999].

The HISQ action that we use was introduced in [Follana et al., 2007], and was found to reduce taste-breaking effects even further than the ASQTAD. The motivation behind the HISQ action was to suppress the $O(\alpha_s a^2)$ taste breaking effects, which are particularly important for heavy quarks. These effects are, of course, 1-loop effects. It had been observed that the source of these effects are the neighboring, unsmeared links that participate in the Fat7 process, and therefore, two sequential Fat7 smearings should correct for those. However, doing this introduces new errors, and it was found in [Follana et al., 2007] that the correct way to go about multiple smearings is to reunitarize the link, i.e. project it on the $SU(3)$ group, between the two Fat7 smearings. The reunitarization can be carried out analytically. It has been shown that when reunitarization is present, tadpole improvement is not needed.

As in the ASQTAD case, we can give a schematic description of the HISQ action construction process:

$$\begin{aligned} U_\mu &\to V_\mu = \mathcal{F}^{F7} U_\mu \\ V_\mu &\to W_\mu = \mathcal{U} V_\mu = \mathcal{U}\mathcal{F}^{F7} U_\mu \\ W_\mu &\to X_\mu = \mathcal{F}^{F7L} W_\mu = \mathcal{F}^{F7L}\mathcal{U}\mathcal{F}^{F7} U_\mu \end{aligned} \tag{3.104}$$

where $\mathcal{U}$ is the reunitarization operator. It can be noticed that the Lepage term is implemented only in the second smearing application. Finally, similarly to the ASQTAD case, the fat links X_μ^F are constructed out of the fully smeared X_μ links, and the long links X_μ^L are constructed out of the reunitarized W_μ links. The HISQ action (with a single quark flavor) is:

$$S^{HISQ}[\chi, \bar{\chi}, U] = \sum_{x,y} \left(\bar{\chi}(x) D^{HISQ}[U](x,y) \chi(x) + m\delta^{(4)}(x-y) \bar{\chi}(x) \chi(y) \right) \tag{3.105}$$

with the HISQ Dirac operator defined as:

$$
\begin{aligned}
D^{HISQ}[U](x,y) = \frac{1}{2}\sum_{\mu=1}^{4}\eta_\mu(x)\Big\{ & X^F_{x,\mu}[U]\delta^{(4)}(x+\hat{\mu}-y) - X^{F\dagger}_{x-\hat{\mu},\mu}[U]\delta^{(4)}(x-\hat{\mu}-y) \\
& + (1+\epsilon(am))\Big(X^L_{x,\mu}[U]\delta(x+3\hat{\mu}-y) - X^{L\dagger}_{x-3\hat{\mu},\mu}[U]\delta^{(4)}(x-3\hat{\mu}-y)\Big)\Big\}
\end{aligned}
\tag{3.106}
$$

where ϵ corrects for large quark masses. For u, d, s quarks we can set it to zero. It needs to be stressed that the gauge path-integration is always in terms of the original, unsmeared, links U. Up to the introduction of anisotropy, Eq. (3.106) is the action we use in our simulations for the quark sector. One can see, e.g. in [Bazavov et al., 2010a] that indeed the HISQ action helps significantly reduce the taste breaking effects. Finally, the RHMC for the HISQ action is discussed in Sec. 4.4.

CHAPTER 4

QCD ON ANISOTROPIC LATTICES

Anisotropic lattices have been used for studies in lattice QCD since the early days of the field [Hasenfratz and Hasenfratz, 1981, Karsch, 1982]. The anisotropy is introduced naturally within the path-integral formulation of a quantum field theory on a discretized spacetime grid, as the temporal and spatial lattice spacings appear for different reasons, and therefore need not be equal, e.g., [Rothe, 2012]. The introduction of anisotropy adds complexity to the tuning of lattice ensembles, since the tuning of the couplings and quark masses is now entangled with the anisotropy parameters that appear in the action. For that reason, anisotropic simulations are less common than the isotropic ones. The recent work employing anisotropic ensembles includes thermodynamics, glueball and hadronic spectroscopy and spectral reconstruction [Smecca et al., 2025, Jiang et al., 2023, Lombardo et al., 2025]. Apart from the early attempts with the anisotropic naive staggered fermions in the early 2000s [Nomura et al., 2004, Levkova et al., 2006], the present large-scale anisotropic simulations employ only Wilson fermions.

4.1 Gauge anisotropy

In the following the lattice spacing in the spatial directions is denoted a_σ and in the temporal one a_τ. We refer to the ratio $\xi = a_\sigma/a_\tau$ of these dimensionful quantities as the renormalized anisotropy. To achieve different lattice spacings, one needs an additional bare parameter in the action, namely the bare gauge anisotropy, denoted here by ξ_0. The introduction of anisotropy in a lattice gauge action is quite standard with the details fully worked out in the early work by Karsch [Karsch, 1982]. We use the anisotropic tree-level Symanzik-improved gauge action

$$\begin{aligned} S_G &= \beta\frac{1}{\xi_0}\left(c_P\sum_{P_{\sigma\sigma}}\left(1-\frac{1}{3}\mathrm{ReTr}(P_{\sigma\sigma})\right)+c_R\sum_{R_{\sigma\sigma}}\left(1-\frac{1}{3}\mathrm{ReTr}(R_{\sigma\sigma})\right)\right) \\ &+ \beta\xi_0\left(c_P\sum_{P_{\sigma\tau}}\left(1-\frac{1}{3}\mathrm{ReTr}(P_{\sigma\tau})\right)+c_R\sum_{R_{\sigma\tau}}\left(1-\frac{1}{3}\mathrm{ReTr}(R_{\sigma\tau})\right)\right), \end{aligned} \tag{4.1}$$

where the sums are over all 1×1 and 1×2 Wilson loops in all possible orientations, denoted P and R, respectively. The indices $\sigma\sigma$ ($\sigma\tau$) represent spatial-spatial (spatial-temporal) orientations, and

$c_P = 1$, $c_R = -1/20$ and $\beta = 10/g^2$. This is the standard Lüscher-Weisz action of Eq.(2.65), with c_0 combined with β for convenience.

Mapping the bare parameters (β, ξ_0) to the dimensionful quantities (a_σ, a_τ), or, equivalently, to (a_σ, ξ), requires an analog of the usual lattice scale setting procedure, modified to provide two quantities. In general, one computes a physical quantity that allows for separating spatial and temporal direction e.g., differently oriented Wilson loops as in the Klassen method [Klassen, 1998]) and imposes that it is the same in physical units in both directions, thus fixing (a_σ, a_τ). As the use of the gradient flow is now a more common and more convenient practice to set the scale [Lüscher, 2010] and anisotropy, as was first proposed in [Borsanyi et al., 2012b], we also use it for determining the spatial lattice spacing and the renormalized anisotropy, as described next.

4.2 Anisotropic gradient flow

The gradient flow, first introduced in the lattice context in [Luscher, 2010] and as a scale setting procedure in [Lüscher, 2010], was extended to anisotropic case in [Borsanyi et al., 2012b]. The original procedure of [Borsanyi et al., 2012b] was later slightly modified [Borsanyi et al., 2018] to make it more computationally efficient. (The procedure of [Borsanyi et al., 2012b] requires several gradient flows per lattice, while the one of [Borsanyi et al., 2018] only one flow.) We experimented with both procedures, and having observed no qualitative differences, preferred the computationally cheaper one of [Borsanyi et al., 2018].

Let the flow anisotropy be denoted ξ_0^{gf} and the gradient flow equation for the flowed lattice gauge links $U_\mu(x,t)$ be written in the following way:

$$\frac{dU_\mu}{dt} = Z_\mu U_\mu, \quad Z_\mu(x,t) = -\sum_{\nu\neq\mu} \rho_{\mu\nu} \mathcal{P}_A\left[U_\mu(x,t) S^\dagger_{\mu\nu}[U](x,t)\right] \tag{4.2}$$

where t is the flow time, $S_{\mu\nu}$ is the staple arising from taking the group derivative of the flow action, $\mathcal{P}_A$ denotes traceless antihermitean projection

$$\mathcal{P}_A(V) = \frac{1}{2}(V - V^\dagger) - \frac{1}{6}\mathrm{Tr}(V - V^\dagger) \tag{4.3}$$

and the weight factors $\rho_{\mu\nu}$

$$\rho_{i4} = (\xi_0^{gf})^2, \quad \rho_{ij} = \rho_{4i} = 1 \tag{4.4}$$

make the flow anisotropic in the spatial and temporal directions in lattice units.

As an observable, one can choose the flowed spatial and temporal action densities, similar to the original isotropic proposal [Lüscher, 2010]:

$$S_{\sigma\sigma}(t) = \frac{1}{4}\sum_{x,i\neq j} F_{ij}^2(x,t)\,, \qquad S_{\sigma\tau}(t) = \frac{1}{2}\sum_{x,i} F_{i4}^2(x,t) \tag{4.5}$$

with a suitable discretization of the field strength tensor, or their derivatives with respect to the flow time, since those are less affected by the discretization effects, as was first noted in [Borsanyi et al., 2012a]. In the anisotropic case the scale setting conditions for the two scales $w_{0,\sigma}$, $w_{0,\tau}$ now are

$$\left[t\frac{d}{dt}t^2\langle S_{\sigma\sigma}(t)\rangle\right]_{t=w_{0,\sigma}^2} = 0.15, \qquad (\xi_0^{gf})^2\left[t\frac{d}{dt}t^2\langle S_{\sigma\tau}(t)\rangle\right]_{t=w_{0,\tau}^2} = 0.15\,. \tag{4.6}$$

If one fixes the target renormalized anisotropy ξ at some value, e.g., $\xi = 2$, and sets the gradient flow anisotropy to that value $\xi_0^{gf} = \xi$, the only remaining free parameter is the bare gauge anisotropy ξ_0 (we consider the bare gauge coupling β fixed at this stage). Then ξ_0 is adjusted until the following additional scale setting condition is met

$$\frac{w_{0,\sigma}}{w_{0,\tau}} = 1. \tag{4.7}$$

When the condition (4.7) is met, the renormalized gauge anisotropy of the ensemble generated at the bare parameters (β, ξ_0) is defined to be that fixed value of ξ. While adjusting ξ_0 means generating gauge field ensembles at various values of ξ_0 (which is needed at the tuning stage when the parameter space is not yet mapped out anyway), there is only one flow per ensemble to be run–at the target anisotropy ξ.

4.3 Fermion anisotropy

To introduce anisotropy in the fermion part of the action, we can start with a generic form of the Dirac operator. The action is

$$S_F = a_\sigma^3 a_\tau \sum_{x,y} \bar{\tilde{\psi}}(x)\tilde{M}(x,y)\tilde{\psi}(y) \tag{4.8}$$

where the summation is over the lattice volume and $\tilde{M}(x,y) = \tilde{D}(x,y) + m\delta^{(4)}(x-y)$. The color and spinor indices are suppressed for brevity. The tilde sign indicates that the quantities are dimensionful. The Dirac operator is decomposed into the spatial and temporal parts $\tilde{D}(x,y) = \tilde{D}_\sigma(x,y) + \tilde{D}_\tau(x,y)$, where all matrices are of the same dimension and in the spatial (temporal) part the temporal (spatial) gauge links are set to zero. To make the quantities dimensionless, appropriate factors of the spatial and temporal lattice spacing are introduced:

$$\psi = a_\sigma\sqrt{a_\tau}\,\tilde{\psi}, \quad D_\sigma(x,y) = a_\sigma\tilde{D}_\sigma(x,y), \quad \xi D_\tau(x,y) = \xi a_\tau\tilde{D}_\tau(x,y) = a_\sigma\tilde{D}_\tau(x,y) \tag{4.9}$$

This assignment of factors follows the convention that the fermion mass is measured in the units of the spatial lattice spacing, $a_\sigma m$. The dimensionless form of the action is then

$$S_F = \sum_{x,y}\bar{\psi}(x)M(x,y)\psi(y) = \sum_{x,y}\bar{\psi}(x)\left[D_\sigma(x,y) + \xi_0^f D_\tau(x,y) + a_\sigma m\delta^{(4)}(x-y)\right]\psi(y). \tag{4.10}$$

The replacement of ξ with ξ_0^f indicates that the quantity in the action is a bare parameter (subscript “0”), not necessarily equal to the target renormalized anisotropy ξ. Also, given that the discretization effects in the gauge and fermion sectors are of a different origin, this parameter is different (superscript “f”) from the bare gauge anisotropy ξ_0.

To relate ξ_0^f to the renormalized anisotropy, one needs to use observables sensitive to the fermion anisotropy. There are two common schemes:

- measure a state (e.g. a meson) at non-zero momentum $\vec{p}$ and fit the dispersion relation:

$$a_\tau^2 E^2(p^2) = a_\tau^2 E^2(0) + \frac{a_\sigma^2 p^2}{(\xi^f)^2}, \tag{4.11}$$

- measure a zero-momentum correlation function for, e.g., a meson with mass M, in the temporal and spatial directions and define the renormalized fermion anisotropy through the ratio of the extracted energy levels E_σ and E_τ

$$\xi^f = \frac{E_\sigma}{E_\tau} = \frac{a_\sigma M}{a_\tau M} = \frac{a_\sigma}{a_\tau}. \tag{4.12}$$

The bare quantity ξ_0^f is adjusted until $\xi^f = \xi$, the target renormalized anisotropy. We experimented with both approaches and prefer the first one. Our numerical setup is discussed in detail in Sec. 5.4. The second approach is illustrated in Appendix C.

So far the discussion has been generic and applies to any unsmeared Dirac operator. The spin Clifford algebra is realized for any staggered fermion formulation via phase factors $\eta_\mu(x)$ accompanying either forward or backward displacements by an odd number of steps $\delta^{(4)}(x \pm (2n+1)\hat{\mu} - y), n \in \mathbf{Z}$, together with some realization of the necessary parallel transporters $X_{x,\mu}[U]$:[1]

$$S^\gamma_\mu(x,y) \equiv \eta_\mu(x) X_{x,\mu}[U]\delta^{(4)}(x \pm \hat{\mu} - y), \quad \eta_\mu(x) \equiv (-1)^{\sum\limits_{\nu<\mu} x_\nu}. \tag{4.13}$$

These are the shifts of Eq. (3.23) in the interacting case. For the HISQ action the Dirac operator has the form of Eq. (3.106), where, as mentioned, the smeared links are constructed as $U_{x,\mu} \xrightarrow{Fat7} V_{x,\mu}$, $V_{x,\mu} \xrightarrow{proj\ U(3)} W_{x,\mu}$, $W_{x,\mu} \xrightarrow{Fat7} X^F_{x,\mu}$, and $W_{x,\mu} \xrightarrow{Naik} X^L_{x,\mu}$. As the HISQ action involves smearing, there is potentially some freedom in where the anisotropy can be introduced: before or after the smearing. However, as the Fat7 part of the smearing was designed to suppress the coupling to gluons with momenta at the corners of the Brillouin zone, the relative coefficients of the Fat3, Fat5 and Fat7 paths are fixed. Thus, to preserve that property (which is independent of anisotropy), we must introduce the fermion anisotropy at the outermost level:

$$\begin{aligned}
2D^{aHISQ}[U](x,y) = \sum_{\mu=1}^{3} \eta_\mu(x) \Big\{ & X^F_{x,\mu}[U]\delta^{(4)}(x+\hat{\mu}-y) - X^{F\dagger}_{x-\hat{\mu},\mu}[U]\delta^{(4)}(x-\hat{\mu}-y) \\
& + (1+\epsilon(a_\sigma m))\Big(X^L_{x,\mu}[U]\delta^{(4)}(x+3\hat{\mu}-y) - X^{L\dagger}_{x-3\hat{\mu},\mu}[U]\delta^{(4)}(x-3\hat{\mu}-y)\Big)\Big\} \\
& + \xi_0^f \eta_4(x) \Big\{ X^F_{x,4}[U]\delta^{(4)}(x+\hat{4}-y) - X^{F\dagger}_{x-\hat{4},4}[U]\delta^{(4)}(x-\hat{4}-y) \\
& + (1+\epsilon(a_\sigma m))\Big(X^L_{x,4}[U]\delta^{(4)}(x+3\hat{4}-y) - X^{L\dagger}_{x-3\hat{4},\mu}[U]\delta^{(4)}(x-3\hat{4}-y)\Big)\Big\}.
\end{aligned} \tag{4.14}$$

We call the action in Eq. (4.14) the anisotropic highly improved staggered quark (aHISQ) action.

This way of introducing the fermion anisotropy is also less demanding from the computational perspective, as the smearing and the major part of the fermion force, discussed in detail in Sec. 4.4 proceed in the same way for isotropic and anisotropic simulations.

---

[1] The parallel transporters can be links $U_\mu(x)$ or smeared links $X_{x,\mu}[U]$.

To better understand the taste symmetry breaking pattern and to crosscheck our code, we have also performed calculations with naive (i.e. unimproved) staggered fermions with the following anisotropic Dirac operator

$$2D^{naive}[U](x,y) = \sum_{\mu=1}^{3} \eta_\mu(x) \left\{ U_{x,\mu}\delta^{(4)}(x+\hat{\mu}-y) - U^\dagger_{x-\hat{\mu},\mu}\delta^{(4)}(x-\hat{\mu}-y) \right\}$$
$$+ \xi_0^f \eta_4(x) \left\{ U_{x,4}\delta^{(4)}(x+\hat{4}-y) - U^\dagger_{x-\hat{4},4}\delta^{(4)}(x-\hat{4}-y) \right\}. \qquad (4.15)$$

It is structurally the same as aHISQ, apart from the absence of the three-link hopping (Naik) term and the fact that the original gauge links $U_{x,\mu}$ are used.

4.4 Dynamical fermions with anisotropy

As in the isotropic dynamical HISQ simulations, we intend to use the Rational Hybrid Monte Carlo (RHMC) algorithm, that was introduced and developed in [Clark and Kennedy, 2004], [Clark and Kennedy, 2007a], [Clark and Kennedy, 2007b]. The main components of RHMC are the gauge and fermion forces, and the fermion matrix inverter. For aHISQ we an need anisotropic version of all the components. The gauge force is straightforward, and it was developed and tested in parallel with the anisotropic local updating algorithms for pure gauge ensembles that are discussed in Sec. 5.1.

The aHISQ inverter amounts to introducing proper anisotropy factors as shown in Eq. (4.10). Those can be taken care of by multiplying the HISQ smeared links immediately before the inversion. The conjugate gradient proceeds in exactly same way as for the isotropic case. The most complicated component is the fermion force: the anisotropy factors are on the outermost smearing level, however, the chain rule proceeds recursively outside-in. The anisotropy factors can be incorporated at the stage of constructing the outer products of pseudo-fermion fields. Structurally, the aHISQ fermion force is similar to HISQ, therefore we follow [Wong and Woloshyn, 2007] that spelled out the recursive chain rule expressions for multiply smeared actions, such as HISQ.

To simplify the discussion, it is enough to consider a single-smeared action, for instance, Fat7: $U_{x,\mu} \xrightarrow{Fat7} V_{x,\mu}$. We closely follow the discussion of [Wong and Woloshyn, 2007] in this part. The smeared links $V_{x,\mu}$ are constructed as weighted averages of the products of the original gauge links

$U_{x,\mu}$ along the paths of length up to 7. The Dirac operator for the anisotropic Fat7 action is[2]

$$D_{xy} = \sum_{\mu=1}^{3} \eta_{x,\mu} \left\{ V_{x,\mu}\delta_{x,y-\hat{\mu}} - V^{\dagger}_{x-\hat{\mu},\mu}\delta_{x,y+\hat{\mu}} \right\} + \xi_0^f \, \eta_{x,4} \left\{ V_{x,4}\delta_{x,y-\hat{4}} - V^{\dagger}_{x-\hat{4},4}\delta_{x,y+\hat{4}} \right\} \tag{4.16}$$

and the fermion matrix is $M_{xy} = D_{xy} + 2m\delta_{xy}$ (for convenience in the code M and D are redefined to be twice what they are in Eq. (4.10)).

For n_f fermion flavors the rooted staggered pseudofermion action is

$$S_{\Phi} = \langle \Phi | [M^{\dagger}M]^{-n_f/4} | \Phi \rangle. \tag{4.17}$$

In the RHMC algorithm the fractional power is approximated as

$$[M^{\dagger}M]^{-n_f/4} \approx \alpha_0 + \sum_{l} \frac{\alpha_l}{M^{\dagger}M + \beta_l} \tag{4.18}$$

and the fermion force, defined in Eq. (2.127), is

$$f^F_{x,\mu} = \frac{\delta S_{\Phi}}{\delta U_{x,\mu}} = -\sum_{l} \alpha_l \left\{ \left\langle X^l \left| \frac{\partial D^{\dagger}[V[U]]}{\partial U_{x,\mu}} \right| Y^l \right\rangle + \left\langle Y^l \left| \frac{\partial D[V[U]]}{\partial U_{x,\mu}} \right| X^l \right\rangle \right\}, \tag{4.19}$$

where $|X^l\rangle = [M^{\dagger}M + \beta_l]^{-1}|\Phi\rangle$ and $|Y^l\rangle = D|X^l\rangle$. The X^l and Y^l fields are defined on the even and odd sites, respectively, and they implicitly incorporate the anisotropy, as they are solutions to a linear system with the anisotropic Dirac operator. Using the chain rule,

$$\begin{aligned}
\frac{\partial D_{mn}}{\partial U_{x,\mu}} &= \sum_{y,\nu} \left[\frac{\partial D_{mn}}{\partial V_{y,\nu}} \frac{\partial V_{y,\nu}}{\partial U_{x,\mu}} + \frac{\partial D_{mn}}{\partial V^{\dagger}_{y,\nu}} \frac{\partial V^{\dagger}_{y,\nu}}{\partial U_{x,\mu}} \right], \\
\frac{\partial D^{\dagger}_{mn}}{\partial U_{x,\mu}} &= \sum_{y,\nu} \left[\frac{\partial D^{\dagger}_{mn}}{\partial V_{y,\nu}} \frac{\partial V_{y,\nu}}{\partial U_{x,\mu}} + \frac{\partial D^{\dagger}_{mn}}{\partial V^{\dagger}_{y,\nu}} \frac{\partial V^{\dagger}_{y,\nu}}{\partial U_{x,\mu}} \right],
\end{aligned} \tag{4.20}$$

where the derivatives $\partial V / \partial U$ depend only on the smearing and are not affected by the anisotropy. The other derivatives involve the anisotropy directly:

$$\begin{aligned}
\frac{\partial D_{mn}}{\partial V_{y,\nu}} &= \omega_{\nu}\eta_{m,\nu}\delta_{m,y}\delta_{m,n-\hat{\nu}}, \\
\frac{\partial D_{mn}}{\partial V^{\dagger}_{y,\nu}} &= -\omega_{\nu}\eta_{m,\nu}\delta_{m-\hat{\nu},y}\delta_{m,n+\hat{\nu}}, \\
\frac{\partial D^{\dagger}_{mn}}{\partial V_{y,\nu}} &= -\omega_{\nu}\eta_{n,\nu}\delta_{n-\hat{\nu},y}\delta_{n,m+\hat{\nu}}, \\
\frac{\partial D^{\dagger}_{mn}}{\partial V^{\dagger}_{y,\nu}} &= \omega_{\nu}\eta_{n,\nu}\delta_{n,y}\delta_{n,m-\hat{\nu}},
\end{aligned} \tag{4.21}$$

---

[2] In this section we will reduce the spacetime points to indices, to simplify the notation. They are indices, after all.

with

$$\omega_\nu = \begin{cases} 1, & \nu \neq 4, \\ \xi_0^f, & \nu = 4. \end{cases} \tag{4.22}$$

Substituting Eqs. (4.20) and (4.21) into Eq. (4.19) gives

$$\begin{aligned} [f^F_{x,\mu}]_{AB} &= \sum_y (-1)^y \Big[\sum_{\nu\neq 4} \eta_{y,\nu} \Big(\frac{\partial [V_{y,\nu}]_{CD}}{\partial [U_{x,\mu}]_{AB}} [f^{(0)}_{y,\nu}]_{CD} + \frac{\partial [V^\dagger_{y,\nu}]_{CD}}{\partial [U_{x,\mu}]_{AB}} [f^{(0)\dagger}_{y,\nu}]_{CD} \Big) \\ &+ \xi_0^f \, \eta_{y,4} \Big(\frac{\partial [V_{y,4}]_{CD}}{\partial [U_{x,\mu}]_{AB}} [f^{(0)}_{y,4}]_{CD} + \frac{\partial [V^\dagger_{y,4}]_{CD}}{\partial [U_{x,\mu}]_{AB}} [f^{(0)\dagger}_{y,4}]_{CD} \Big) \Big], \end{aligned} \tag{4.23}$$

which is an anisotropic generalization of Eq. (2.6) of [Wong and Woloshyn, 2007], and where

$$[f^{(0)}_{y,\nu}]_{CD} = \sum_l \alpha_l \big([Y^l_{y+\nu}]_D [X^{l*}_y]_C + [X^l_{y+\nu}]_D [Y^{l*}_y]_C \big). \tag{4.24}$$

The color indices are explicitly spelled out with capital roman letters.

The bare fermion anisotropy ξ_0^f multiplies the temporal component of $f^{(0)}_{x,\mu}$ and this suggests an economical practical implementation: multiply the outer product $|X\rangle\langle Y|$ by ξ_0^f when the corresponding sites are separated by a temporal link at the stage of constructing $f^{(0)}_{x,\mu}$. After that, the chain rule proceeds identically for the isotropic and anisotropic case.

4.5 Properties of the anisotropic staggered spectrum

Another Clifford algebra besides the one generated by Eq. (4.13) for the spin exists among the internal taste degrees of freedom. It is realized similarly via a different set of phase factors $\zeta_\mu(x)$:

$$S^\xi_\mu(x,y) \equiv \zeta_\mu(x) X_{x,\mu}[U] \delta^{(4)}(x \pm \hat{\mu} - y), \quad \zeta_\mu(x) \equiv (-1)^{\sum\limits_{\nu>\mu} x_\nu}, \tag{4.25}$$

These are the shifts of Eq. (3.4), generalized for the interacting theory, that are a symmetry of staggered fermion actions. As we have seen, in the free theory, the products of phases and displacements of either kind constitute two separate exact Clifford algebras, e.g.

$$\begin{aligned} S^\gamma_\mu(x,y) S^\gamma_\nu(y,z) + S^\gamma_\nu(x,y) S^\gamma_\mu(y,z) &= 2\delta_{\mu\nu} \delta^{(4)}(x \pm \hat{\mu} \pm \hat{\nu} - z), \qquad (4.26) \\ S^\xi_\mu(x,y) S^\xi_\nu(y,z) + S^\xi_\nu(x,y) S^\xi_\mu(y,z) &= 2\delta_{\mu\nu} \delta^{(4)}(x \pm \hat{\mu} \pm \hat{\nu} - z) \qquad (4.27) \end{aligned}$$

up to an overall two-step displacement, and elements from separate spin or taste Clifford algebras commute. Thus, Eq. (4.27) enforces exact sixteenfold degeneracies for the free staggered spectrum.

Yet in the interacting theory the displacements S^γ, S^ξ in Eqs. (4.13) and (4.25) are accompanied by parallel transporters $X_{x,\mu}[U]$ that do not commute. Hence, Wilson loop factors arise between the two paths in Eqs. (4.26) and (4.27) (if one factors out a common part of the paths), which cause mixing and lift degeneracies in the interacting staggered spectrum. These outcomes are irrespective of using forward or backward displacements, or of any particular choices for the parallel transporters.

Site-local operators are constructed by pairing corresponding elements of both Clifford algebras with one forward and one backward displacement, e.g. $S^\gamma_\mu(x, x \pm \hat{\mu}) S^\xi_\mu(x \mp \hat{\mu}, x)$, most notably in the spin-pseudoscalar taste-pseudoscalar case,

$$\epsilon_x \equiv S^\gamma_5(x, y) S^\xi_5(y, x) = (-1)^{\sum\limits_\mu x_\mu}, \tag{4.28}$$

which is the generator of the last remaining taste-isovector $U(1)_A$ chiral symmetry of any staggered fermion action. Because this symmetry is broken spontaneously in the interacting theory, the lowest pseudoscalar taste state excited by interpolating operators using ϵ_x is a Goldstone boson.

Any other taste of a pseudoscalar state needs further parallel transport on the taste end, by one step in the μ direction for $S^\xi_5(y, x) S^\xi_\mu(x, x \pm \hat{\mu})$, by one step each in the μ and ν directions for $S^\xi_5(y, x) S^\xi_\mu(x, x \pm \hat{\mu}) S^\xi_\nu(x \pm \hat{\mu}, x \pm \hat{\mu} \pm \hat{\nu})$, etc. Each of those additional steps involves gauge links that fluctuate at the lattice scale, less so if smeared. Their fluctuations, which are independent to a leading approximation, add positive contributions scaling as $(a\Lambda)^2$, where Λ represents a typical hadronic scale, to the respective taste hadron's squared energy. As such, the sixteenfold degeneracy breaks up in the interacting theory, and the spectrum is affected by taste-symmetry breaking. In improved staggered quark formulations using smoother links such as HISQ, i.e., Eq. (3.106), the link fluctuations are reduced, and thus the taste-symmetry breaking is diminished.

With respect to the taste quantum number, the meson multiplets are classified as pseudoscalar (denoted ξ_5 or P), axial vector ($\xi_\mu \xi_5$ or A), tensor ($\xi_\mu \xi_\nu$ or T), vector (ξ_μ or V) and scalar, or singlet (1 or S) [Golterman, 1986b]. A taste-multiplet hierarchy of $P < A < T < V < S$ with $1, 4, 6, 4, 1$-fold remnant degeneracies emerges for the tastes of pseudoscalar states due to the minimal count of fluctuating links involved in each of the interpolating operators. The Goldstone boson taste P

is the lowest and the taste singlet pseudoscalar boson taste S is the highest state. Since the pion mass is much smaller than the hadronic scale Λ, taste-symmetry breaking is a large effect for the taste pions. Because all other light hadrons have masses at the hadronic scale Λ, taste-symmetry breaking is only a modest effect for those.

On anisotropic lattices, the temporal links are smoother than the spatial links, and hence, the former fluctuate less than the latter. Thus, we are led to expect that a new taste-multiplet hierarchy $P \lesssim A_\tau < A_\sigma \lesssim T_{\sigma\sigma} < T_{\sigma\tau} \lesssim V_\sigma < V_\tau \lesssim S$ with $1, 1, 3, 3, 3, 3, 1, 1$-fold remnant degeneracies emerges at nontrivial anisotropy. In the limit of infinite anisotropy, i.e., vanishing temporal lattice spacing, the fluctuations of the temporal links become negligible, the taste matrix $S_4^\xi(x, x \pm \hat{4})$ does not change the energy anymore, and the approximate $\lesssim$ degeneracies become exact with a $2, 6, 6, 2$-fold degeneracy pattern.

CHAPTER 5

NUMERICAL RESULTS

To validate our code for anisotropic simulations, understand anisotropy tuning with the gradient flow and study the spectrum of anisotropic staggered quarks, we start with anisotropic pure gauge simulations. In the fully dynamical case that we are interested in, i.e., two degenerate light and one strange quark, one needs to tune four bare parameters simultaneously: the gauge coupling β, gauge anisotropy ξ_0, strange quark mass m_s (as is often done, we can fix the strange-to-light mass ratio, e.g., to $m_s/m_l = 5$), and the fermion anisotropy ξ_0^f. For quenched simulations the tuning splits into two independent steps: (β, ξ_0), then (m_s, ξ_0^f).

5.1 Pure gauge ensembles

We anticipate using ensembles with high anisotropy with Non-Relativistic QCD (NRQCD) formalism for heavy quarks. Therefore we are interested in relatively spatially coarse lattices. To keep the computational cost of the explorations modest, we start with the spatial lattice spacing $a_\sigma \sim 0.16 - 0.2$ fm and concentrate our simulations in that region of the parameter space to understand how the discretization effects influence anisotropy tuning and what anisotropies can practically be reached. (As is clear from Eq. (4.1), higher anisotropy is equivalent to stronger coupling in the magnetic part of the action.)

To generate anisotropic pure gauge ensembles we use the Cabibbo-Marinari SU(3) heatbath algorithm [Cabibbo and Marinari, 1982] that updates the three SU(2) subgroups. The SU(2) matrices are sampled with the Fabricius-Haan-Kennedy-Pendleton (FHKP) heatbath [Fabricius and Haan, 1984, Kennedy and Pendleton, 1985]. Per one step of the heatbath algorithm, four steps of overrelaxation [Adler, 1988] were performed. We also generated several test ensembles with the Hybrid Monte Carlo algorithm [Duane et al., 1987] to validate the anisotropic gauge force. Among a number of tests, the anisotropic pure gauge code was validated by reproducing some runs from [Namekawa et al., 2001], as discussed in Appendix E.

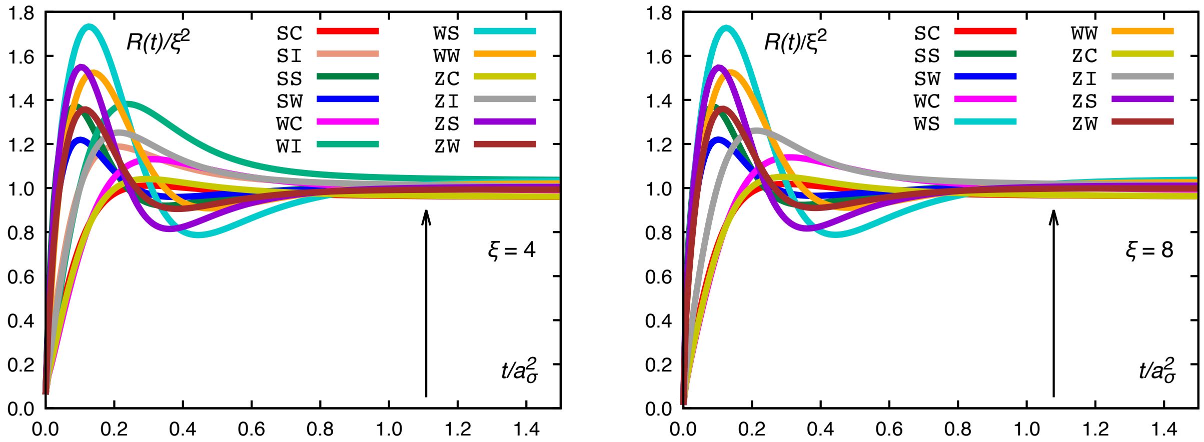

Figure 5.1 The ratio defined in Eq. (5.1) scaled with the renormalized anisotropy, $R(t)/\xi^2$, plotted as a function of flow time t/a_σ^2 for the renormalized anisotropy $\xi = 4$ (left) and $\xi = 8$ (right). The vertical lines correspond to $t = w_{0,\sigma}^2/a_\sigma^2$ with $a_\sigma \approx 0.1665$ fm. The lines of different color correspond to different flow-observable schemes. The errorbars are not visible on the scale of the figure.

5.2 Gauge anisotropy and lattice spacing tuning

To determine the spatial and temporal lattice spacing, (a_σ, a_τ), or, equivalently, the spatial lattice spacing and renormalized anisotropy, (a_σ, ξ), we use the gradient flow as described in Sec. 4.2. The discretization effects on the scale setting come from three origins: the gauge action used to generate the configurations, generator of the flow and the discretization of the observable, as is well known for the isotropic case [Fodor et al., 2014].

The gauge action is fixed to the tree-level Symanzik-improved one, Eq. (4.1). For the flow we use Wilson (W), tree-level Symanzik (S) action, and, in some cases, we also compute the Zeuthen flow (Z), which is a modification of the flow equation itself [Ramos and Sint, 2016]. For the observable we use Wilson (W), Symanzik (S), clover (C) [Sheikholeslami and Wohlert, 1985] and improved clover (I) [Bilson-Thompson et al., 2003] discretization. As the gauge action is fixed, we only denote flow-observable combinations with two-letter abbreviations, spanning [W,S,Z][W,S,C,I]. The early flow time artifacts are different for these combinations, and their severity limits how large the spatial lattice spacing may be so that the tuning procedure of Sec. 4.2 is still practical to use.

To assess the discretization effects on the anisotropy, which is determined through the ratio in Eq. (4.7), one can compute the evolution of the ratio of the energy densities defined in Eq. (4.6) themselves:

$$R(t) = t\frac{d}{dt}t^2\langle S_{\sigma\sigma}(t)\rangle \Bigg/ t\frac{d}{dt}t^2\langle S_{\sigma\tau}(t)\rangle \ . \tag{5.1}$$

When $w_{0,\sigma}/w_{0,\tau}$ is close to 1, $R(t)$ approaches ξ^2. In Fig. 5.1 the ratio $R(t)/\xi^2$ is shown for the two tuned ensembles that we use in this study, with same spatial lattice spacing $a_\sigma \approx 0.1665$ fm and the renormalized gauge anisotropy $\xi = 4$ (left panel) and $\xi = 8$ (right panel). The first important point the plots illustrate is that, as expected, at large anisotropies the discretization effects are determined by the spatial lattice spacing a_σ: the ratios $R(t)/\xi^2$ for the two ensembles behave almost identically. We have not measured the SI and WI combinations on the $\xi = 8$ ensemble (right panel), but we expect them also to be similar to the ones at $\xi = 4$ (left panel). The arrows indicate the flow time that corresponds to $a_\sigma \approx 0.1665$ fm. This flow time is in the flat region of $R(t)$, however, with NRQCD and thermodynamics applications in mind, we are interested in even coarser lattices. Therefore for tuning the gauge anisotropy we prefer such flow-observable combinations that quickly reach plateau and are monotonic for the most part. From Fig. 5.1 one can observe that, in general, the clover (C) and improved clover (I) observables reach a maximum and then approach the plateau from above, while Wilson (W) and Symanzik (S) observables reach maximum, then minimum and then approach the plateau from below. We therefore avoid using W and S observables for tuning the gauge anisotropy. Another observation from the left panel of Fig. 5.1 is the ordering of the combinations of W, S, Z flows and C, I observables from the least to most variation (i.e. the peak height): SC, ZC, WC, SI, ZI, WI. Given that ordering, we will choose the clover observable (C) for tuning.

Our discussion in this part follows closely the tuning process described in [Borsanyi et al., 2018]. The continuum limit is usually taken at fixed renormalized anisotropy. In the parameter space (β, ξ_0) the fixed renormalized anisotropy $\xi(\beta, \xi_0) = \text{const}$ translates into an implicit dependence $\xi_0(\beta)$ which we call the line of constant renormalized anisotropy (LCRA). We now exemplify the tuning process for the $\xi = 2$ LCRA. We generate ensembles on the grid that spans $\beta = \{6.9, ..., 7.3\}$ with step of 0.1 and $\xi_0 = \{1.78, ..., 1.94\}$ with step of 0.02, *i.e.*, $5 \times 9 = 45$ pure gauge tuning ensembles with the same lattice volume $16^3 \times 32$ (a large enough physical volume to accommodate

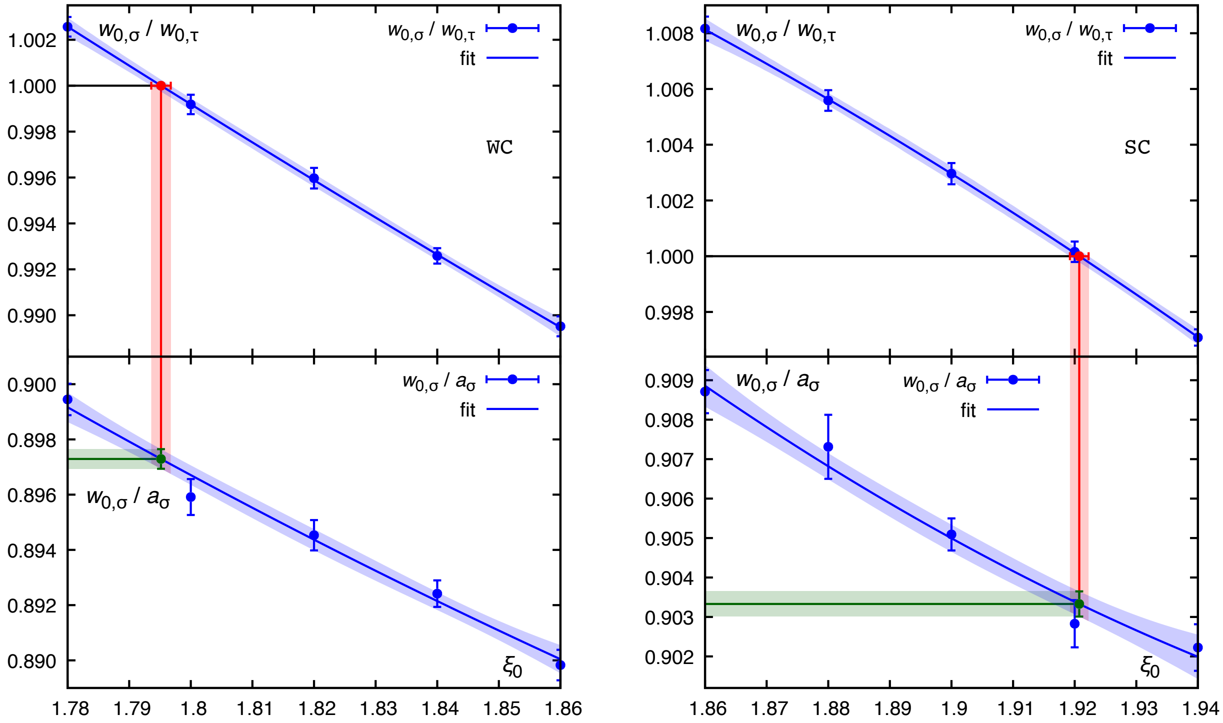

Figure 5.2 Determining the bare gauge anisotropy ξ_0 and the lattice scale in units of $w_{0,\sigma}/a_\sigma$ for a pure gauge ensemble at $\beta = 6.9$ and the renormalized anisotropy $\xi = 2$ in the WC (left) and SC (right) flow-observable scheme.

the lowest glueball and to allow for reaching the flow times on the scale of w_0^2 without distortions from the boundary). The large number of ξ_0 points is needed for studying different flow-observable combinations, as will become clear in a moment. Consider now fixed $\beta = 6.9$ set of ensembles as an example. At each ξ_0 we compute W, S and Z flows with the flow anisotropy set to the target one, $\xi_0^{gf} = \xi = 2$. For the WC combination the ratio $w_{0,\sigma}/w_{0,\tau}$ as function of the bare gauge anisotropy ξ_0 is shown in the top panel of the left panel of Fig. 5.2. We fit the dependence over the five nearby ξ_0 points with a linear or quadratic polynomial and propagate errors with bootstrap. The errors are uncorrelated – each point represents an independent ensemble. Determining ξ_0^* such that $w_{0,\sigma}(\xi_0^*)/w_{0,\tau}(\xi_0^*) = 1$ gives the bare gauge anisotropy for which at $\beta = 6.9$ the renormalized gauge anisotropy defined in the WC scheme is $\xi = 2$. In this particular case, $\xi_0^* = 1.7952(16)$. We similarly fit $w_{0,\sigma}(\xi_0)/a_\sigma$, shown in the bottom panel of the left panel of Fig. 5.2, and evaluate $w_{0,\sigma}(\xi_0^*)/a_\sigma = 0.89729(36)$. Thus, from this set of the tuning runs we learn that an ensemble

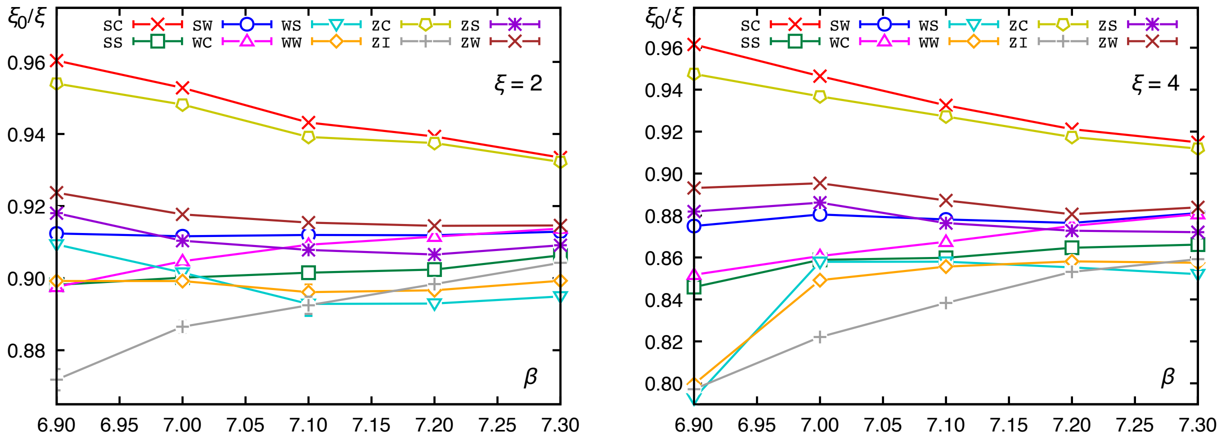

Figure 5.3 The lines of constant renormalized anisotropy, *i.e.*, functional dependencies $\xi_0(\beta)$ that correspond to the renormalized gauge anisotropy $\xi = 2$ (left) and $\xi = 4$ (right) in different flow-observable schemes.

generated at $(\beta = 6.9, \xi_0 = 1.7952)$ will have the target renormalized anisotropy $\xi = 2$ and the gradient flow scale $w_{0,\sigma}/a_\sigma$ of about 0.897.

The right panel of Fig. 5.2 illustrates the same process for $\beta = 6.9$ and the SC scheme. In that case, $\xi_0^* = 1.9207(15)$ and $w_{0,\sigma}(\xi_0^*)/a_\sigma = 0.90333(32)$. As expected, the discretization effects lead to quite different values of ξ_0 for the two gradient flow schemes. For the production ensembles we will use only one scheme, for which we simply repeat the process described above for the sets of ensembles at different β values. This produces $\xi = 2$ LCRA encoded in the dependencies $\xi_0^*(\beta)$ and $w_{0,\sigma}(\xi_0^*, \beta)/a_\sigma$. To simplify the notation, we drop the asterisk $*$ and the ξ_0^* dependence in the scale, implying that $\xi_0(\beta)$ and $w_{0,\sigma}(\beta)/a_\sigma$ represent LCRA that maps $(\beta, \xi_0(\beta))$ to the target $(a_\sigma = w_0/(w_{0,\sigma}(\beta)/a_\sigma), \xi)$.

To understand the discretization effects further, we measured multiple flow-observable combinations for $\xi = 2$, and also repeated the same tuning process for $\xi = 4$ LCRAs in multiple gradient flow schemes. In the latter case, the tuning ensembles spanned the same β values, and the bare gauge anisotropies are $\xi_0 = \{3.0, ..., 3.9\}$ with step of 0.1. The lattice volume is $16^3 \times 64$.

The resulting $\xi = 2$ and $\xi = 4$ LCRAs in different gradient flow schemes are shown in the left and right panels of Fig. 5.3, respectively. The lines are drawn to simply guide the eye and are not fits. The errorbars are not visible on the scale of the figure. For easier comparison, the y-axes are

$\xi_0(\beta)/\xi$ rather than $\xi_0(\beta)$. In the limit $\beta \to \infty$ the ratio of the bare to renormalized anisotropy must approach $\xi_0/\xi \to 1$. The largest ratio is provided by the SC scheme and it may be preferred as the least amount of renormalization is needed. However, the SC LCRA $\xi_0(\beta)$, and similarly the nearby ZC LCRA, is decreasing in the relevant β range, which means that at some value of β it must acquire a minimum and then approach 1 from below. This non-monotonicity of the SC LCRA most likely translates into the non-monotonicity in the approach to the continuum limit in the observables, if the simulations are tuned in the SC scheme. We, in general, would like to avoid such behavior. The more promising schemes are WC and ZI, and, perhaps, SS and SW. The WS, ZS, ZW exhibit a decrease similar to SC and ZC. WS and WW appear relatively flat for $\xi = 2$ but exhibit a rapid drop at the lowest coupling $\beta = 6.9$ for $\xi = 4$ (Fig. 5.3, right). We attribute that behavior to the early-flow-time artifacts, similar to the ones shown in Fig. 5.1, since for $\xi = 2$ LCRA $\beta = 6.9$ corresponds to $a_\sigma \approx 0.20$ fm, while for $\xi = 4$ LCRA to $a_\sigma \approx 0.24$ fm. The two schemes that exhibit monotonically rising behavior are WC and ZI. The ZI LCRA is significantly below the WC LCRA, meaning that ξ_0 requires larger renormalization. We therefore use WC as the tuning scheme for all production ensembles. With the WC tuning scheme and the choice of the gauge action in Eq. (4.1) our pure gauge setup is identical to the one of [Borsanyi et al., 2018], which used the renormalized anisotropy $\xi = 2$.

For parametrization purposes it is more convenient to work with the inverse gradient flow scale. The $\xi = 2$ and $\xi = 4$ LCRAs that we tuned in the range of bare gauge couplings $\beta = 6.9, ..., 7.3$ are shown, respectively, in the left and right panels of Fig. 5.4. The top panels display $a_\sigma/w_{0,\sigma}(\beta)$ and the bottom $\xi_0(\beta)$. The dashed lines in the left panel show the corresponding parametrizations of the $\xi = 2$ LCRA from [Borsanyi et al., 2018]. The deviations for $\beta < 7$ can be attributed to the fact that the lowest coupling considered there was $\beta = 7$ ($\beta = 4.2$ in their standard normalization $\beta = 2N_c/g_0^2$) and thus the fits were not constrained below that point.

The inverse gradient flow scale is fit with the Allton-type ansatz [Allton, 1997]:

$$\frac{a_\sigma}{w_0}(\beta) = c_0 f(\beta) \frac{1 + c_2(10/\beta) f(\beta)^2}{1 + d_2(10/\beta) f(\beta)^2}, \tag{5.2}$$

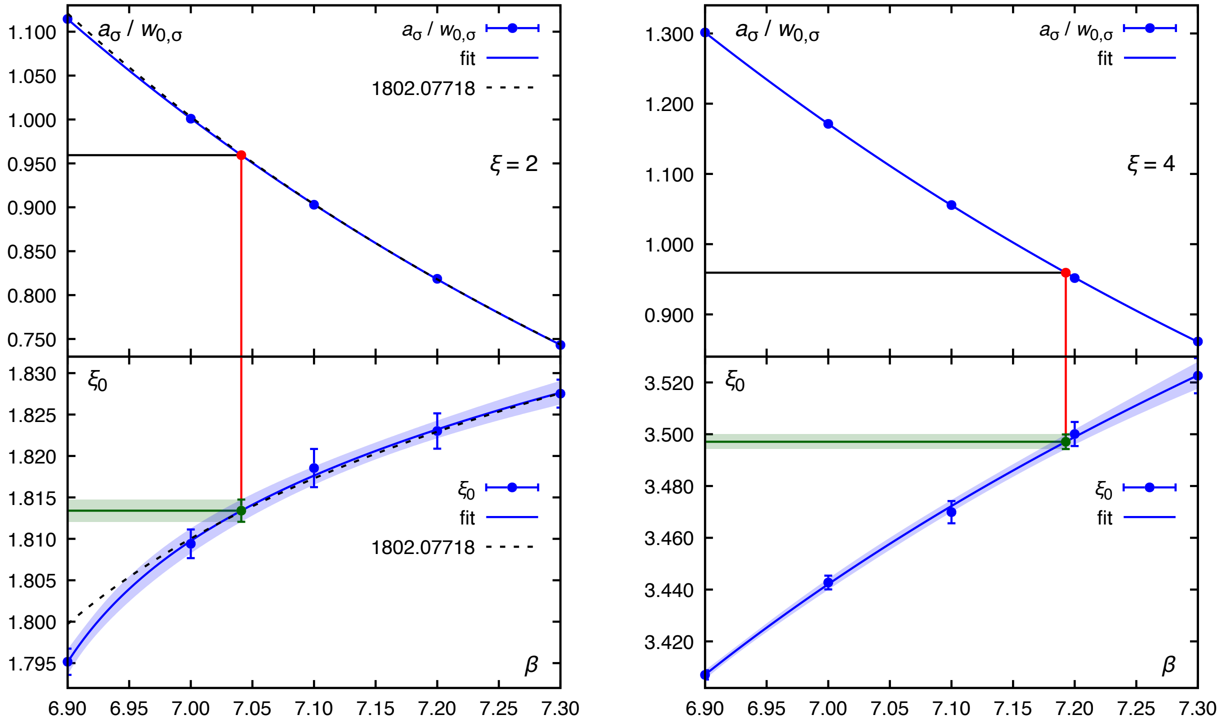

Figure 5.4 Finding the bare gauge coupling β (top panels) and the bare gauge anisotropy ξ_0 (bottom panels) that correspond to the spatial lattice spacing $a_\sigma = 0.1665$ fm and the renormalized anisotropy $\xi = 2$ (left panels) and 4 (right panels), in the WC scheme, as explained in the text. The curves in the bottom panels are the same as the magenta lines with the triangle symbols in Fig. 5.3, shown as ξ_0 on the y-axis.

$$f(\beta) = \left(\frac{10b_0}{\beta}\right)^{-b_1/(2b_0^2)} \exp\left(-\frac{\beta}{20b_0}\right), \tag{5.3}$$

where the two-loop beta-function coefficients for the $N_c = 3$ pure gauge case are $b_0 = 11N_c/(48\pi^2)$ and $b_1 = 34N_c^2/(768\pi^4)$. For the $\xi = 2$ coefficients we find:

$$c_0 = 42.08(45), \quad c_2 = 856(152), \quad d_2 = 2.8(85.9),$$

and for $\xi = 4$:

$$c_0 = 43.13(75), \quad c_2 = 2539(255), \quad d_2 = 792(108).$$

To fit $\xi_0(\beta)$ we use the same rational function ansatz as in [Borsanyi et al., 2018] (ξ is fixed to the target value and is not a fit parameter):

$$\xi_0(\beta) = \xi\left(1 + \frac{10}{\beta}\,\frac{u_2 + u_4(10/\beta)}{1 + v_2(10/\beta)}\right), \tag{5.4}$$

where for $\xi = 2$

$$u_2 = -0.05958(66), \;\; u_4 = 0.03989(64), \;\; v_2 = -0.6727(27),$$

and for $\xi = 4$

$$u_2 = -0.039(19), \;\; u_4 = 0.013(18), \;\; v_2 = -0.562(47).$$

Negative u_2 reflects the fact that the approach to ξ is from below. Converted to our convention, the corresponding coefficients of the fit form (5.4) for $\xi = 2$ from [Borsanyi et al., 2018] are: $u_2 = -0.0578007$, $u_4 = 0.0375841$ and $v_2 = 0.65674$.

For the study of the fermion anisotropy tuning and properties of the staggered spectrum we tuned ensembles with various gauge anisotropies and fixed spatial lattice spacing $a_\sigma^* \approx 0.1665$ fm in the WC scheme. The use of the LCRA for tuning is also illustrated in Fig. 5.4. That lattice spacing corresponds to $a_\sigma^*/w_0 = 0.1665/0.17355 \approx 0.959378$. (We use $w_0 = 0.17355(92)$ fm from the FLAG Review 2024 [Aoki et al., 2026].) Solving $a_\sigma/w_{0,\sigma}(\beta) = a_\sigma^*/w_0$ for β from the top curve and then computing ξ_0 at that β from the lower curve gives the needed parameters. For $\xi = 2$ we have $\beta = 7.0410(34)$ and $\xi_0 = 1.8134(13)$, and for $\xi = 4$ $\beta = 7.19278(39)$ and $\xi_0 = 3.4971(28)$.

In addition to $\xi = 2$ and $\xi = 4$ we also tuned a set of ensembles with the same spatial lattice spacing $a_\sigma \approx 0.1665$ fm and the renormalized anisotropies $\xi = 1$, 1.1, 1.2, 1.5 and 8. The parameters of the ensembles are summarized in Table A.1 in Appendix A. The mistuning of anisotropy can be measured by deviation of the $w_{0,\sigma}/w_{0,\tau}$ ratio from one. The largest in our case is 0.1% (for $\xi = 8$). The largest deviation of the spatial lattice spacing from the target value $a_\sigma = 0.1665$ fm is 0.4% (also for $\xi = 8$). We find, expectedly, that the gradient flow anisotropy tuning procedure is statistically quite accurate.

The gradient flow is integrated with the 6-stage 4-order low-storage Runge-Kutta scheme of [Berland et al., 2006] which happens to be a low-storage commutator-free Lie group integrator, as explained in [Bazavov, 2021],[Bazavov and Chuna, 2021], [Bazavov, 2026],[Bazavov, 2025]. The setup is identical to, *e.g.*, the one used in [Bazavov et al., 2026], apart from the anisotropy. While in [Bazavov et al., 2026] the integration was performed at step sizes as large as $1/20$, here one should take into account the potentially large anisotropy factors, Eq. (4.4), that appear in the generator of the flow. For that reason, for instance, at the largest anisotropy $\xi = 8$, we used the step size of $1/128$ to keep the integration stable.

5.3 Meson correlation functions fits

Our spectrum computational setup is very similar to the one used in [Bazavov et al., 2010b], [Bazavov et al., 2013]. For tuning spectrum measurements with zero and finite momentum we used corner wall sources. Examples of correlators at zero and finite momenta can be seen in Fig. 5.5. For pion splittings measurements we used the special wall sources that include phases and allow us to project different meson tastes at the sink, which are also standard in the MILC code. Part of the fitting process for one instance, π_{45} at $\xi = 2$ and $\xi = 4$, is shown in Figs. 5.6 and 5.7. The meson correlation functions are fit to the expected staggered form, i.e. Eq. (3.82), that includes oscillating channel and the back-propagating states due to the finite temporal extent of the lattice:

$$C(\tau) = \sum_{i=1}^{2} A_i^n \left(e^{-E_i^n \tau} + e^{-E_i^n (N_\tau - \tau)}\right) + (-1)^\tau \sum_{j=1}^{2} A_j^o \left(e^{-E_j^o \tau} + e^{-E_j^o (N_\tau - \tau)}\right), \tag{5.5}$$

where the superscripts “n" and “o" denote non-oscillating and oscillating states, respectively.

Where necessary, we include up to one excited state in each channel. The consistency of the fits is checked by comparing the results with and without the excited states and by varying the minimal distance included in the fit τ_{min}. All fits whose results are listed in Tables B.1–B.9, E.2 and E.3 were performed independently by two authors with different software: `lsqfit` [Lepage and Gohlke, 2025] and the software similar to the one used in [Bazavov et al., 2010b]. The final values quoted in the tables are produced by the following procedure:

1. If necessary (for complicated cases such as heavier pion tastes), perform uncorrelated fits to find reasonable starting guesses for the fit parameters.

2. Perform correlated fits on the full ensemble to find where the ground state energy reaches a plateau and χ^2/dof is about 1.

3. Choose and keep constant τ_{min} consistent with point 2, and keep $\tau_{max} = N_\tau/2 - 1$.

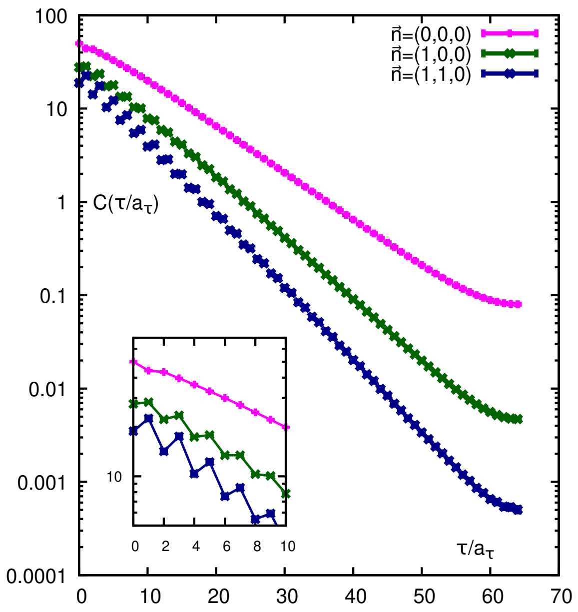

Figure 5.5 Correlators for $\eta_{s\bar{s}}$ at zero and finite momentum: $(N_\sigma a_\sigma \vec{p}/2\pi)^2 = \vec{n}^2 = 0, 1, 2$. $\eta_{s\bar{s}}$ has Goldstone spin-taste structure, and at zero momentum there should be no state in the opposite parity channel, as discussed at the end of Sec. 3.2.2. One can however see the emergence of the parity partner as the momentum increases from zero.

4. Perform correlated fits (with the covariance matrix from the full ensemble) with fixed τ_{min}, τ_{max} in each jackknife bin.

5. Propagate errors on the ground state energies (and the functions thereof such as pion splittings) with the jackknife procedure.

Thus, the final quoted errors are propagated with jackknife and they are typically large enough to accommodate the systematic errors coming from varying τ_{min}.

5.4 Fermion anisotropy and strange quark mass tuning

In our setup, the main parameter controlling the fermionic part of the action is the bare strange quark mass $a_\sigma m_s$. Its value is tuned such that the mass of the fictitious $\eta_{s\bar{s}}$ meson is approximately equal to $M_{s\bar{s}}^{phys} = 685.8$ MeV, as computed by fitting lattice data to chiral perturbation theory in [Davies et al., 2010]. Similarly to the bare gauge anisotropy tuning, the ultimate goal is to determine the mapping $(a_\sigma m_s, \xi_0^f) \longrightarrow (M_{s\bar{s}}, \xi^f)$, where ξ^f is the renormalized fermion anisotropy, that can be inverted and would allow one to predict what bare parameters $a_\sigma m_s$, ξ_0^f are needed to produce an ensemble with desired properties. The fermion anisotropy may depend on the quark mass. To simplify tuning and define the action to have only one bare fermion anisotropy parameter independently of what quarks are included, we define the fermion anisotropy of an ensemble as

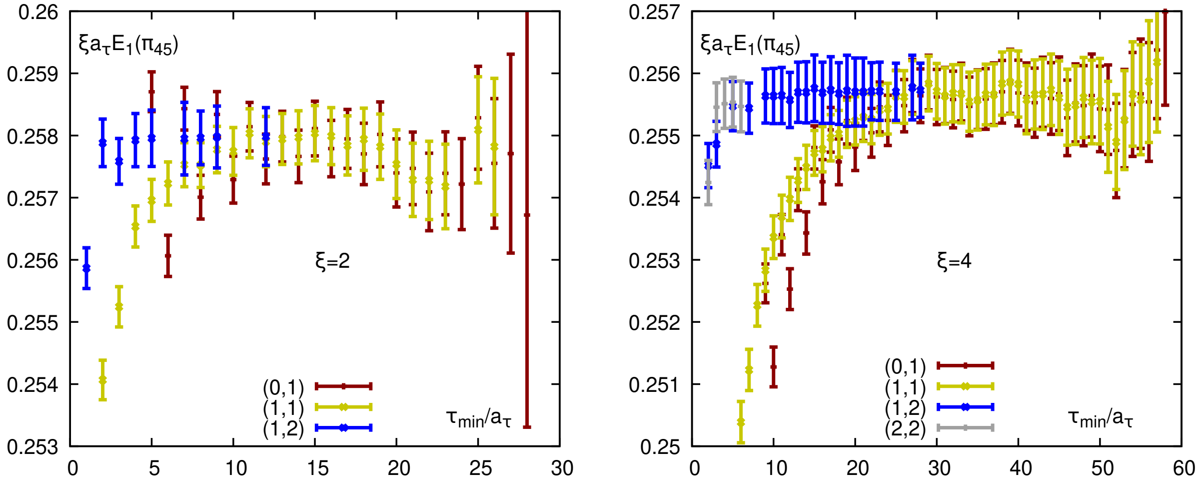

Figure 5.6 Ground state channel energies for π_{45} at fixed τ_{max} and varying τ_{min}, for $\xi = 2, 4$. In the notation of Eq. (5.5) we are plotting E_1^o. The corresponding χ^2/dof are plotted in Fig. 5.7. The notation (N, M) indicates N states in the non-oscillating, and M states in the oscillating channel. Generally, one tries to include as many states as possible to the fit, and looks for plateaus in plots like the ones presented here, taking the χ^2/dof values into account. One can see how the energy plateaus earlier for the fits with more states included. One can also see that it is easier to identify plateaus in the higher ξ case (right panel), where even a (2,2) fit was possible for early τ_{min} values.

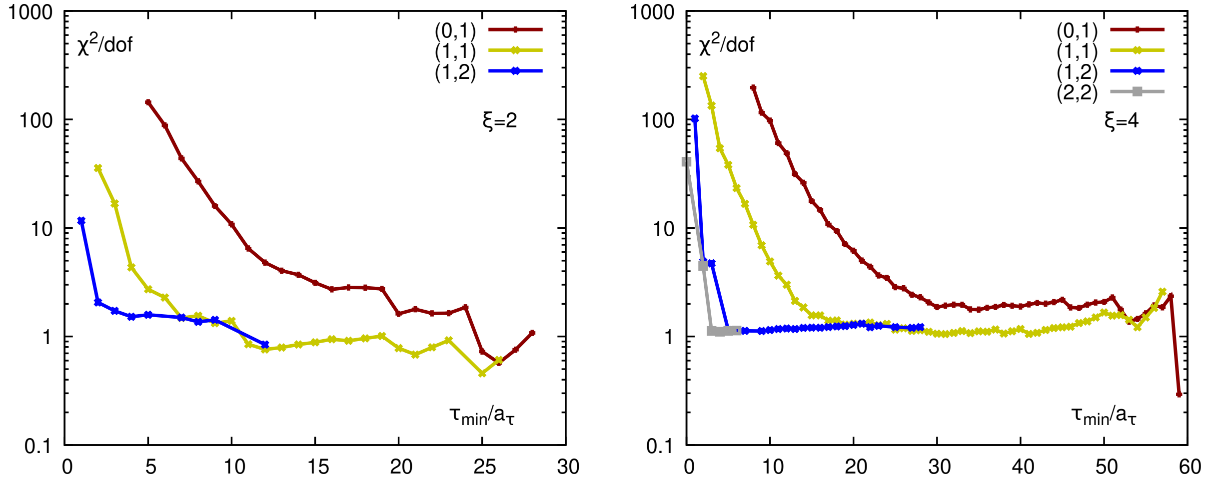

Figure 5.7 χ^2/dof is plotted against τ_{min}, for the π_{45} fits presented in Fig. 5.6. Once can notice how noise from excited states excluded from the fits decreases, as τ_{min} increases. This happens earlier for fits with more states included. For example, by looking at the $(0, 1)$ points, we can infer that the non-oscillating ground state is not present for $\tau_{min} \gtrsim 30$, since these points approach 1 around this τ_{min} and therefore only the oscillating ground state contributes.

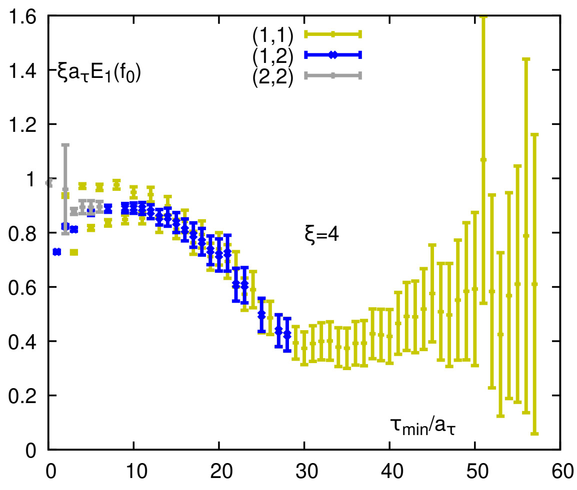

Figure 5.8 Energy plotted against τ_{min} for the ground state channel of the parity partner of π_{45}, which is the scalar meson f_0, at $\xi = 4$. In the language of Eq. (5.5) we are plotting E_1^n. One can see from the right panel of Fig. 5.7, and specifically from the $(0, 1)$ points, that after $\tau_{min} \sim 30$ the f_0 channel is no longer present. Therefore, if we were to extract the f_0 mass from this fit, we should probably trust the first plateau, i.e. the $\tau_{min} \sim 5$ fits of $(2, 2)$ or the $\tau_{min} \sim 10$ fits of $(1, 2)$.

the one evaluated at the strange quark mass that corresponds to the $\eta_{s\bar{s}}$ at the physical mass. This choice is dictated by convenience, as it should not matter and different choices, e.g., $a_\sigma m_s/2$ or $a_\sigma m_s/27$ being the reference point, should give the same continuum limit. (And, as shown below, the dependence of the bare fermion anisotropy ξ_0^f on the quark mass for aHISQ is flat across a large mass range.

To determine the renormalized fermion anisotropy we use the dispersion relation method. We performed tuning for both naive and highly improved staggered quarks to investigate the effect of smearing on the staggered spectrum and to also validate our code and tuning procedure by comparing with the naive staggered simulations in [Nomura et al., 2004] and [Levkova et al., 2006].

We discuss the parameter tuning of the naive staggered quark action first. At this stage we consider (β, ξ_0) fixed and for brevity suppress the parameters that are fixed in the following. For illustration, we use $(\beta = 6.87348, \xi_0 = 1.15792)$ ensemble listed in Table A.1 that has the renormalized anisotropy $\xi = 1.2$.

In the first step of our fermion anisotropy tuning process we keep the bare strange quark mass $a_\sigma m_s$ fixed. We measure the Goldstone pseudoscalar meson correlation functions for the $\eta_{s\bar{s}}$ meson at the three lowest spatial momenta $a_\sigma \vec{p} = 2\pi\vec{n}/N_\sigma$ for several bare fermion anisotropies ξ_0^f. In more convenient integer units they are $\vec{n} = (0, 0, 0)$, $\vec{n} = (1, 0, 0)$ and $\vec{n} = (1, 1, 0)$, and correspond to $(N_\sigma a_\sigma \vec{p}/2\pi)^2 = \vec{n}^2 = 0, 1, 2.$[1] The energy squared plotted in similarly rescaled

---

[1] See Fig. 5.5.

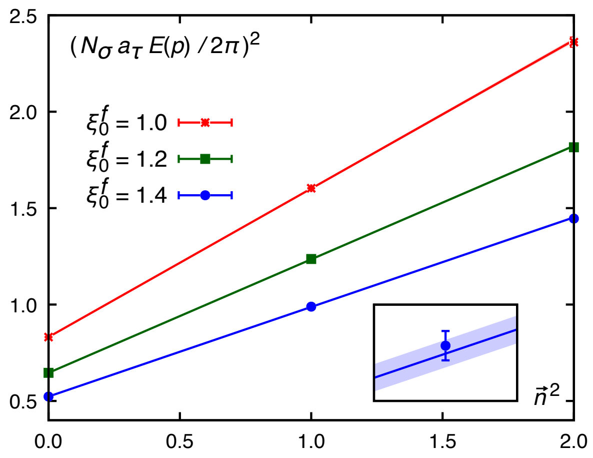

Figure 5.9 Fits to the dispersion relation for naive staggered fermions on the ensemble ($\beta = 6.87348, \xi_0 = 1.15792$) that has the renormalized anisotropy $\xi = 1.2$. The bare quark mass is $a_\sigma m_s = 0.02$ and the bare fermion anisotropy is varied $\xi_0^f = 1$, 1.2 and 1.4. The slopes of the fits produce, respectively, $\xi^f = 1.13958(436)$, $\xi^f = 1.30358(351)$ and $\xi^f = 1.46703(384)$.

units as $(N_\sigma a_\tau E(p)/2\pi)^2$ vs $\vec{n}^2$ for the $\xi = 1.2$ ensemble at $a_\sigma m_s = 0.02$ is shown in Fig. 5.9 for three bare fermion anisotropies $\xi_0^f = 1$, 1.2 and 1.4. By fitting the dispersion relation (4.11) with a linear polynomial, we determine the renormalized anisotropy ξ^f for a given bare ξ_0^f. In the units of Fig. 5.9 the slope is simply $1/(\xi^f)^2$. The errors are propagated with the jackknife procedure. The errorbars are not visible on the scale of the figure and the lines, in fact, have error bands. This is illustrated in the inset of Fig. 5.9 by magnifying the vicinity of the $\vec{n}^2 = 1$ point for $\xi_0^f = 1.4$.

Once the renormalized fermion anisotropy ξ^f and the $\eta_{s\bar{s}}$ mass are determined for each bare fermion anisotropy ξ_0^f, we can fit them as functions of ξ_0^f. We use a quadratic polynomial, however, given that there are only three bare anisotropies, this is simply an interpolation. The data together with the fits are shown in the left panel of Fig. 5.10. By solving $\xi^f(\xi_0^f) = \xi = 1.2$ for ξ_0^f (upper panel) we determine the bare fermion anisotropy $\xi_0^{f*} = 1.074(46)$ that corresponds to the renormalized anisotropy $\xi^f = 1.2$. Evaluating $a_\tau M_{s\bar{s}}(\xi_0^{f*})$ gives the $\eta_{s\bar{s}}$ mass, $a_\tau M_{s\bar{s}} = 0.34117(43)$ that also corresponds to $\xi = 1.2$. Now the bare fermion anisotropy is properly tuned and the renormalized anisotropy is the same for both, gauge and fermion parts of the action. However, the mass of the $\eta_{s\bar{s}}$ meson is at some arbitrary value, since we held $a_\sigma m_s = 0.02$ fixed until now. Thus, at the next tuning stage, the process described above is repeated for several values of the bare strange quark mass, in this case $a_\sigma m_s = 0.04$ and 0.06. As a result, we get the dependence $\xi_0^f(a_\sigma m_s)$ for fixed $\xi^f = 1.2$ (i.e., what bare anisotropy is needed to produce the renormalized fermion anisotropy at a given $a_\sigma m_s$) and the dependence $a_\tau M_{s\bar{s}}(a_\sigma m_s)$, also for fixed $\xi_f = 1.2$. These two functions (with

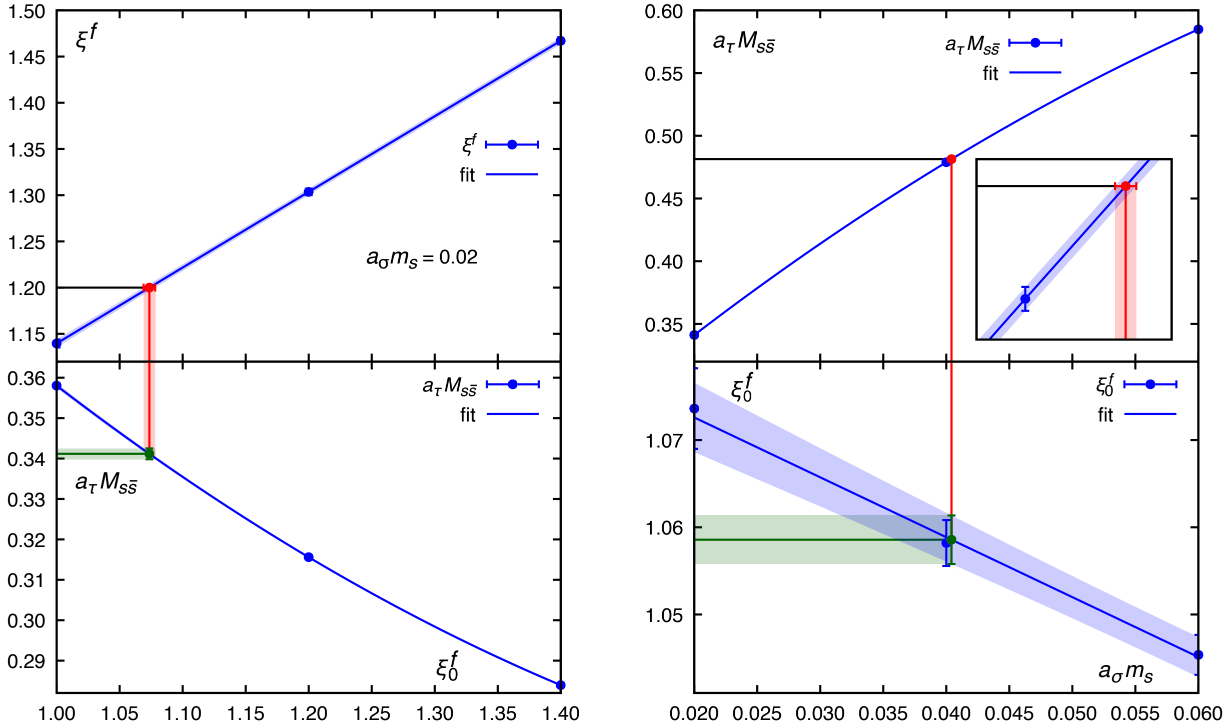

Figure 5.10 (Left panel) Finding the bare fermion anisotropy ξ_0^f that corresponds to the renormalized fermion anisotropy $\xi_f = \xi = 1.2$ (top) and then computing the $\eta_{s\bar{s}}$ at that ξ_0^f (bottom) for naive staggered fermions at the strange quark mass $a_\sigma m_s = 0.02$. (Right panel) Finding the bare strange quark mass at which the $\eta_{s\bar{s}}$ is at the physical value, $a_\sigma m_s = 0.040412(44)$ (top) and computing the bare fermion anisotropy at that mass, $\xi_0^f = 1.0586(28)$.

the data and the fits) are shown in the right panel of Fig. 5.10. The $a_\tau M_{s\bar{s}}(a_\sigma m_s)$ (top panel of the right panel of Fig. 5.10) function has some curvature and is fit (in fact, interpolated since there are only three points) with a quadratic polynomial. The $\xi_0^f(a_\sigma m_s)$ dependence is consistent with a linear fit. For the final tuning step we compute the mass of the fictitious $\eta_{s\bar{s}}$ meson in units of the temporal lattice spacing: $a_\tau M_{s\bar{s}} = a_\sigma/\xi \cdot M_{s\bar{s}}^{phys} = 0.166218 \text{ fm}/1.2 \cdot 685.8 \text{ MeV}/197.327 \text{ MeV} \cdot \text{fm} \approx 0.4814$. Solving $a_\tau M_{s\bar{s}}(a_\sigma m_s^*) = 0.4814$ for $a_\sigma m_s^*$ (top panel) and then evaluating $\xi_0^f(a_\sigma m_s^*)$ (bottom panel) gives the final parameters: for naive staggered fermions on the quenched ensemble ($\beta = 6.87348, \xi_0 = 1.15792$) the pair ($a_\sigma m_s = 0.040412(44), \xi_0^f = 1.0586(28)$) is on the $\xi = 1.2$ LCRA with the mass of the $\eta_{s\bar{s}}$ at the physical value.

Using the procedure described above, we tuned three anisotropic naive staggered ensembles with the renormalized anisotropy $\xi = 1.2$, 1.5 and 2 at fixed spatial lattice spacing $a_\sigma \approx 0.1665$ fm.

One should note that, despite the fact that we only need to compute strange quark propagators, the tuning process is quite computationally demanding. In this case, very similar to tuning of the gauge anisotropy, we needed to generate a grid in the parameter space that spanned:

- $\xi = 1.2$: $a_\sigma m_s = \{0.02, 0.04, 0.06\} \times \xi_0^f = \{1, 1.2, 1.4\}$,
- $\xi = 1.5$: $a_\sigma m_s = \{0.03, 0.05, 0.07, 0.09\} \times \xi_0^f = \{1.05, 1.25, 1.45, 1.65\}$,
- $\xi = 2$: $a_\sigma m_s = \{0.025, 0.035, 0.045\} \times \xi_0^f = \{1.2, 1.6, 2\}$.

For each point on the $(a_\sigma m_s, \xi_0^f)$ grid we need to compute correlation functions at three momenta.

We followed the same tuning protocol for the aHISQ action at two anisotropies $\xi = 1.2$ and $\xi = 1.5$. The final stages of the tuning process are shown in the left and right panels of Fig. 5.11, respectively. In that case the parameter grid spanned:

- $\xi = 1.2$: $a_\sigma m_s = \{0.05, 0.07, 0.09\} \times \xi_0^f = \{1, 1.2, 1.4\}$,
- $\xi = 1.5$: $a_\sigma m_s = \{0.05, 0.07, 0.09\} \times \xi_0^f = \{1.05, 1.25, 1.45, 1.65\}$.

While the functional dependence $a_\tau M_{s\bar{s}}(a_\sigma m_s)$ is similar between the naive staggered and aHISQ actions, the striking feature of aHISQ is almost no dependence of the bare fermion anisotropy on the quark mass $\xi_0^f(a_\sigma m_s)$: in the range where the $\eta_{s\bar{s}}$ mass changes by about 25%, the variation in the bare fermion anisotropy is about 0.7% and can be fit with a constant, Fig. 5.11. Moreover, the value of the tuned bare fermion anisotropy for aHISQ is within 0.6% (1.7σ) for $\xi = 1.2$ and 0.3% (0.8σ) for $\xi = 1.5$ of the target renormalized anisotropy. (For $\xi = 1.5$ we also have measurements at $a_\sigma m_s = 0.03$, as indicated in Table B.3. We do not include them in the tuning process, shown in Fig. 5.11, as we are interested in the strange quark mass not too far from the physical value. However, even if that point is included in the right panel of Fig. 5.11, the fit for ξ_0^f (lower panel) is still consistent with a constant.)

The flatness of the $\xi_0^f(a_\sigma m_s)$ dependence means that tuning of aHISQ can be drastically simplified. If the trend $\xi_0^f \approx \xi$ persists to larger anisotropies, one can simply set $\xi_0^f = \xi$ (target renormalized anisotropy) in the fermion part of the action and only tune the strange quark mass.

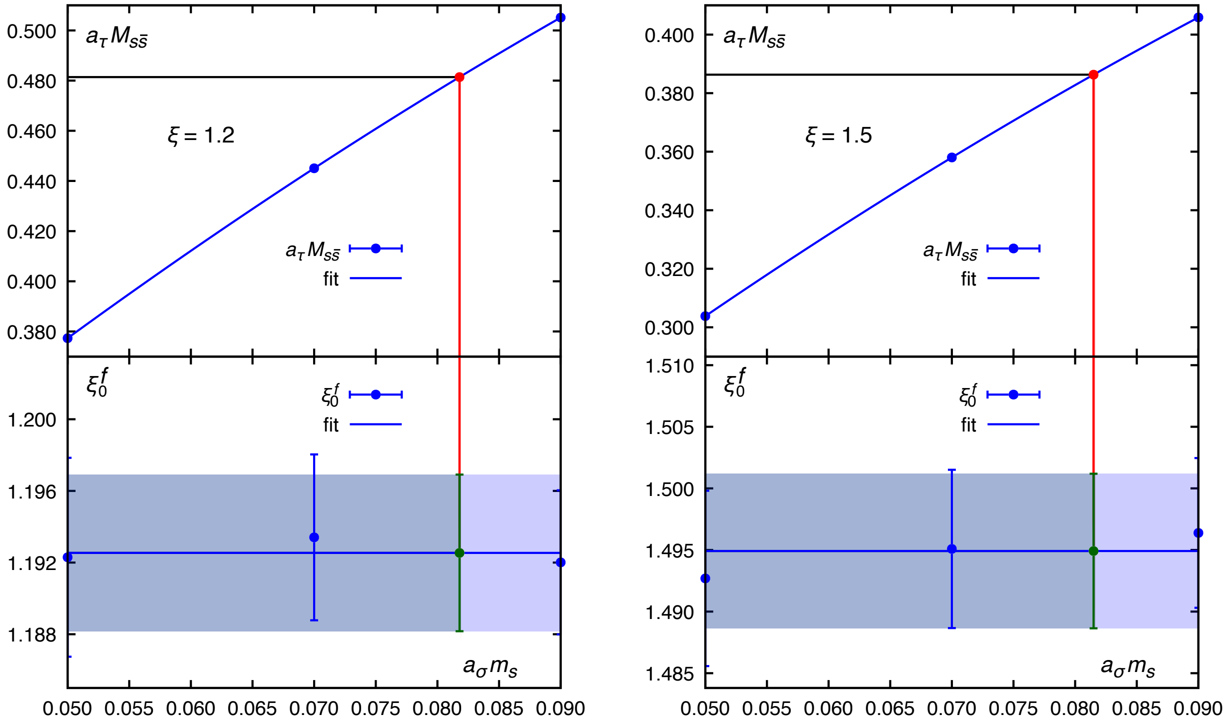

Figure 5.11 Final tuning steps that determine the strange quark mass that corresponds to the $\eta_{s\bar{s}}$ at the physical point (upper panels) and the corresponding bare fermion anisotropy (lower panels) for the aHISQ action on the ensembles with the renormalized anisotropy $\xi = 1.2$ and $\xi = 1.5$. These are the same tuning steps as shown in the right panel of Fig. 5.10 for the naive staggered action.

To check that, however, we adopted a simplified tuning procedure for aHISQ that still allows us to tune both the bare fermion anisotropy and strange quark mass. Namely, instead of measuring the dispersion relation on the full grid of masses and bare anisotropies, we first fix the strange quark mass close to the anticipated target value, and vary the bare fermion anisotropy only at that mass. From the fit we find proper tuned value of ξ_0^f (that gives $\xi^f = \xi$), and then vary the strange quark mass only at that bare anisotropy. In other words, for aHISQ one can reduce two-dimensional grid search to two one-dimensional searches, where only one of them requires non-zero momentum measurements.

With the simplified procedure described above we tuned aHISQ action at the additional renormalized anisotropies $\xi = 1.1$, 2, 4 and 8. The values of the ground state energies for aHISQ used in the tuning process are documented in Tables B.1–B.7 and the predicted $a_\sigma m_s$ and ξ_0^f for various ensembles in Table B.8. It has to be noted that in those tables we documented the values in units of

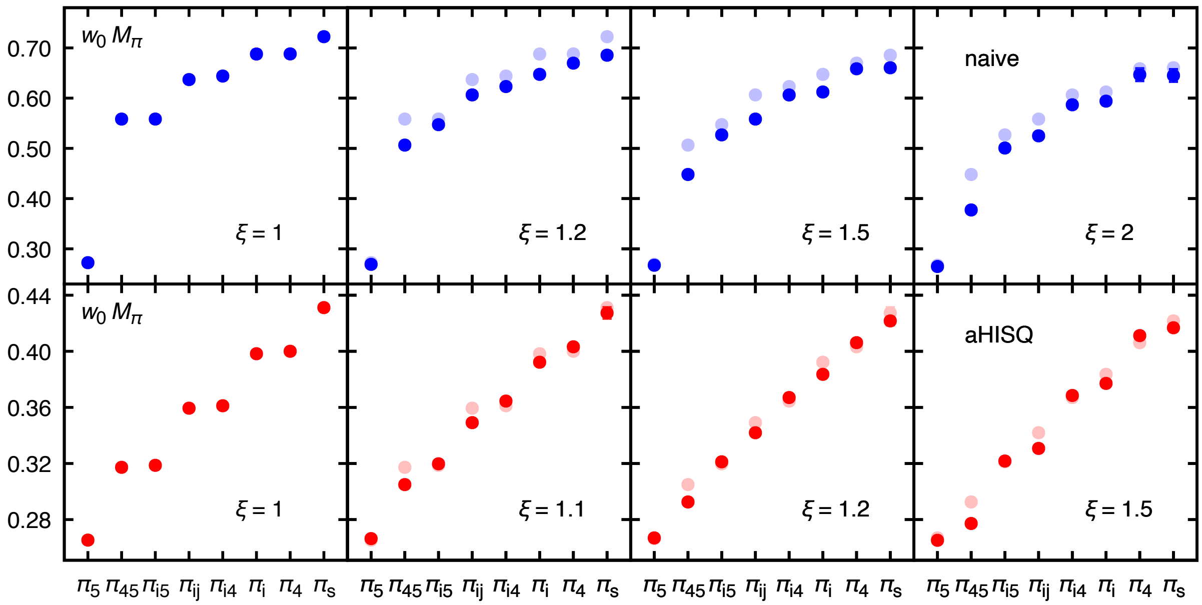

Figure 5.12 Progression of pion taste masses, plotted as dimensionless combinations $w_0 M_\pi$, from isotropic $\xi = 1$ case to anisotropy up to 2 for naive (upper panel) and 1.5 for aHISQ (lower panel) action. The Goldstone pion π_5 is tuned to approximately same value for all anisotropies. Pale points represent the values of the masses at the anisotropy on the plot immediately to the left.

the temporal lattice spacing, $a_\tau E$, directly as they are determined from the fits. For the discussion in the next section however, in order to be able to compare different anisotropies, we need to convert everything to common units. A convenient choice is w_0 units: $w_0 E = (w_0/a_\sigma)\xi(a_\tau E)$. In other words, the $a_\tau E$ values from the tables are multiplied by the gradient flow scale w_0/a_σ, listed in the seventh column of Table A.1, and by the renormalized anisotropy ξ, listed in the third column of the same table.

5.5 Pion taste masses and splittings

Our main focus is to understand how to tune the aHISQ action for future dynamical simulations. We also need to study the pattern of the pion taste multiplets, as taste-breaking effects are often the dominant discretization effects with staggered actions. In this initial phase, we study the dependence of the pion taste masses on the anisotropy at fixed spatial lattice spacing. The bare light quark mass is set to $a_\sigma m_l = a_\sigma m_s/5$. For lower anisotropies, we also measured the pion taste masses with the naive staggered action. Those allow us to check correctness of our workflow (from ensemble generation to the final fits), and also compare two different actions, where we, in fact, observe some qualitative differences. To illustrate the effect, we plot the pion taste masses at different anisotropies in Fig. 5.12. The top panel displays the values for the naive action and the bottom for the aHISQ action. The pion mass is in units of $1/w_0$. The anisotropy increases from left to right, and since the dependence on anisotropy at low values is much steeper for aHISQ, we illustrate the change for the naive staggered action on $\xi = 1$, 1.2, 1.5 and 2, and for aHISQ on $\xi = 1$, 1.1, 1.2 and 1.5 ensembles. At the anisotropies $\xi > 1$ the pale points represent the values at the previous anisotropy. From the progressions in Fig. 5.12 one can observe the following: for the naive staggered action all heavier pion tastes move down, as the anisotropy increases, approaching the new degeneracy pattern expected for $\xi \gg 1$, as discussed in Sec. 4.5. For aHISQ, the $\xi_4\xi_5$, $\xi_i\xi_j$, ξ_i and 1 tastes move down, while the $\xi_i\xi_5$, $\xi_i\xi_4$ and ξ_4 move up at much slower rate, compared to the first four. (On the scale of the figure the $\xi_i\xi_5$ taste appears constant, but it also moves up, as will become apparent shortly.) For the ease of notation, we use two ways to denote pion tastes: with the explicit taste matrix-structure, *e.g.*, $\xi_i\xi_5$, and as π with a proper index, *e.g.*, π_{i5}. The taste structure 1 is denoted π_s.

Now we consider the quadratic splittings from the lowest, Goldstone pion mass:

$$\delta M_\pi \equiv M_\pi^2 - M_{\pi_5}^2, \tag{5.6}$$

where the index π denotes all taste structures except of ξ_5. For the ease of comparison between the naive staggered and aHISQ, we normalize by the splittings for the heaviest taste, π_s, at the anisotropy $\xi = 1$:

$$\Delta_\pi \equiv \frac{\delta M_\pi}{\delta M_{\pi_s}\big|_{\xi=1}}. \tag{5.7}$$

The normalized splittings Δ_π for the naive staggered and aHISQ action are shown in left and right panels of Fig. 5.13, respectively. The lines are not fits but simple spline interpolations to guide the eye. Apart from showing the obvious benefits of the smeared actions,–i.e., not only the naive taste masses are larger in magnitude, Fig. 5.12, the relative gap between the Goldstone and the next taste is twice larger for the naive staggered action compared to HISQ,–Fig. 5.13 highlights the qualitatively different behavior in the multiplet formation when anisotropy is increased. The

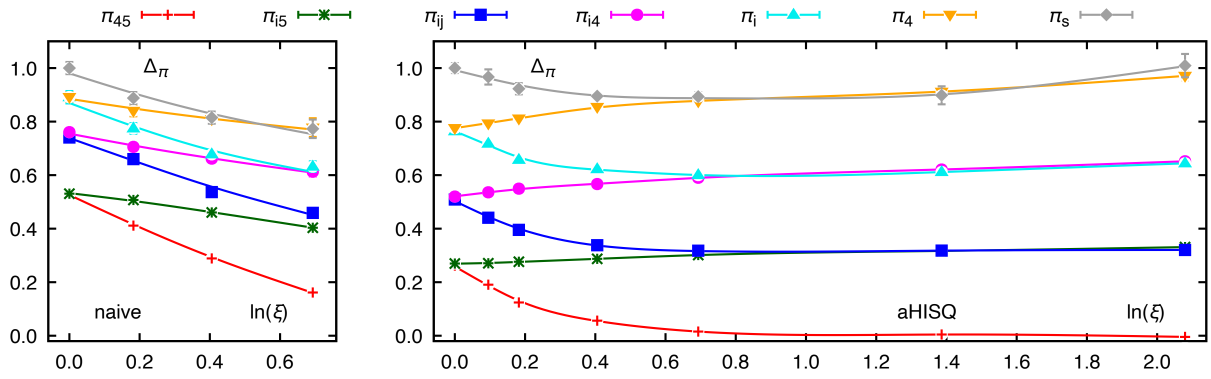

Figure 5.13 Splittings of pion taste multiplets from the Goldstone pion, normalized by the value for the singlet taste at $\xi = 1$, Eq. (5.7), for the naive staggered (left) and aHISQ (right) action, as function of $\ln(\xi)$.

naive taste splittings decrease, and this happens at a different but comparable rate to allow for the new pattern formation which is almost complete at the largest considered anisotropy $\xi = 2$ (except of the $\xi_4\xi_5$ not joining the ξ_5 taste yet). For aHISQ at low anisotropy, all odd pion taste splittings (using the ordering in the legend of Fig. 5.13) decrease at fast rate, while all the even ones increase, at a much slower rate. Moreover, the increase of the even splittings appears to become the dominant effect at higher anisotropy, and the odd splittings (except of the $\xi_4\xi_5$ that must become degenerate with ξ_5) must follow to maintain the new degeneracy pattern. For that reason, at some anisotropy between 2 and 4 the odd splittings acquire a minimum and start slowly increasing, following the even splittings. The effect is mild but resolvable within the errors.

Another way to look at the taste splittings is to normalize them by their individual corresponding value at the renormalized anisotropy $\xi = 1$:

$$\Delta'_\pi \equiv \frac{\delta M_\pi}{\delta M_\pi|_{\xi=1}}. \tag{5.8}$$

In that normalization, they are plotted in Fig. 5.14. The lines are not fits but spline interpolations to guide the eye. While for the naive staggered action there is no specific pattern, we observe that for aHISQ the even splittings that slightly increase ($\xi_i\xi_5$, $\xi_i\xi_4$ and ξ_4) collapse onto an almost universal curve. In other words, it may be that at the leading order their dependence on anisotropy is the same, and they only differ by multiplicative factors.

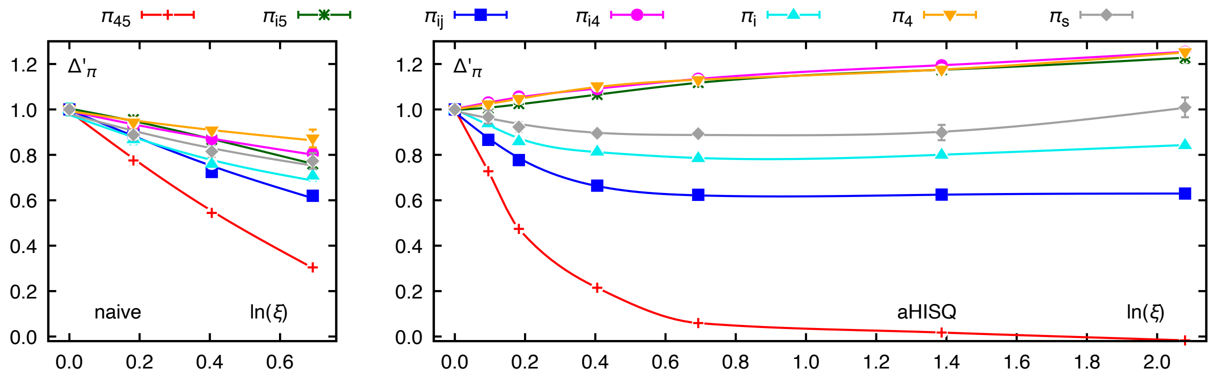

Figure 5.14 Splittings of pion taste multiplets from the Goldstone pion, normalized by their individual values at $\xi = 1$, Eq. (5.8), for the naive staggered (left) and aHISQ (right) action, as function of $\ln(\xi)$.

The observed patterns for the aHISQ pion taste splittings prompted our attempt to develop a qualitative model, described in the next section, that describes the splittings dependence on anisotropy.

5.6 Staggered chiral perturbation theory and a model for pion taste mass splittings

The dimension-6 operators contributing to the pion taste mass splittings have been identified in [Luo, 1998], [Lee and Sharpe, 1999]. For the isotropic case the chiral perturbation theory Lagrangian has the following form:

$$\mathcal{L}(\Sigma) = \frac{a^4 f^2}{8}\mathrm{Tr}\left(\partial_\mu \Sigma \partial_\mu \Sigma^\dagger\right) - \frac{a^4}{4} B f^2 \mathrm{Tr}\left(\mathcal{M}\Sigma + \mathcal{M}\Sigma^\dagger\right) + \frac{a^4 m_0^2}{24}(\mathrm{Tr}\Phi)^2 + \mathcal{V}, \tag{5.9}$$

where the field Σ is defined as $\Sigma = \exp(i\Phi/f)$, with f, B low energy constants and the term before the last term being relevant only for the taste- and flavor-singlet η' [Bernard, 2002]. The dimension-6 potential $\mathcal{V}$ contains the operators responsible for taste splittings, and we deliberately do not factor out a^6, as will become clear in a moment. It has two parts $\mathcal{V} = \mathcal{U} + \mathcal{U}'$, where $\mathcal{U}'$ affects only flavor-singlet states, as explained in [Aubin and Bernard, 2003], and we thus focus on the $\mathcal{U}$ in the following:

$$\begin{aligned}
-\mathcal{U} &= a^6 \sum_k C_k O_k \\
&= a^6 C_1 \mathrm{Tr}\big(\xi_5 \Sigma \xi_5 \Sigma^\dagger\big) \\
&+ a^6 C_3 \frac{1}{2} \sum_\nu \Big[\mathrm{Tr}\big(\xi_\nu \Sigma \xi_\nu \Sigma\big) + \mathrm{Tr}\big(\xi_\nu \Sigma^\dagger \xi_\nu \Sigma^\dagger\big)\Big] \\
&+ a^6 C_4 \frac{1}{2} \sum_\nu \Big[\mathrm{Tr}\big(\xi_{\nu 5} \Sigma \xi_{5\nu} \Sigma\big) + \mathrm{Tr}\big(\xi_{\nu 5} \Sigma^\dagger \xi_{5\nu} \Sigma^\dagger\big)\Big] \\
&+ a^6 C_6 \sum_{\mu<\nu} \mathrm{Tr}\big(\xi_{\mu\nu} \Sigma \xi_{\nu\mu} \Sigma^\dagger\big).
\end{aligned} \tag{5.10}$$

Anisotropy appears on the level of the fundamental theory and its effect on the level of the effective theory is not obvious. A proper procedure requires extending the Lee-Sharpe analysis [Lee and Sharpe, 1999] to anisotropic case. This is a possible direction for a future study. Here, we would like to find an empirical modification of the staggered chiral perturbation theory Lagrangian that can describe the anisotropy dependence observed in the data. The simplest way to transition to the anisotropic case is then to introduce appropriate factors of the temporal lattice spacing for the operators that contain temporal direction. Proceeding as in the isotropic case [Lee and Sharpe, 1999] by expanding the Σ field to second order, one arrives at the following pattern for the taste splittings:

$$\delta M_{45}(\xi) = \frac{16 a_\sigma^2}{f^2}\left(C_1 + 3C_3 + \frac{1}{\xi^2} C_4 + 3\frac{1}{\xi^2} C_6\right) \tag{5.11}$$

$$\delta M_{i5}(\xi) = \frac{16 a_\sigma^2}{f^2}\left(C_1 + \left(2 + \frac{1}{\xi^2}\right) C_3 + C_4 + \left(2 + \frac{1}{\xi^2}\right) C_6\right) \tag{5.12}$$

$$\delta M_{ij}(\xi) = \frac{16 a_\sigma^2}{f^2}\left(1 + \frac{1}{\xi^2}\right)(C_3 + C_4 + 2C_6) \tag{5.13}$$

$$\delta M_{i4}(\xi) = \frac{16 a_\sigma^2}{f^2} 2\left(C_3 + C_4 + \left(1 + \frac{1}{\xi^2}\right) C_6\right) \tag{5.14}$$

$$\delta M_{i}(\xi) = \frac{16 a_\sigma^2}{f^2}\left(C_1 + C_3 + \left(2 + \frac{1}{\xi^2}\right) C_4 + \left(2 + \frac{1}{\xi^2}\right) C_6\right) \tag{5.15}$$

$$\delta M_{4}(\xi) = \frac{16 a_\sigma^2}{f^2}\left(C_1 + \frac{1}{\xi^2} C_3 + 3C_4 + 3\frac{1}{\xi^2} C_6\right) \tag{5.16}$$

$$\delta M_{s}(\xi) = \frac{16 a_\sigma^2}{f^2}\left(\left(3 + \frac{1}{\xi^2}\right) C_3 + \left(3 + \frac{1}{\xi^2}\right) C_4\right) \tag{5.17}$$

It is known [Lee and Sharpe, 1999] that for smeared actions, such as HISQ, the splittings are dominated by the C_4 coefficient with the rest being close to zero. (We illustrate this with the actual data later.) We find, however, that the form in Eqs. (5.11)–(5.17) is inconsistent with the data. It predicts that for aHISQ the masses of the $\xi_i\xi_5$, $\xi_i\xi_4$ and ξ_4 tastes stay constant, while the $\xi_4\xi_5$, $\xi_i\xi_j$, ξ_i and 1 tastes approach the partner values as $1/\xi^2$, however, Fig. 5.14 clearly shows that $\xi_i\xi_5$, $\xi_i\xi_4$ and ξ_4 splittings increase with anisotropy. Moreover, for the naive staggered action the δM_{45} splitting would approach $C_1 + 3C_3$ rather than 0, when the $\xi_4\xi_5$ taste is expected to become degenerate with ξ_5. Thus, one needs to introduce anisotropy dependence in the low-energy constants. This alone, however, does not allow us to describe the data. We therefore introduce a further modification of the potential in Eq. (5.10). We assume that for anisotropic case the low-energy constants for the temporal components are different from the spatial ones. The potential then takes the following form:

$$
\begin{aligned}
-\mathcal{U}_{ani} \;=\;& a_\sigma^6 C_1(\xi)\mathrm{Tr}\big(\xi_5\Sigma\xi_5\Sigma^\dagger\big) \\
+\;& a_\sigma^6 C_3(\xi)\frac{1}{2}\sum_j\Big[\mathrm{Tr}\big(\xi_j\Sigma\xi_j\Sigma\big) + \mathrm{Tr}\big(\xi_j\Sigma^\dagger\xi_j\Sigma^\dagger\big)\Big] \\
+\;& a_\sigma^4 a_\tau^2 C_3'(\xi)\frac{1}{2}\Big[\mathrm{Tr}\big(\xi_4\Sigma\xi_4\Sigma\big) + \mathrm{Tr}\big(\xi_4\Sigma^\dagger\xi_4\Sigma^\dagger\big)\Big] \\
+\;& a_\sigma^6 C_4(\xi)\frac{1}{2}\sum_j\Big[\mathrm{Tr}\big(\xi_{j5}\Sigma\xi_{5j}\Sigma\big) + \mathrm{Tr}\big(\xi_{j5}\Sigma^\dagger\xi_{5j}\Sigma^\dagger\big)\Big] \\
+\;& a_\sigma^4 a_\tau^2 C_4'(\xi)\frac{1}{2}\Big[\mathrm{Tr}\big(\xi_{45}\Sigma\xi_{54}\Sigma\big) + \mathrm{Tr}\big(\xi_{45}\Sigma^\dagger\xi_{54}\Sigma^\dagger\big)\Big] \\
+\;& a_\sigma^6 C_6(\xi)\sum_{j<k}\mathrm{Tr}\big(\xi_{jk}\Sigma\xi_{kj}\Sigma^\dagger\big) \\
+\;& a_\sigma^4 a_\tau^2 C_6'(\xi)\sum_j\mathrm{Tr}\big(\xi_{j4}\Sigma\xi_{4j}\Sigma^\dagger\big).
\end{aligned}
\tag{5.18}
$$

Factoring out the spatial lattice spacing a_σ^6 produces explicit factors of anisotropy $1/\xi^2$ that always accompany the $C_i'(\xi)$ low-energy constants, so for convenience we replace them with $D_i(\xi) \equiv C_i'(\xi)/\xi^2$. All terms then share a common factor a_σ^6, and the final potential that we use, rescaled by that factor, is then:

$$
\begin{aligned}
-\mathcal{U}_{ani}/a_\sigma^6 \;&=\; C_1(\xi)\mathrm{Tr}\big(\xi_5\Sigma\xi_5\Sigma^\dagger\big)\\
&+\; C_3(\xi)\frac{1}{2}\sum_j\Big[\mathrm{Tr}\big(\xi_j\Sigma\xi_j\Sigma\big)+\mathrm{Tr}\big(\xi_j\Sigma^\dagger\xi_j\Sigma^\dagger\big)\Big]\\
&+\; D_3(\xi)\frac{1}{2}\Big[\mathrm{Tr}\big(\xi_4\Sigma\xi_4\Sigma\big)+\mathrm{Tr}\big(\xi_4\Sigma^\dagger\xi_4\Sigma^\dagger\big)\Big]\\
&+\; C_4(\xi)\frac{1}{2}\sum_j\Big[\mathrm{Tr}\big(\xi_{j5}\Sigma\xi_{5j}\Sigma\big)+\mathrm{Tr}\big(\xi_{j5}\Sigma^\dagger\xi_{5j}\Sigma^\dagger\big)\Big]\\
&+\; D_4(\xi)\frac{1}{2}\Big[\mathrm{Tr}\big(\xi_{45}\Sigma\xi_{54}\Sigma\big)+\mathrm{Tr}\big(\xi_{45}\Sigma^\dagger\xi_{54}\Sigma^\dagger\big)\Big]\\
&+\; C_6(\xi)\sum_{j<k}\mathrm{Tr}\big(\xi_{jk}\Sigma\xi_{kj}\Sigma^\dagger\big)\\
&+\; D_6(\xi)\sum_j\mathrm{Tr}\big(\xi_{j4}\Sigma\xi_{4j}\Sigma^\dagger\big).
\end{aligned}
\tag{5.19}
$$

In general, the low-energy constants are functions of two lattice spacings, a_σ and a_τ. We remind the reader that in this study $a_\sigma = \mathrm{const}$, thus the dependence is on a single parameter, ξ. From this point on, for ease of notation, we include the constant prefactor $16a_\sigma^2/f^2$ into the definition of the low-energy constants, i.e., we rescale, e.g., $16a_\sigma^2/f^2 C_i \to C_i$. By definition, $D_i(\xi = 1) \equiv C_i(\xi = 1)$.

The taste splittings derived in the same way as before for the potential in Eq. (5.19) are:

$$\delta M_{45}(\xi) = C_1(\xi) + 3C_3(\xi) + D_4(\xi) + 3D_6(\xi), \tag{5.20}$$

$$\delta M_{i5}(\xi) = C_1(\xi) + 2C_3(\xi) + D_3(\xi) + C_4(\xi) + 2C_6(\xi) + D_6(\xi), \tag{5.21}$$

$$\delta M_{ij}(\xi) = C_3(\xi) + D_3(\xi) + C_4(\xi) + D_4(\xi) + 2C_6(\xi) + 2D_6(\xi), \tag{5.22}$$

$$\delta M_{i4}(\xi) = 2C_3(\xi) + 2C_4(\xi) + 2C_6(\xi) + 2D_6(\xi), \tag{5.23}$$

$$\delta M_{i}(\xi) = C_1(\xi) + C_3(\xi) + 2C_4(\xi) + D_4(\xi) + 2C_6(\xi) + D_6(\xi), \tag{5.24}$$

$$\delta M_{4}(\xi) = C_1(\xi) + D_3(\xi) + 3C_4(\xi) + 3D_6(\xi), \tag{5.25}$$

$$\delta M_{s}(\xi) = 3C_3(\xi) + D_3(\xi) + 3C_4(\xi) + D_4(\xi). \tag{5.26}$$

Now there are seven taste splittings that depend on seven low-energy constants. Inverting the dependence allows us to express the low-energy constants in terms of the data for the taste splittings

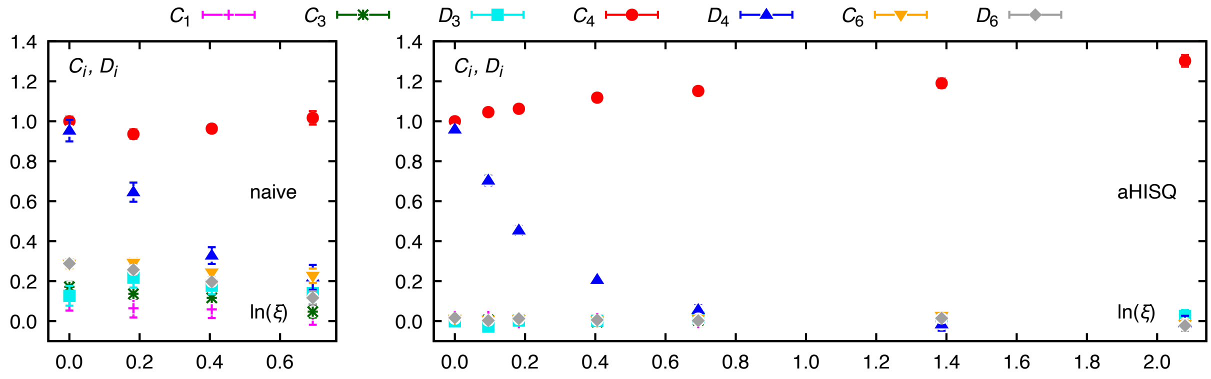

Figure 5.15 The low-energy constants C_i and D_i as functions of $\ln(\xi)$ for the naive staggered (left) and aHISQ (right) action. For comparison, the values on the left are divided by $C_4(\xi = 1) = 0.0974(22)$ for the naive staggered and on the right by $C_4(\xi = 1) = 0.02914(37)$ for the aHISQ action.

as functions of anisotropy:

$$C_1(\xi) = \frac{1}{8}(\ \ \delta M_{45}(\xi) + 3\delta M_{i5}(\xi) - 3\delta M_{ij}(\xi) - 3\delta M_{i4}(\xi) + 3\delta M_i(\xi) + \delta M_4(\xi) - \delta M_s(\xi)), \tag{5.27}$$

$$C_3(\xi) = \frac{1}{8}(\ \ \delta M_{45}(\xi) + \delta M_{i5}(\xi) - \delta M_{ij}(\xi) + \delta M_{i4}(\xi) - \delta M_i(\xi) - \delta M_4(\xi) + \delta M_s(\xi)), \tag{5.28}$$

$$D_3(\xi) = \frac{1}{8}(-\delta M_{45}(\xi) + 3\delta M_{i5}(\xi) + 3\delta M_{ij}(\xi) - 3\delta M_{i4}(\xi) - 3\delta M_i(\xi) + \delta M_4(\xi) + \delta M_s(\xi)), \tag{5.29}$$

$$C_4(\xi) = \frac{1}{8}(-\delta M_{45}(\xi) - \delta M_{i5}(\xi) - \delta M_{ij}(\xi) + \delta M_{i4}(\xi) + \delta M_i(\xi) + \delta M_4(\xi) + \delta M_s(\xi)), \tag{5.30}$$

$$D_4(\xi) = \frac{1}{8}(\ \ \delta M_{45}(\xi) - 3\delta M_{i5}(\xi) + 3\delta M_{ij}(\xi) - 3\delta M_{i4}(\xi) + 3\delta M_i(\xi) - \delta M_4(\xi) + \delta M_s(\xi)), \tag{5.31}$$

$$C_6(\xi) = \frac{1}{8}(-\delta M_{45}(\xi) + \delta M_{i5}(\xi) + \delta M_{ij}(\xi) + \delta M_{i4}(\xi) + \delta M_i(\xi) - \delta M_4(\xi) - \delta M_s(\xi)), \tag{5.32}$$

$$D_6(\xi) = \frac{1}{8}(\ \ \delta M_{45}(\xi) - \delta M_{i5}(\xi) + \delta M_{ij}(\xi) + \delta M_{i4}(\xi) - \delta M_i(\xi) + \delta M_4(\xi) - \delta M_s(\xi)). \tag{5.33}$$

These dependencies are shown in Fig. 5.15. As expected, for aHISQ (right panel) only $C_4(\xi)$ and $D_4(\xi)$ contribute to the taste splittings, while the other low-energy constants stay close to 0 also for $\xi > 1$. For the naive staggered action (left panel) the situation is different: while the splittings are also dominated by $C_4(\xi)$ and $D_4(\xi)$, the other low-energy constants are also sizeable. It appears that $C_4(\xi)$ increases, similar to aHISQ. Importantly, $C_1(\xi)$ and $C_3(\xi)$ decrease with anisotropy, consistent with the expectation of δM_{45} going to 0.

For aHISQ taste splittings the dependence on anisotropy is then simplified:

$$\delta M_{45}(\xi) = 0 \cdot C_4(\xi) + 1 \cdot D_4(\xi), \tag{5.34}$$

$$\delta M_{i5}(\xi) = 1 \cdot C_4(\xi) + 0 \cdot D_4(\xi), \tag{5.35}$$

$$\delta M_{ij}(\xi) = 1 \cdot C_4(\xi) + 1 \cdot D_4(\xi), \tag{5.36}$$

$$\delta M_{i4}(\xi) = 2 \cdot C_4(\xi) + 0 \cdot D_4(\xi), \tag{5.37}$$

$$\delta M_{i}(\xi) = 2 \cdot C_4(\xi) + 1 \cdot D_4(\xi), \tag{5.38}$$

$$\delta M_{4}(\xi) = 3 \cdot C_4(\xi) + 0 \cdot D_4(\xi), \tag{5.39}$$

$$\delta M_{s}(\xi) = 3 \cdot C_4(\xi) + 1 \cdot D_4(\xi). \tag{5.40}$$

Equations (5.34)–(5.40) reveal an interesting feature of the aHISQ taste splittings. Consider, for instance, the vector, $\gamma_5 \otimes \xi_i$ taste, Eq. (5.38). Given that $\gamma_5 = \gamma_1\gamma_2\gamma_3\gamma_4$, an interpolating operator requires 4 shifts to build the spin and 1 shift to build the taste structure. The spatial taste shift can balance one spatial spin shift, so in total there are $l_\sigma = 2$ and $l_\tau = 1$ unbalanced shifts, i.e., gauge links in the interpolating operator for the $\gamma_5 \otimes \xi_i$ taste, as discussed in Sec. 4.5. (From this consideration, the Goldstone taste, $\gamma_5 \otimes \xi_5$ is, of course, local, as there are four spin and four taste shifts that can balance each other.) The values $l_\sigma = 2$ and $l_\tau = 1$ are precisely the coefficients in front of $C_4(\xi)$ and $D_4(\xi)$ in Eq. (5.38). One can easily check that this interpretation of the coefficients applies to all aHISQ splittings in Eqs. (5.34)–(5.40).

Our next step is to determine what functional forms may describe the anisotropy dependence of the low-energy constants $C_4(\xi)$ and $D_4(\xi)$. At the first stage, we fit them individually and do not enforce the constraint $D_4(\xi = 1) = C_4(\xi = 1)$. That constraint is automatically incorporated in the final global fit.

It appears that the D_4 data strongly favors a power law. A fit to the form (D_4 fit 1):

$$D_4(\xi) = d_1 + \frac{d_2}{\xi^{d_3}} \tag{5.41}$$

produces $d_1 = -0.00050(62)$, $d_2 = 0.02855(72)$ and $d_3 = 3.70(23)$ with $\chi^2/\text{dof} = 0.9$. As the closest integer power is $d_3 = 4$ and d_1 is consistent with 0, as expected, a fit to a simplified form

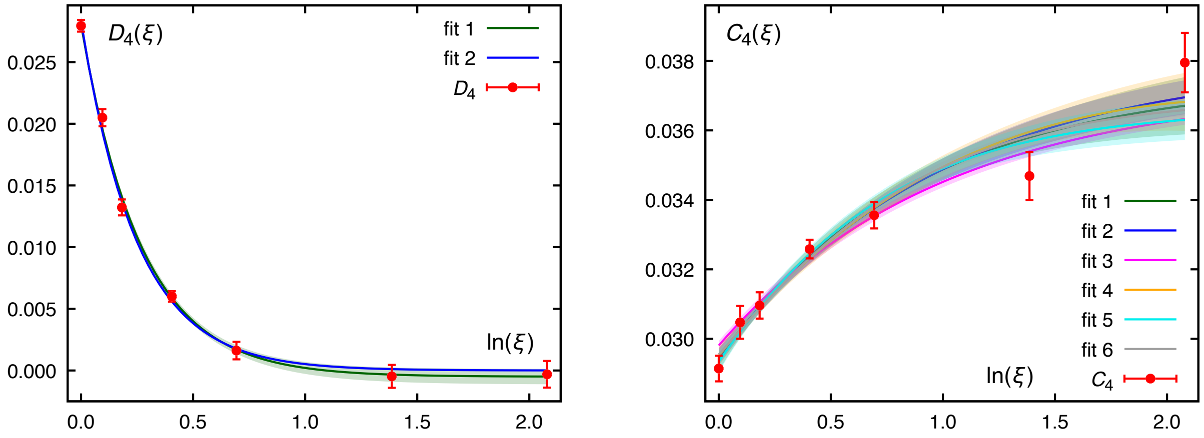

Figure 5.16 The low-energy constants D_4 (left) and C_4 (right) determined from the aHISQ pion taste splittings as functions of $\ln(\xi)$. The bands represent the fits described in the text.

(D_4 fit 2):

$$D_4(\xi) = \frac{d_2}{\xi^4} \tag{5.42}$$

gives $d_2 = 0.02830(40)$ with $\chi^2/\text{dof} = 0.9$. The two fits described above are shown in Fig. 5.16, left. We note that fits to the form

$$D_4(\xi) = d_1 + d_2 \frac{\ln(\xi)}{\xi^{d_3}} \tag{5.43}$$

are disfavored by the data, with χ^2/dof of order ten.

Next, we examine the dependence $C_4(\xi)$ where we find the data to be less constraining. A fit to the form (C_4 fit 1):

$$C_4(\xi) = c_1 \left(1 - \frac{c_2}{\xi^{c_3}}\right) \tag{5.44}$$

produces $c_1 = 0.0375(12)$, $c_2 = 0.215(24)$ and $c_3 = 1.14(31)$ with $\chi^2/\text{dof} = 1.6$. The power is consistent with 1, so we fix $c_3 = 1$, then the fit (C_4 fit 2) produces $c_1 = 0.03802(51)$, $c_2 = 0.225(15)$ with $\chi^2/\text{dof} = 1.3$. Fixing also $c_2 = 1/5$ (C_4 fit 3) gives $c_1 = 0.03726(18)$ with $\chi^2/\text{dof} = 1.5$. In general, we also expect some logarithmic dependence on ξ (if perturbation theory is applicable, one expects the coupling also to appear in the expansion). We therefore also try (C_4 fit 4):

$$C_4(\xi) = c_1 + c_2 \frac{\ln(\xi)}{\xi^{c_3}} \tag{5.45}$$

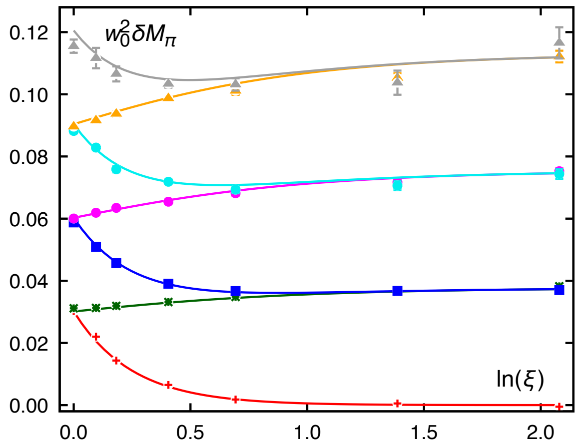

Figure 5.17 Splittings of the aHISQ pion taste multiplets from the Goldstone pion, same as in Fig. 5.13 (right), but in units of $1/w_0^2$, as function of $\ln(\xi)$. The lines represent a joint fit of all data points to the functional form in Eq. (5.47) with a single fit parameter c (overall amplitude).

that gives $c_1 = 0.02951(29)$, $c_2 = 0.0081(12)$ and $c_3 = 0.403(92)$ with $\chi^2/\text{dof} = 1.9$. We interpret the appearance of non-integer powers of ξ as masking some more complicated dependence, still resolvable by the data, and try (C_4 fit 5):

$$C_4(\xi) = c_1\left(1 - (c_2 + c_3\ln(\xi))\,\frac{1}{\xi^2}\right) \tag{5.46}$$

that produces $c_1 = 0.03658(68)$, $c_2 = 0.198(16)$ and $c_3 = 0.140(78)$ with $\chi^2/\text{dof} = 1.9$.

Fixing $c_2 = c_3 = 1/5$ (C_4 fit 6) gives $c_1 = 0.03694(18)$ with $\chi^2/\text{dof} = 1.4$. The six fit forms described above together with the data are shown in Fig. 5.16 (right). We give preference to the fits that contain even powers, and possibly logarithms, of the anisotropy ξ.

Now we combine the fit forms for C_4 and D_4 into a single form that we use to fit the aHISQ splittings directly:

$$\delta M_\pi(\xi) = c\left(l_\sigma \cdot \frac{5}{4}\left(1 - \frac{1}{5}\,(1 + \ln(\xi))\,\frac{1}{\xi^2}\right) + l_\tau \cdot \frac{1}{\xi^4}\right), \tag{5.47}$$

where l_σ and l_τ as before are, respectively, the number of unbalanced spatial and temporal links in the interpolating operators. The $5/4$ coefficient in the first term ensures that in the isotropic limit $\xi = 1$ the expression reduces to $c(l_\sigma + l_\tau)$. The remaining fit parameter c is determined by simultaneously fitting all aHISQ splittings to Eq. (5.47) which gives $c = 0.030129(31)$ and $\chi^2/\text{dof} = 3.2$. While the χ^2/dof is somewhat high, the functional form (5.47) captures the main features of the aHISQ splittings remarkably well, as shown in Fig. 5.17. One of the factors contributing to the high χ^2/dof is the fact that the model inherits some inaccuracy present already in the isotropic case: Eqs. (5.34)–(5.40) that reduce to the known forms of [Lee and Sharpe, 1999] predict that the isotropic splittings for the axial, tensor, vector and singlet taste multiplets form ratios 1:2:3:4, while the data show a slightly different pattern 1:1.94:2.92:3.82 which is due to the small but non-negligible dependence on the C_1, C_3 and C_6 low-energy constants.

The χ^2/dof can be brought close to 1 by introducing different amplitudes c for different splittings and/or introducing fit parameters in the parentheses in Eq. (5.47). We, however, prefer the simplest fit with minimal number of free parameters.

Curiously, one can arrive at an empirical model that captures main features of the aHISQ taste splittings from considerations very different from the staggered chiral perturbation theory inspired approach described above. (In fact, we found that model first, and that allowed us to introduce proper modifications to the chiral perturbation theory-inspired model.) As the origin and the quantitative dependence of the taste splittings on the lattice spacing, and in our case, anisotropy, are not fully understood, we believe, it is useful for future studies to document those considerations here.

Let us first consider introducing the anisotropy $\xi > 1$ as a symmetry-breaking perturbation. We can estimate how it affects the fluctuations of spatial and temporal links. Consider plaquettes normalized to the value at $\xi = 1$: $Q_{\mu\nu} = P_{\mu\nu}(\xi)/P_{\mu\nu}(\xi = 1)$. Similar to tadpole factors, we can define $u_\sigma(\xi) = \sqrt[4]{Q_{\sigma\sigma}}$ and $u_\tau(\xi) = \sqrt[4]{Q_{\sigma\tau}^2/Q_{\sigma\sigma}}$ as proxies for average spatial and temporal link fluctuations, respectively. For $\xi > 1$ $u_\tau(\xi)$ is growing, as temporal links fluctuate less and get closer to 1, while $u_\sigma(\xi)$ is decreasing, as the spatial links fluctuate more and get farther from 1. Using the data from Table A.2 one finds that (at least, for small anisotropies, $1 < \xi \lesssim 2$) $u_\tau(\xi) - 1 \approx 3.7(1 - u_\sigma(\xi))$, i.e., per one unit of increase in fluctuations in the spatial links, there are 3.7 units of decrease in fluctuations in the temporal links. While the prefactor is not exactly 3 (the number of spatial dimensions), it is plausible to assume a picture similar to how a symmetry-breaking perturbation often affects the spectrum, by redistributing the energy according to multiplicities of the levels with the net change being 0.

This picture is generally familiar, from Grotrian diagrams of fine structure and hyperfine structure in atomic physics, or from the eightfold way [Gell-Mann, 1964]: the larger strange quark mass (or, more precisely, $(m_s - m_l)/(2m_l + m_s) \simeq 0.90$) acts as a symmetry breaking perturbation from the SU(3) flavor symmetric point and, for instance, the baryon decuplet masses split according to their multiplicities in such a way that the weighted average mass stays invariant (up to per mill level amount of about 2 MeV due to the isospin breaking effects). The Δ state masses are lowered and the Ξ^* and Ω are raised, while the Σ^* states stay at the symmetric point. The analog to the symmetry breaking by the strange quark mass for the anisotropic case is that one temporal link getting smoother is exactly balanced by three spatial links getting rougher.

Next, the aHISQ splittings in Fig. 5.13 exhibit approximately equidistant pattern and they are ordered by the number of unbalanced links in the interpolating operator. Let the first splitting between the Goldstone and the axial vector taste be denoted δE. Then

$$\delta M_\pi = (l_\sigma + l_\tau)\,\delta E. \tag{5.48}$$

We stress that this formula does not depend on the structure of Eqs. (5.34)–(5.40) that we discussed previously and follows from the aHISQ data alone (i.e., equidistant multiplets and ordering by the number of unbalanced links). Let us assume that δM_s is independent of anisotropy and equal to the value at $\xi = 1$, then $\delta E = \delta M_s/4$. (The deviation of δM_s from constant is about 17%, Fig. 5.13). How can anisotropy be introduced into Eq. (5.48) from the perspective of a symmetry-breaking perturbation? We can view the taste-breaking effects as the amount of energy associated with the individual fluctuations of the unbalanced gauge links in the interpolating operators. After all, the number of unbalanced links is the number of additional links that an anti-quark needs to hop relative to the quark in a pion taste heavier than the Goldstone taste. This picture of independent link fluctuations immediately explains why the isotropic HISQ splittings are ordered the way they are: axial vector taste (1 unbalanced link), tensor (2), vector (3) and singlet (4 unbalanced links). (And this argument largely applies also to the naive staggered case, since, as Fig. 5.15 shows, the naive splittings are dominated by the C_4 low-energy constant.)

If we assume that the symmetry-breaking perturbation for the gauge links can be described by some positive increasing universal function $f(\xi)$ with the limiting behavior $f(\xi \to 1) \to 0$ and

$f(\xi \to \infty) \to 1$, and that the "units of fluctuations" distribute themselves between the temporal and spatial links as 3:1, it is natural to modify Eq. (5.48) in the following way:

$$\delta M_\pi(\xi) = \left(l_\sigma \left(1 + \frac{1}{3} f(\xi) \right) + l_\tau \left(1 - f(\xi) \right) \right) \delta E. \tag{5.49}$$

The way $f(\xi)$ is defined, the $1 - f(\xi)$ in the temporal part shows that the temporal links are becoming smoother with ξ growing and contribute less fluctuations, while $1 + f(\xi)/3$ in the spatial part reflects the opposite: the spatial links are getting rougher and contribute more fluctuations, in proportion 1:3 relative to the temporal links. In this model, the taste splittings based on Eq. (5.49) are

$$\begin{aligned}
\delta M_{45}(\xi) &= \frac{3}{3} \left(1 - f(\xi) \right) \delta E, && (5.50)\\
\delta M_{i5}(\xi) &= \frac{1}{3} \left(3 + f(\xi) \right) \delta E, && (5.51)\\
\delta M_{ij}(\xi) &= \frac{2}{3} \left(3 - f(\xi) \right) \delta E, && (5.52)\\
\delta M_{i4}(\xi) &= \frac{2}{3} \left(3 + f(\xi) \right) \delta E, && (5.53)\\
\delta M_{i}(\xi) &= \frac{1}{3} \left(9 - f(\xi) \right) \delta E, && (5.54)\\
\delta M_{4}(\xi) &= \frac{3}{3} \left(3 + f(\xi) \right) \delta E, && (5.55)\\
\delta M_{s}(\xi) &= \frac{3}{3}\, 4 \delta E. && (5.56)
\end{aligned}$$

This model captures the crucial feature of the aHISQ taste splittings observed in the data: the masses of the $\xi_i\xi_5$, $\xi_i\xi_4$ and ξ_4 tastes increase with anisotropy, the splittings differ only by a multiplicative factor, in proportion 1:2:3, and $\delta M_{45} \to 0$ as $\xi \to \infty$. If one forms ratios that cancel δE and isolate $f(\xi)$:

$$f(\xi) = 3\, \frac{\delta M_{i5}(\xi) - \delta M_{45}(\xi)}{3\delta M_{i5}(\xi) + \delta M_{45}(\xi)} = 3\, \frac{\delta M_{i4}(\xi) - \delta M_{ij}(\xi)}{\delta M_{i4}(\xi) + \delta M_{ij}(\xi)} = 9\, \frac{\delta M_{4}(\xi) - \delta M_{i}(\xi)}{\delta M_{4}(\xi) + 3\delta M_{i}(\xi)}, \tag{5.57}$$

one indeed finds data collapse confirming that $f(\xi)$ is a universal function. This feature is independent from the assumption of δE being constant. Therefore, to accommodate the observed dependence of δE on anisotropy, one can form linear combinations that cancel $f(\xi)$ and allow one to study the isolated dependence $\delta E(\xi)$.

At this stage, however, it is more convenient to connect the qualitative model to the staggered chiral perturbation theory inspired model, as the latter separates the anisotropy dependence of the taste splitting more cleanly. Matching Eqs. (5.50)–(5.56) with Eqs. (5.34)–(5.40) one finds that

$$\delta E(\xi) = \frac{1}{4}(3C_4(\xi) + D_4(\xi)) \tag{5.58}$$

and

$$f(\xi) = 3\,\frac{C_4(\xi) - D_4(\xi)}{3C_4(\xi) + D_4(\xi)}, \tag{5.59}$$

so that $f(\xi)$ is indeed a universal increasing function with proper limits.

Another interesting observation for aHISQ is that as $\delta M_s(\xi = 8) \simeq \delta M_s(\xi = 1)$, the five approximately equidistant taste multiplets (counting also the Goldstone $\gamma_5 \otimes \xi_5$ taste for which by definition $\delta M_5 = 0$) at $\xi = 1$ rearrange themselves at $\xi = 8$ into four approximately equidistant multiplets with the unit of splitting being $4/3\,\delta E$, Fig. 5.13 (right), as the qualitative model predicts: Eqs. (5.50)–(5.56) with $f(\xi \to \infty) \to 1$ give the pattern $\{0, 1, 1, 2, 2, 3, 3\} \times 4/3\,\delta E$. (This is also not at odds with the limiting behavior of Eq. (5.47), if one observes that at the largest anisotropy $\xi = 8$ δE has a smaller value: taking $\delta E \to 15/16\,\delta E$ would produce a unit of splitting $5/4\,\delta E$, as dictated by Eq. (5.47).) If $\xi = 8$ can be considered large enough to represent the $\xi \to \infty$ limit, and whether this behavior of δE (i.e., δM_s) is similar at smaller spatial lattice spacing a_σ remains to be uncovered.

CHAPTER 6

OUTLOOK

6.1 Tuning dynamical ensembles

6.2 NRQCD

6.3 Spectral reconstruction

BIBLIOGRAPHY

[Adler, 1988] Adler, S. L. (1988). Overrelaxation Algorithms for Lattice Field Theories. *Phys. Rev. D*, 37:458.

[Adobe Systems Incorporated, 1992] Adobe Systems Incorporated (1992). Encapsulated postscript file format specification. Technical Report Developer Note #5002, Adobe Systems Incorporated.

[Aitchison and Hey, 2013] Aitchison, I. J. R. and Hey, A. J. G. (2013). *Gauge Theories in Particle Physics, 40th Anniversary Edition: A Practical Introduction, Volume 2*. Taylor & Francis.

[Allton, 1997] Allton, C. R. (1997). Lattice Monte Carlo data versus perturbation theory. *Nucl. Phys. B Proc. Suppl.*, 53:867–869.

[Altmann and Cracknell, 1965] Altmann, S. L. and Cracknell, A. P. (1965). Lattice Harmonics 1. Cubic Groups. *Rev. Mod. Phys.*, 37:19–32.

[Aoki et al., 2026] Aoki, Y. et al. (2026). FLAG review 2024. *Phys. Rev. D*, 113(1):014508.

[Aubin and Bernard, 2003] Aubin, C. and Bernard, C. (2003). Pion and kaon masses in staggered chiral perturbation theory. *Phys. Rev. D*, 68:034014.

[Bazavov, 2021] Bazavov, A. (2021). Commutator-free Lie group methods with minimum storage requirements and reuse of exponentials. *BIT Numerical Mathematics*, 62(3):745–771.

[Bazavov, 2025] Bazavov, A. (2025). 2N-storage Runge-Kutta methods: c-reflection symmetry and factorization of the Butcher tableau.

[Bazavov, 2026] Bazavov, A. (2026). 2n-storage runge-kutta methods: Order conditions, general properties and some analytic solutions. *BIT Numerical Mathematics*, 66(2):38.

[Bazavov and Chuna, 2021] Bazavov, A. and Chuna, T. (2021). Efficient integration of gradient flow in lattice gauge theory and properties of low-storage commutator-free Lie group methods.

[Bazavov et al., 2010a] Bazavov, A. et al. (2010a). Nonperturbative QCD Simulations with 2+1 Flavors of Improved Staggered Quarks. *Rev. Mod. Phys.*, 82:1349–1417.

[Bazavov et al., 2010b] Bazavov, A. et al. (2010b). Scaling studies of QCD with the dynamical HISQ action. *Phys. Rev. D*, 82:074501.

[Bazavov et al., 2013] Bazavov, A. et al. (2013). Lattice QCD Ensembles with Four Flavors of Highly Improved Staggered Quarks. *Phys. Rev. D*, 87(5):054505.

[Bazavov et al., 2026] Bazavov, A. et al. (2026). High-precision scale setting with the Ω-baryon mass and gradient flow. *Phys. Rev. D*, 113(5):054501.

[Berg and Billoire, 1983] Berg, B. and Billoire, A. (1983). Glueball Spectroscopy in Four-Dimensional SU(3) Lattice Gauge Theory. 1. *Nucl. Phys. B*, 221:109–140.

[Berland et al., 2006] Berland, J., Bogey, C., and Bailly, C. (2006). Low-dissipation and low-dispersion fourth-order Runge-Kutta algorithm. *Computers and Fluids*, 35(10):1459 – 1463.

[Bernard, 2002] Bernard, C. (2002). Chiral logs in the presence of staggered flavor symmetry breaking. *Phys. Rev. D*, 65:054031.

[Bernard et al., 2007] Bernard, C., Golterman, M., Shamir, Y., and Sharpe, S. R. (2007). Comment on 'Chiral anomalies and rooted staggered fermions'. *Phys. Lett. B*, 649:235–240.

[Bilson-Thompson et al., 2003] Bilson-Thompson, S. O., Leinweber, D. B., and Williams, A. G. (2003). Highly improved lattice field strength tensor. *Annals Phys.*, 304:1–21.

[Birman, 1984] Birman, J. (1984). *Theory of Crystal Space Groups and Lattice Dynamics: Infrared and Raman Optical Processes of Insulating Crystals*. Handbuch der Physik. Springer-Verlag.

[Blum et al., 1997] Blum, T., Detar, C. E., Gottlieb, S. A., Rummukainen, K., Heller, U. M., Hetrick, J. E., Toussaint, D., Sugar, R. L., and Wingate, M. (1997). Improving flavor symmetry in the Kogut-Susskind hadron spectrum. *Phys. Rev. D*, 55:R1133–R1137.

[Borsanyi et al., 2012a] Borsanyi, S., Dürr, S., Fodor, Z., Hoelbling, C., Katz, S. D., Krieg, S., Kurth, T., Lellouch, L., Lippert, T., and McNeile, C. (2012a). High-precision scale setting in lattice QCD. *JHEP*, 09:010.

[Borsanyi et al., 2012b] Borsanyi, S., Durr, S., Fodor, Z., Katz, S. D., Krieg, S., Kurth, T., Mages, S., Schafer, A., and Szabo, K. K. (2012b). Anisotropy tuning with the Wilson flow.

[Borsanyi et al., 2018] Borsanyi, S., Fodor, Z., Giordano, M., Katz, S. D., Pasztor, A., Ratti, C., Schäfer, A., Szabo, K. K., and Tóth, B. (2018). High statistics lattice study of stress tensor correlators in pure $SU(3)$ gauge theory. *Phys. Rev. D*, 98(1):014512.

[Cabibbo and Marinari, 1982] Cabibbo, N. and Marinari, E. (1982). A New Method for Updating SU(N) Matrices in Computer Simulations of Gauge Theories. *Phys. Lett. B*, 119:387–390.

[Clark and Kennedy, 2004] Clark, M. A. and Kennedy, A. D. (2004). The RHMC algorithm for two flavors of dynamical staggered fermions. *Nucl. Phys. B Proc. Suppl.*, 129:850–852.

[Clark and Kennedy, 2007a] Clark, M. A. and Kennedy, A. D. (2007a). Accelerating dynamical fermion computations using the rational hybrid Monte Carlo (RHMC) algorithm with multiple pseudofermion fields. *Phys. Rev. Lett.*, 98:051601.

[Clark and Kennedy, 2007b] Clark, M. A. and Kennedy, A. D. (2007b). Accelerating Staggered Fermion Dynamics with the Rational Hybrid Monte Carlo (RHMC) Algorithm. *Phys. Rev. D*, 75:011502.

[Creutz, 1980] Creutz, M. (1980). Monte Carlo Study of Quantized SU(2) Gauge Theory. *Phys. Rev. D*, 21:2308–2315.

[Creutz, 1987] Creutz, M. (1987). Overrelaxation and Monte Carlo Simulation. *Phys. Rev. D*, 36:515.

[Creutz, 2007] Creutz, M. (2007). Chiral anomalies and rooted staggered fermions. *Phys. Lett. B*, 649:230–234.

[Davies et al., 2010] Davies, C. T. H., Follana, E., Kendall, I. D., Lepage, G. P., and McNeile, C. (2010). Precise determination of the lattice spacing in full lattice QCD. *Phys. Rev. D*, 81:034506.

[DeGrand and Detar, 2006] DeGrand, T. and Detar, C. E. (2006). *Lattice methods for quantum chromodynamics*.

[Duane et al., 1987] Duane, S., Kennedy, A. D., Pendleton, B. J., and Roweth, D. (1987). Hybrid Monte Carlo. *Phys. Lett. B*, 195:216–222.

[Fabricius and Haan, 1984] Fabricius, K. and Haan, O. (1984). Heat Bath Method for the Twisted Eguchi-Kawai Model. *Phys. Lett. B*, 143:459–462.

[Fodor et al., 2014] Fodor, Z., Holland, K., Kuti, J., Mondal, S., Nogradi, D., and Wong, C. H. (2014). The lattice gradient flow at tree-level and its improvement. *JHEP*, 09:018.

[Follana et al., 2007] Follana, E., Mason, Q., Davies, C., Hornbostel, K., Lepage, G. P., Shigemitsu, J., Trottier, H., and Wong, K. (2007). Highly improved staggered quarks on the lattice, with applications to charm physics. *Phys. Rev. D*, 75:054502.

[Gattringer and Lang, 2010] Gattringer, C. and Lang, C. B. (2010). *Quantum chromodynamics on the lattice*, volume 788. Springer, Berlin.

[Gell-Mann, 1964] Gell-Mann, M. (1964). A Schematic Model of Baryons and Mesons. *Phys. Lett.*, 8:214–215.

[Ginsparg and Wilson, 1982] Ginsparg, P. H. and Wilson, K. G. (1982). A Remnant of Chiral Symmetry on the Lattice. *Phys. Rev. D*, 25:2649.

[Golterman, 2024] Golterman, M. (2024). Staggered fermions.

[Golterman, 1986a] Golterman, M. F. L. (1986a). Irreducible Representations of the Staggered Fermion Symmetry Group. *Nucl. Phys. B*, 278:417–435.

[Golterman, 1986b] Golterman, M. F. L. (1986b). Staggered Mesons. *Nucl. Phys. B*, 273:663–676.

[Golterman and Smit, 1984] Golterman, M. F. L. and Smit, J. (1984). Selfenergy and Flavor Interpretation of Staggered Fermions. *Nucl. Phys. B*, 245:61–88.

[Golterman and Smit, 1985] Golterman, M. F. L. and Smit, J. (1985). Lattice Baryons With Staggered Fermions. *Nucl. Phys. B*, 255:328–340.

[Gottlieb et al., 1987] Gottlieb, S. A., Liu, W., Toussaint, D., Renken, R. L., and Sugar, R. L. (1987). Hybrid Molecular Dynamics Algorithms for the Numerical Simulation of Quantum Chromodynamics. *Phys. Rev. D*, 35:2531–2542.

[Hamermesh, 1962] Hamermesh, M. (1962). *Group theory and its application to physical problems*. Addison-Wesley.

[Hasenfratz and Hasenfratz, 1981] Hasenfratz, A. and Hasenfratz, P. (1981). The scales of euclidean and hamiltonian lattice qcd. *Nuclear Physics B*, 193(1):210–220.

[Jansen and Boon, 1967] Jansen, L. and Boon, M. (1967). *Theory of Finite Groups: Applications in Physics*. Ne67-47. North-Holland Publishing Company.

[Jiang et al., 2023] Jiang, X., Sun, W., Chen, F., Chen, Y., Gong, M., Liu, Z., and Zhang, R. (2023). η-glueball mixing from Nf=2 lattice QCD. *Phys. Rev. D*, 107(9):094510.

[Karsch, 1982] Karsch, F. (1982). SU(N) Gauge Theory Couplings on Asymmetric Lattices. *Nucl. Phys. B*, 205:285–300.

[Kennedy and Pendleton, 1985] Kennedy, A. D. and Pendleton, B. J. (1985). Improved Heat Bath Method for Monte Carlo Calculations in Lattice Gauge Theories. *Phys. Lett. B*, 156:393–399.

[Kilcup and Sharpe, 1987] Kilcup, G. W. and Sharpe, S. R. (1987). A Tool Kit for Staggered Fermions. *Nucl. Phys. B*, 283:493–550.

[Klassen, 1998] Klassen, T. R. (1998). The Anisotropic Wilson gauge action. *Nucl. Phys. B*, 533:557–575.

[Kogut and Susskind, 1975] Kogut, J. B. and Susskind, L. (1975). Hamiltonian Formulation of Wilson's Lattice Gauge Theories. *Phys. Rev. D*, 11:395–408.

[Le Bellac, 2011] Le Bellac, M. (2011). *Thermal Field Theory*. Cambridge Monographs on Mathematical Physics. Cambridge University Press.

[Lee and Sharpe, 1999] Lee, W.-J. and Sharpe, S. R. (1999). Partial flavor symmetry restoration for chiral staggered fermions. *Phys. Rev. D*, 60:114503.

[Lepage, 1997] Lepage, G. P. (1997). Redesigning lattice QCD. *Lect. Notes Phys.*, 479:1–48.

[Lepage, 1999] Lepage, G. P. (1999). Flavor symmetry restoration and Symanzik improvement for staggered quarks. *Phys. Rev. D*, 59:074502.

[Lepage and Mackenzie, 1993] Lepage, G. P. and Mackenzie, P. B. (1993). On the Viability of Lattice Perturbation Theory. *Phys. Rev. D*, 48:2250–2264.

[Lepage and Gohlke, 2025] Lepage, P. and Gohlke, C. (2025). gplepage/lsqfit: lsqfit version 13.3.1.

[Levkova et al., 2006] Levkova, L., Manke, T., and Mawhinney, R. (2006). Two-flavor QCD thermodynamics using anisotropic lattices. *Phys. Rev. D*, 73:074504.

[Lombardo et al., 2025] Lombardo, M. P. et al. (2025). Bottomonium spectral functions in thermal QCD. *J. Subatomic Part. Cosmol.*, 3:100049.

[Luo, 1998] Luo, Y.-b. (1998). On-shell improved lattice QCD with staggered fermions. *Phys. Rev. D*, 57:265–275.

[Lüscher, 2010] Lüscher, M. (2010). Properties and uses of the Wilson flow in lattice QCD. *JHEP*, 08:071. [Erratum: JHEP 03, 092 (2014)].

[Luscher, 2010] Luscher, M. (2010). Trivializing maps, the Wilson flow and the HMC algorithm. *Commun. Math. Phys.*, 293:899–919.

[Luscher and Weisz, 1985] Luscher, M. and Weisz, P. (1985). On-shell improved lattice gauge theories. *Commun. Math. Phys.*, 98(3):433. [Erratum: Commun.Math.Phys. 98, 433 (1985)].

[Montvay and Munster, 1997] Montvay, I. and Munster, G. (1997). *Quantum fields on a lattice*. Cambridge Monographs on Mathematical Physics. Cambridge University Press.

[Naik, 1989] Naik, S. (1989). On-shell Improved Lattice Action for QCD With Susskind Fermions and Asymptotic Freedom Scale. *Nucl. Phys. B*, 316:238–268.

[Namekawa et al., 2001] Namekawa, Y. et al. (2001). Thermodynamics of SU(3) gauge theory on anisotropic lattices. *Phys. Rev. D*, 64:074507.

[Nomura et al., 2004] Nomura, K., Matsufuru, H., and Umeda, T. (2004). Numerical study of staggered quark action on quenched anisotropic lattices. *Prog. Theor. Phys.*, 111:245–264.

[Orginos and Toussaint, 1999] Orginos, K. and Toussaint, D. (1999). Testing improved actions for dynamical Kogut-Susskind quarks. *Phys. Rev. D*, 59:014501.

[Orginos et al., 1999] Orginos, K., Toussaint, D., and Sugar, R. L. (1999). Variants of fattening and flavor symmetry restoration. *Phys. Rev. D*, 60:054503.

[Peskin and Schroeder, 1995] Peskin, M. E. and Schroeder, D. V. (1995). *An Introduction to quantum field theory*. Addison-Wesley, Reading, USA.

[Ramos and Sint, 2016] Ramos, A. and Sint, S. (2016). Symanzik improvement of the gradient flow in lattice gauge theories. *Eur. Phys. J. C*, 76(1):15.

[Rothe, 2012] Rothe, H. J. (2012). *Lattice Gauge Theories : An Introduction (Fourth Edition)*, volume 43. World Scientific Publishing Company.

[Sheikholeslami and Wohlert, 1985] Sheikholeslami, B. and Wohlert, R. (1985). Improved Continuum Limit Lattice Action for QCD with Wilson Fermions. *Nucl. Phys. B*, 259:572.

[Smecca et al., 2025] Smecca, A., Aarts, G., Allton, C., Bignell, R., Jäger, B., Nam, S.-i., Kim, S., Skullerud, J.-I., and Wu, L.-K. (2025). Curvature of the pseudocritical line in the QCD phase diagram from mesonic lattice correlation functions. *Phys. Rev. D*, 112(11):114509.

[Symanzik, 1983] Symanzik, K. (1983). Continuum Limit and Improved Action in Lattice Theories. 1. Principles and φ^4 Theory. *Nucl. Phys. B*, 226:187–204.

[van den Doel and Smit, 1983] van den Doel, C. and Smit, J. (1983). Dynamical Symmetry Breaking in Two Flavor SU(N) and SO(N) Lattice Gauge Theories. *Nucl. Phys. B*, 228:122–144.

[Weinberg, 2005] Weinberg, S. (2005). *The Quantum theory of fields. Vol. 1: Foundations*. Cambridge University Press.

[Weisz, 1983] Weisz, P. (1983). Continuum Limit Improved Lattice Action for Pure Yang-Mills Theory. 1. *Nucl. Phys. B*, 212:1–17.

[Weisz and Wohlert, 1984] Weisz, P. and Wohlert, R. (1984). Continuum Limit Improved Lattice Action for Pure Yang-Mills Theory. 2. *Nucl. Phys. B*, 236:397. [Erratum: Nucl.Phys.B 247, 544 (1984)].

[Wilson, 1974] Wilson, K. G. (1974). Confinement of Quarks. *Phys. Rev. D*, 10:2445–2459.

[Wilson, 1975] Wilson, K. G. (1975). Quarks and Strings on a Lattice. In *13th International School of Subnuclear Physics: New Phenomena in Subnuclear Physics*.

[Wong and Woloshyn, 2007] Wong, K. Y. and Woloshyn, R. M. (2007). Dynamical Simulations with Highly Improved Staggered Quarks. *PoS*, LATTICE2007:047.

APPENDIX A

PURE GAUGE ENSEMBLES

The parameters of the production pure gauge ensembles used for the spectrum studies are documented in Table A.1. The values of the spatial and temporal plaquettes on those ensembles in the normalization $P(\beta \to \infty) = 1$ are documented in Table A.2.

Table A.1 Pure gauge ensembles used in this study, tuned to have the same spatial lattice spacing $a_\sigma \approx 0.1665$ fm in the WC scheme. The first column lists the bare gauge coupling $\beta = 10/g_0^2$, second the bare fermion anisotropy ξ_0, third the target renormalized anisotropy ξ, fourth the lattice volume, fifth the number of configurations used in the flow measurements, sixth the ratio of the spatial and temporal scales which is equal to 1 if the ensemble is properly tuned, seventh the gradient flow scale in units of the spatial lattice spacing and eighth the lattice spacing in fm.

β	ξ_0	ξ	$N_\sigma^3 \times N_\tau$	N_{flow}	$w_{0,\sigma}/w_{0,\tau}$	$w_{0,\sigma}/a_\sigma$	a_σ, fm
6.81823	1	1	$16^3 \times 32$	500	1	1.04147(49)	0.166639(78)
6.84652	1.07865	1.1	$16^3 \times 32$	300	0.99944(26)	1.04393(87)	0.16625(14)
6.87348	1.15792	1.2	$16^3 \times 32$	600	0.99946(30)	1.04411(41)	0.166218(65)
6.94635	1.39939	1.5	$16^3 \times 48$	500	1.00080(43)	1.04090(56)	0.166731(90)
7.04115	1.81411	2	$16^3 \times 64$	440	0.99970(34)	1.04158(79)	0.16662(13)
7.19156	3.48992	4	$16^3 \times 128$	1640	1.00043(17)	1.04165(32)	0.166611(51)
7.26025	6.89327	8	$20^3 \times 320$	320	0.99897(25)	1.03859(78)	0.16710(13)

Table A.2 Spatial, $P_{\sigma\sigma}$ (column 5), and temporal, $P_{\sigma\tau}$ (column 6), plaquettes computed on the production pure gauge ensembles. The meaning of the columns 1–3 is the same as in Table A.1, column 4 lists the number of plaquette measurements.

β	ξ_0	ξ	N_{meas}	$P_{\sigma\sigma}$	$P_{\sigma\tau}$
6.81823	1	1	80,000	0.5815390(34)	0.5815417(32)
6.84652	1.07865	1.1	80,000	0.5663272(36)	0.6023595(29)
6.87348	1.15792	1.2	80,000	0.5528877(50)	0.6207760(34)
6.94635	1.39939	1.5	80,000	0.5214717(30)	0.6662955(16)
7.04115	1.81411	2	40,000	0.4892744(43)	0.7222637(18)
7.19156	3.48992	4	30,000	0.4456197(53)	0.83347145(60)
7.26025	6.89327	8	15,000	0.4282994(20)	0.90823420(26)

APPENDIX B

SPECTRUM FITS

In this appendix we document the results of the fits used to tune the bare fermion anisotropy ξ_0^f for the aHISQ action, as well as the pion taste masses computed on the pure gauge ensembles listed in Table A.1. As discussed in the main text, we used full two-dimensional grid approach to tune the renormalized fermion anisotropy $\xi^f = 1.2$ and 1.5. The results for the energy levels are documented in Tables B.2 and B.3.

For the $\xi^f = 1.1$, 2, 4 and 8 we used a simplified tuning method: one-dimensional search in bare fermion anisotropy at fixed quark mass, then one-dimensional search in quark mass at fixed anisotropy. The results are collected in Tables B.4–B.7. Those tables contain two parts, with the meaning of the columns being different to accommodate finite momentum fits in the first and the mass dependence in the second.

The predicted values of $(a_\sigma m, \xi_0^f)$ for the tuned ensembles are summarized in Table B.8 in columns five and six under the "predicted" header. The actual run parameters, listed in columns seven and eight are discussed in Appendix D.

The masses of different pion tastes for the aHISQ action are shown in Table B.9 and the quadratic mass splittings from the Goldstone taste ξ_5 in Table B.10. Each line of that table corresponds to the same line in Table A.1. The number of configurations used for these measurements for $\xi = 1$ is 4,400, for $\xi = 1.1$ 4,200, for $\xi = 1.2$ 4,000, for $\xi = 1.5$ 4,650, for $\xi = 2$ 2,000, for $\xi = 4$ 1,600 and for $\xi = 8$ 800.

The masses and the quadratic splittings for the naive staggered action are shown in Tables B.11 and B.12, respectively. The number of configurations used for $\xi = 1$ is 4,400, for $\xi = 1.2$ 4,850, for $\xi = 1.5$ 4,650 and for $\xi = 2$ 2,200.

Table B.1 Tuning of the strange quark mass $a_\sigma m_s$ for the aHISQ action on the isotropic pure gauge ensemble ($\beta = 6.81823, \xi_0 = 1$) listed in Table A.1. The first row lists the strange quark mass $a_\sigma m_s$ and second the energy level at zero momentum $a_\tau E(0)$, i.e. the mass of $\eta_{s\bar{s}}$, measured in units of temporal lattice spacing.

$a_\sigma m_s$	0.03	0.05	0.07	0.09	0.11
$a_\tau E(0)$	0.35186(47)	0.45084(43)	0.53190(41)	0.60299(41)	0.66761(41)

Table B.2 Tuning of the bare fermion anisotropy ξ_0^f and the strange quark mass $a_\sigma m_s$ for the aHISQ action on the pure gauge ensemble ($\beta = 6.87348, \xi_0 = 1.15792$) with the renormalized anisotropy $\xi = 1.2$, listed in Table A.1. The first column lists the bare fermion anisotropy ξ_0^f, second the strange quark mass $a_\sigma m_s$, third, fourth and fifth the energy $a_\tau E(\vec{n}^2)$ extracted from the fits of correlation functions at the momentum $\vec{n}$ in lattice units, sixth the renormalized fermion anisotropy as defined by the dispersion relation, Eq. (4.11). The number of configurations used for these measurements $N_{conf} = 950$.

ξ_0^f	$a_\sigma m_s$	$a_\tau E(0)$	$a_\tau E(1)$	$a_\tau E(2)$	ξ^f
1	0.05	0.41582(31)	0.55032(67)	0.65957(201)	1.08821(265)
	0.07	0.49201(32)	0.61089(58)	0.71131(146)	1.08332(227)
	0.09	0.55949(32)	0.66687(56)	0.76027(103)	1.08046(228)
1.2	0.05	0.37596(32)	0.49735(71)	0.59564(143)	1.20437(317)
	0.07	0.44364(33)	0.55034(60)	0.64046(100)	1.20390(275)
	0.09	0.50315(32)	0.59925(54)	0.68256(74)	1.20487(247)
1.4	0.05	0.34569(34)	0.45661(70)	0.54617(117)	1.31483(348)
	0.07	0.40704(34)	0.50411(58)	0.58548(75)	1.31990(290)
	0.09	0.46063(32)	0.54773(52)	0.62301(66)	1.32426(278)

Table B.3 Tuning of the bare fermion anisotropy ξ_0^f and the strange quark mass $a_\sigma m_s$ for the aHISQ action on the pure gauge ensemble ($\beta = 6.94635, \xi_0 = 1.39939$) with the renormalized anisotropy $\xi = 1.5$, listed in Table A.1. The meaning of the columns is the same as in Table B.2. The number of configurations used for these measurements $N_{conf} = 500$.

ξ_0^f	$a_\sigma m_s$	$a_\tau E(0)$	$a_\tau E(1)$	$a_\tau E(2)$	ξ^f
1.05	0.03	0.28705(35)	0.42730(115)	0.53087(160)	1.24236(378)
	0.05	0.36959(36)	0.48803(79)	0.58168(125)	1.23451(350)
	0.07	0.43853(35)	0.54329(64)	0.62976(115)	1.22667(347)
	0.09	0.50001(34)	0.59536(68)	0.67574(104)	1.21911(320)
1.25	0.03	0.26121(32)	0.38896(88)	0.48319(155)	1.36429(406)
	0.05	0.33535(33)	0.44285(64)	0.52824(124)	1.35907(382)
	0.07	0.39674(32)	0.49158(54)	0.57035(107)	1.35406(369)
	0.09	0.45113(32)	0.53726(54)	0.61090(122)	1.34690(367)
1.45	0.03	0.24132(29)	0.35904(70)	0.44580(153)	1.47876(423)
	0.05	0.30911(30)	0.40808(56)	0.48698(160)	1.47447(425)
	0.07	0.36480(32)	0.45205(50)	0.52485(131)	1.47124(394)
	0.09	0.41398(30)	0.49251(43)	0.55990(107)	1.47232(360)
1.65	0.03	0.22524(28)	0.33479(59)	0.41538(144)	1.58728(453)
	0.05	0.28812(28)	0.37963(49)	0.45361(161)	1.58783(435)
	0.07	0.33949(29)	0.41970(43)	0.48710(121)	1.59093(400)
	0.09	0.38448(29)	0.45687(40)	0.51912(82)	1.59167(368)

Table B.4 Simplified tuning of the bare fermion anisotropy ξ_0^f at fixed strange quark mass (upper part of the table) and the strange quark mass $a_\sigma m_s$ tuning at fixed bare fermion anisotropy (lower part of the table) on the pure gauge ensemble ($\beta = 6.84652, \xi_0 = 1.07865$) with the renormalized anisotropy $\xi = 1.1$, listed in Table A.1. The meaning of the columns in the upper part is the same as in Tables B.2 and B.3. The lower part contains measurements only at zero momentum and the meaning of the rows is the same as for the isotropic ensemble in Table B.1 with the additional first column showing the bare fermion anisotropy ξ_0^f at which the measurements were done. The number of configurations used for these measurements is $N_{conf} = 400$.

ξ_0^f	$a_\sigma m_s$	$a_\tau E(0)$	$a_\tau E(1)$	$a_\tau E(2)$	ξ^f
1	0.06	0.47296(63)	0.60457(114)	0.71208(768)	1.04284(477)
1.05	0.06	0.46020(63)	0.58816(112)	0.69302(690)	1.07214(488)
1.1	0.06	0.44842(63)	0.57296(111)	0.67523(618)	1.10095(502)
1.15	0.06	0.43748(63)	0.55882(110)	0.65857(555)	1.12932(517)

ξ_0^f	$a_\sigma m_s$	0.04	0.06	0.08	0.1
1.08	$a_\tau E(0)$	0.37166(66)	0.45302(63)	0.52254(60)	0.58488(57)

Table B.5 Simplified tuning of the bare fermion anisotropy ξ_0^f at fixed strange quark mass (upper part of the table) and the strange quark mass $a_\sigma m_s$ tuning at fixed bare fermion anisotropy (lower part of the table) on the pure gauge ensemble ($\beta = 7.04115, \xi_0 = 1.81411$) with the renormalized anisotropy $\xi = 2$, listed in Table A.1. The layout of the table is the same as in Table B.4. The number of configurations used for the measurements in the upper part is $N_{conf} = 400$, and in the lower part $N_{conf} = 500$.

ξ_0^f	$a_\sigma m_s$	$a_\tau E(0)$	$a_\tau E(1)$	$a_\tau E(2)$	ξ^f	-
1.84	0.07	0.28287(29)	0.34986(62)	0.40691(123)	1.90339(784)	-
1.92	0.07	0.27622(28)	0.34184(55)	0.39717(113)	1.94816(731)	-
2	0.07	0.27001(28)	0.33404(52)	0.38803(105)	1.99493(711)	-
ξ_0^f	$a_\sigma m_s$	0.03	0.05	0.07	0.09	0.11
1.98	$a_\tau E(0)$	0.17986(25)	0.23016(27)	0.27165(25)	0.30815(24)	0.34145(23)

Table B.6 Simplified tuning of the bare fermion anisotropy ξ_0^f at fixed strange quark mass (upper part of the table) and the strange quark mass $a_\sigma m_s$ tuning at fixed bare fermion anisotropy (lower part of the table) on the pure gauge ensemble ($\beta = 7.19156, \xi_0 = 3.48992$) with the renormalized anisotropy $\xi = 4$, listed in Table A.1. The layout of the table is the same as in Table B.4. The number of configurations used for these measurements is $N_{conf} = 500$.

ξ_0^f	$a_\sigma m_s$	$a_\tau E(0)$	$a_\tau E(1)$	$a_\tau E(2)$	ξ^f	-
3.76	0.05	0.11985(12)	0.15803(50)	0.18671(107)	3.83782(2262)	-
3.88	0.05	0.11783(12)	0.15530(45)	0.18355(100)	3.90586(2177)	-
4	0.05	0.11595(13)	0.15269(42)	0.18053(94)	3.97497(2044)	-
ξ_0^f	$a_\sigma m_s$	0.03	0.05	0.07	0.09	0.11
4	$a_\tau E(0)$	0.09060(15)	0.11595(13)	0.13682(12)	0.15520(12)	0.17190(11)

Table B.7 Simplified tuning of the bare fermion anisotropy ξ_0^f at fixed strange quark mass (upper part of the table) and the strange quark mass $a_\sigma m_s$ tuning at fixed bare fermion anisotropy (lower part of the table) on the pure gauge ensemble ($\beta = 7.26025, \xi_0 = 6.89327$) with the renormalized anisotropy $\xi = 8$, listed in Table A.1. The layout of the table is the same as in Table B.4. The number of configurations used for these measurements is $N_{conf} = 300$.

ξ_0^f	$a_\sigma m_s$	$a_\tau E(0)$	$a_\tau E(1)$	$a_\tau E(2)$	ξ^f
7.6	0.07	0.070646(99)	0.08128(14)	0.09097(33)	7.78876(4601)
7.8	0.07	0.069630(95)	0.08013(14)	0.08969(29)	7.89090(4691)
8	0.07	0.068640(83)	0.07900(14)	0.08841(27)	8.00298(4682)
8.2	0.07	0.067721(93)	0.07791(14)	0.08717(27)	8.12518(5046)
ξ_0^f	$a_\sigma m_s$	0.05	0.06	0.07	0.08
7.87	$a_\tau E(0)$	0.058655(94)	0.064172(92)	0.069283(87)	0.074085(83)

Table B.8 Predicted values for the strange quark mass $a_\sigma m_s$ and the bare fermion anisotropy ξ_0^f (columns five and six), and actual values of these parameters (columns seven and eight), used for the splittings measurements. The light quark mass $a_\sigma m_l$ used was equal to one fifth of the actual $a_\sigma m_s$ (column 7). The first column lists the fermion action and the information needed to identify the pure gauge ensembles used, the renormalized anisotropy, gauge coupling and the bare gauge anisotropy is listed in columns two to four, respectively.

				predicted		actual	
action	ξ	β	ξ_0	$a_\sigma m_s$	ξ_0^f	$a_\sigma m_s$	ξ_0^f
naive	1	6.81823	1	0.046575(38)	1	0.04275	1
	1.2	6.87348	1.15792	0.040412(44)	1.0586(28)	0.0374	1.058
	1.5	6.94635	1.39939	0.040159(38)	1.2394(38)	0.0367	1.2348
	2	7.04115	1.81411	0.039816(20)	1.5577(26)	0.03625	1.54707
aHISQ	1	6.81823	1	0.08255(12)	1	0.0762	1
	1.1	6.84652	1.07865	0.08062(18)	1.0983(88)	0.07485	1.08
	1.2	6.87348	1.15792	0.08179(11)	1.1925(44)	0.07605	1.195
	1.5	6.94635	1.39939	0.08150(13)	1.4949(63)	0.0747	1.4972
	2	7.04115	1.81411	0.07917(14)	2.009(12)	0.073	1.98
	4	7.19156	3.48992	0.07805(13)	4.044(35)	0.0723	4
	8	7.26025	6.89327	0.07681(18)	7.986(85)	0.0708	7.87

Table B.9 Masses $a_\tau M_\pi$ of the eight pion tastes with taste structure given in the column header, in units of temporal lattice spacing, for the aHISQ action on pure gauge ensembles. Each line corresponds to an ensemble on the same line of Table A.1.

ξ_5	$\xi_4\xi_5$	$\xi_i\xi_5$	$\xi_i\xi_j$	$\xi_i\xi_4$	ξ_i	ξ_4	1
0.25480(18)	0.30465(54)	0.30600(35)	0.34512(61)	0.34681(53)	0.38242(91)	0.38409(70)	0.41399(238)
0.23202(14)	0.26557(40)	0.27846(29)	0.30404(64)	0.31743(76)	0.34156(86)	0.35113(81)	0.37216(335)
0.21305(17)	0.23351(34)	0.25636(31)	0.27292(55)	0.29293(58)	0.30616(104)	0.32417(85)	0.33655(228)
0.169883(95)	0.17755(17)	0.20608(18)	0.21184(51)	0.23602(38)	0.24153(60)	0.26335(52)	0.26695(96)
0.12721(14)	0.12883(18)	0.15558(26)	0.15696(46)	0.17858(51)	0.17932(75)	0.19871(76)	0.19989(113)
0.063578(83)	0.06382(10)	0.07842(13)	0.07847(27)	0.09040(26)	0.09006(46)	0.10053(42)	0.10009(111)
0.032570(91)	0.032456(55)	0.04018(11)	0.03996(19)	0.04638(14)	0.04624(23)	0.05182(26)	0.05243(69)

Table B.10 Quadratic mass splittings $a_\tau^2(M_\pi^2 - M_5^2)$ of the heavier tastes given in the column headers from the Goldstone taste ξ_5, in units of temporal lattice spacing, for the aHISQ action on pure gauge ensembles. Each line corresponds to an ensemble on the same line of Table A.1. We attribute the negative value for the $\xi_4\xi_5$ splitting at the largest anisotropy $\xi = 8$ (last line) to a fluctuation, as we do not expect any splittings to become negative, and interpret that result as consistent with 0.

$\xi_4\xi_5$	$\xi_i\xi_5$	$\xi_i\xi_j$	$\xi_i\xi_4$	ξ_i	ξ_4	1
0.02789(32)	0.02872(18)	0.05419(43)	0.05535(35)	0.08132(71)	0.08260(52)	0.1065(20)
0.01670(21)	0.02371(14)	0.03861(39)	0.04693(48)	0.06283(58)	0.06946(57)	0.0847(25)
0.00914(14)	0.02033(13)	0.02909(30)	0.04042(31)	0.04834(63)	0.05970(53)	0.0679(15)
0.002664(55)	0.013608(61)	0.01602(22)	0.02684(18)	0.02948(28)	0.04050(27)	0.04240(50)
0.000414(43)	0.008023(65)	0.00845(14)	0.01571(18)	0.01597(27)	0.02330(30)	0.02377(46)
0.000031(13)	0.002107(20)	0.002116(38)	0.004130(48)	0.004068(82)	0.006064(87)	0.00598(22)
-0.0000074(58)	0.000554(10)	0.000536(15)	0.001090(14)	0.001077(22)	0.001624(27)	0.001688(73)

Table B.11 Masses $a_\tau M_\pi$ of the eight pion tastes with taste structure given in the column header, in units of temporal lattice spacing, for the naive staggered action on pure gauge ensembles. The first line with the data corresponds to the ensemble with the renormalized anisotropy $\xi = 1$ in Table A.1, second to $\xi = 1.2$, third to $\xi = 1.5$ and fourth to $\xi = 4$.

ξ_5	$\xi_4\xi_5$	$\xi_i\xi_5$	$\xi_i\xi_j$	$\xi_i\xi_4$	ξ_i	ξ_4	1
0.261611(99)	0.5361(24)	0.5361(17)	0.6116(35)	0.6183(45)	0.6604(72)	0.6607(53)	0.6936(68)
0.214802(96)	0.4042(35)	0.4368(16)	0.4840(38)	0.4973(29)	0.5167(55)	0.5345(54)	0.5471(58)
0.171252(73)	0.2870(15)	0.3375(11)	0.3576(40)	0.3883(32)	0.3921(23)	0.4217(29)	0.4230(49)
0.127119(73)	0.18116(56)	0.24034(89)	0.2520(26)	0.2817(32)	0.2852(36)	0.3104(58)	0.3097(57)

Table B.12 Quadratic mass splittings $a_\tau^2(M_\pi^2 - M_5^2)$ of the heavier tastes given in the column headers from the Goldstone taste ξ_5, in units of temporal lattice spacing, for the naive staggered action on pure gauge ensembles. The first line with the data corresponds to the ensemble with the renormalized anisotropy $\xi = 1$ in Table A.1, second to $\xi = 1.2$, third to $\xi = 1.5$ and fourth to $\xi = 4$.

$\xi_4\xi_5$	$\xi_i\xi_5$	$\xi_i\xi_j$	$\xi_i\xi_4$	ξ_i	ξ_4	1
0.2189(26)	0.2190(19)	0.3056(43)	0.3139(55)	0.3677(95)	0.3680(70)	0.4126(94)
0.1173(28)	0.1446(14)	0.1881(37)	0.2012(29)	0.2208(56)	0.2395(58)	0.2532(64)
0.05302(88)	0.08455(78)	0.0985(29)	0.1215(25)	0.1244(18)	0.1485(24)	0.1496(42)
0.01666(20)	0.04161(43)	0.0473(13)	0.0632(18)	0.0652(20)	0.0802(36)	0.0797(36)

APPENDIX C

FERMION ANISOTROPY TUNING METHODS

We have chosen to use the dispersion relation, Eq. (4.11), as the main method for tuning fermion anisotropy. We have also checked that using the mass ratio method, Eq. (4.12), produces essentially same results. On a pure gauge ensemble, specifically generated for the mass ratio tuning with the volume $16^2 \times 32 \times 64$ and the renormalized anisotropy $\xi = 2$, we have measured the $\eta_{s\bar{s}}$ correlation functions in the τ and z direction. The measurements were performed at the strange quark mass $m_s = 0.073$ and a set of bare fermion anisotropies $\xi_0^f = 1.6$, 1.8, 2 and 2.2. The resulting data: ξ^f defined with Eq. (4.12) as function of the bare fermion anisotropy and the quadratic fit are shown in Fig. C.1. The tuned bare fermion anisotropy determined from the fit is $\xi_0^f = 2.0134(26)$. This value is comparable with the bare fermion anisotropy predicted with the dispersion relation method: $\xi_0^f = 2.009(12)$, and differs from the renormalized anisotropy $\xi = 2$ by only 0.7%. We thus expect that the mass ratio tuning method would produce the bare parameters very close to the dispersion relation method. However, we find the latter one to be more convenient for the following reason. Our spatial volumes are typically minimal, to accommodate the gradient flow and to have $m_\pi L \approx 4$. To get stable fits we need the fit direction to be twice larger than the minimal spatial one in physical units. This means that, similar to the example shown in Fig. C.1, for stability of the mass ratio tuning method we need to generate asymmetric spatial volumes $N_z = 2N_x = 2N_y$ which are, at least, twice more computationally expensive. The dispersion relation tuning method

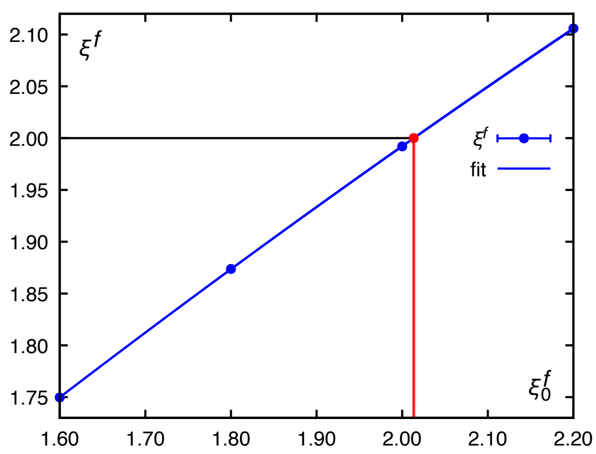

Figure C.1 Determining the bare fermion anisotropy ξ_0^f that corresponds to the renormalized fermion anisotropy $\xi^f = \xi = 2$ with the mass ratio method, where ξ^f is defined as a ratio of masses in lattice units measured in τ and z direction, Eq. (4.12) for the aHISQ action. These measurements were done on a dedicated ensemble with the volume $16^2 \times 32 \times 64$ and $(\beta = 7.04115, \xi_0 = 1.81411)$.

eliminates the need for such asymetric volumes.

APPENDIX D

QUALITY OF THE PARAMETER TUNING FOR THE SPECTRUM CALCULATIONS

In table B.8 we summarize the parameters predicted from the tuning of the fermion anisotropy and strange quark mass measurements, presented in Tables B.1–B.7 and the actual parameters that we used for measuring the pion taste splittings shown in Table B.9. We remind the reader that we tune the strange quark mass $a_\sigma m_s$ and choose the light quark mass as a fixed ratio, in this case, $1/5$. One can notice that the predicted values differ from the ones we actually used, sometimes as much as about 9% for the strange quark mass (naive staggered $\xi = 2$) and about 1.7% for the bare fermion anisotropy (aHISQ $\xi = 1.1$). Our strange quark mass for both naive and aHISQ is about 7-8% lower in the actual runs than the predicted values. Here we explain the reasons for that. The overall project did not progress linearly: as we needed many ensembles, gradient flow and spectrum measurements to tune the parameters of the gauge and fermion action, we started multiple simulations, where possible, before full statistics of the tuning runs was collected. Originally, we used a slightly different value of w_0 and were aiming at the spatial lattice spacing $a_\sigma = 0.16$ fm. As the earlier ensembles turned out to have $a_\sigma \in [0.1662, 0.1667]$, we tried to tune the next ensembles closer to $a_\sigma = 0.1665$ fm value. However, we already started some spectrum measurements with input $\eta_{s\bar{s}}$ mass in lattice units based on the expectation that $a_\sigma = 0.16$ fm. Thus, our strange quark mass is slightly lower than needed. The pion taste splittings at the lowest order are mass independent, so the mistuning of the mass by a small amount should play no role. (Also, one can reinterpret this situation as that we performed the taste splitting measurements with $a_\sigma m_l \simeq 0.184 a_\sigma m_s$ instead of $a_\sigma m_l = 0.2 a_\sigma m_s$.)

For the fermion anisotropy we did not expect that ξ_0^f is almost the same as the renormalized anisotropy ξ for the aHISQ action, *e.g.*, Fig. 5.11. As the expectation was a lower value, similar to the naive staggered action, and it seemed to be confirmed by incomplete statistics, our fermion anisotropy values are also often slightly lower than they should be based on the complete statistics. Overall, the mistuning is quite small, on the level of 1.7% at most, and we believe it does not affect our conclusions.

APPENDIX E

COMPARISONS WITH EXISTING LITERATURE

Our anisotropic setup for calculations in this paper includes the following components: ensemble generation, gradient flow and staggered inverter (naive and aHISQ). To validate our code we reproduced several quantities from the existing literature. In preparation for dynamical aHISQ simulations, we also reproduced some fully dynamical naive staggered simulations.

The pure gauge ensemble generation and gradient flow parts independently reproduce the results of [Borsanyi et al., 2018] in the relevant range of couplings, *e.g.*, Fig. 5.4. To test isolated parts of the code at the early stages of the project we ran various tests. For instance, we generated two pure gauge ensembles with the Wilson gauge action at the parameters of [Namekawa et al., 2001] and compared the plaquette values, Table E.1.

To compare the naive staggered pion spectrum calculations, we generated a pure gauge ensemble at the same parameters as in [Nomura et al., 2004] with the Wilson gauge action and the lattice volume of $12^3 \times 96$. The bare gauge coupling is $\beta = 6/g_0^2 = 5.75$, the bare gauge anisotropy $\xi_0 = 3.136$, the bare fermion anisotropy $\xi_0^f = 2.83$ and the quark mass $a_\sigma m = 0.1$. We measured the same pion tastes as in that reference, and the comparison is reported in Table E.2.

Finally, to test full Rational Hybrid Monte Carlo pipeline, we generated several dynamical 2-flavor naive staggered ensembles of [Levkova et al., 2006], both at zero and finite temperature.

Table E.1 Comparison of the spatial (first line per β value) and temporal (second line) plaquette values with the values from [Namekawa et al., 2001] on two ensembles generated with the Wilson action at the same parameters as in that reference. The first column is the bare gauge coupling $\beta = 6/g_0^2$, second the bare gauge anisotropy, third lattice volume, fourth the number of sweeps (one heatbath and four overrelaxation updates of the full lattice), fifth and sixth are the plaquette values, with those from [Namekawa et al., 2001] being labeled by an asterisk, and seventh the Q value of the Gaussian difference test.

β	ξ_0	$N_\sigma^3 \times N_\tau$	N_{sweep}	$P_{\sigma\sigma}, P_{\sigma\tau}$	$P^*_{\sigma\sigma}, P^*_{\sigma\tau}$	Q
5.8	1.67401280	$16^3 \times 8$	70,000	0.462746(41)	0.462698(75)	0.57
				0.688895(18)	0.688873(33)	0.56
6.51881026	1.75986308	$20^3 \times 40$	50,000	0.5439713(68)	0.5439702(40)	0.89
				0.7454649(27)	0.7454657(19)	0.81

Table E.2 Comparison of pion taste masses with [Nomura et al., 2004]. The parameters of the ensemble are described in the text. The first column lists the taste structure of the measured state, the second column our measurements, the third the results of [Nomura et al., 2004] (labeled with an asterisk) and fourth column the Q value of the Gaussian difference test.

taste	$a_\tau M_\pi$	$a_\tau M_\pi^*$	Q
ξ_5	0.23859(11)	0.23846(10)	0.38
$\xi_4\xi_5$	0.24878(14)	0.24874(12)	0.83
$\xi_i\xi_5$	0.29542(69)	0.29410(40)	0.10
$\xi_i\xi_j$	0.2956(11)	0.29494(48)	0.58

The gauge action is the Wilson action and to match our definition of ξ_0^f, the quark mass value of [Levkova et al., 2006] is multiplied by ξ_0^f. On the two zero-temperature ensembles, we measured the same pion taste, ξ_5 and $\xi_4\xi_5$, masses as in [Levkova et al., 2006]. The comparison is shown in Table E.3. The finite-temperature ensembles were generated at the same parameters as the second, $16^3 \times 64$ ensemble of Table E.3. The only varied parameter is the temporal extent N_τ. The comparison for the chiral condensate $\langle\bar{\psi}\psi\rangle$ is shown in Table E.4 as well as in Fig. E.1. The line is not a fit but spline interpolation to guide the eye. We generated more finite-temperature ensembles to have denser temperature coverage. Since temperature is $T = 1/(a_\tau N_\tau)$ with a_τ fixed in this case, there is no need to convert to physical units for the comparison purposes. Therefore the x-axis of Fig. E.1 is in units of $1/N_\tau$.

Table E.3 The masses of the ξ_5 (first line per β value) and $\xi_0\xi_5$ (second line) pion tastes compared with the results from [Levkova et al., 2006]. The first column is the gauge coupling $\beta = 6/g_0^2$, second the bare gauge anisotropy, third the bare fermion anisotropy, fourth the bare quark mass, fifth the lattice volume, sixth the number of configurations used for measurements, seventh our results for the pion masses, eighth the results from [Levkova et al., 2006] (labeled with an asterisk) and ninth the Q value of the Gaussian difference test.

β	ξ_0	ξ_0^f	$a_\sigma m$	$N_\sigma^3 \times N_\tau$	N_{conf}	$a_\tau M_\pi$	$a_\tau M_\pi^*$	Q
5.425	1.5	3	0.0375	$16^3 \times 32$	1,200	0.31303(11)	0.31309(28)	0.84
						0.4687(13)	0.4605(37)	0.04
5.3	3	3	0.024	$16^3 \times 64$	745	0.112641(46)	0.11280(51)	0.76
						0.14137(19)	0.1410(11)	0.74

For the chiral condensate comparison we note the following. The values were not tabulated

Table E.4 Comparison of the chiral condensate with the results of [Levkova et al., 2006]. The parameters of the ensembles are the same as for the second ensemble in Table E.3, except of varying N_τ, listed in the first column. The second column is the number of trajectories (with one condensate measurement per trajectory), third our values for $\langle\bar{\psi}\psi\rangle$ in lattice units, fourth values from [Levkova et al., 2006] (labeled by an asterisk) and fifth the Q value of the Gaussian difference test. The values from this table are plotted in Fig. E.1.

N_τ	N_{traj}	$\langle\bar{\psi}\psi\rangle$	$\langle\bar{\psi}\psi\rangle^*$	Q
8	2,600	0.03191(11)	0.03184(00)	0.52
10	5,090	0.04264(12)	-	-
12	2,600	0.05858(16)	0.05876(17)	0.44
14	10,095	0.09803(55)	-	-
16	10,095	0.18728(43)	0.18729(92)	0.99
18	9,970	0.20490(45)	-	-
20	5,095	0.20955(43)	0.20987(43)	0.60
24	2,600	0.21174(34)	0.21051(47)	0.03
32	4,795	0.21171(24)	-	-
64	6,980	0.21222(14)	0.21171(26)	0.08

in [Levkova et al., 2006] but only plotted in Fig. 9 of that reference. The Encapsulated PostScript (EPS) file of the figure is available in the arXiv version of the paper. As the EPS file is an ASCII file with a collection of drawing commands [Adobe Systems Incorporated, 1992], we can reconstruct the location of the points from it. That particular EPS file uses coordinates scaled to $[0, 1]$ range with the accuracy of 0.0001. The horizontal axis of Fig. 9 of [Levkova et al., 2006] covers $[0, 0.4]$ range (temperature in GeV) and the vertical $[0, 0.3]$ ($\langle\bar{\psi}\psi\rangle$ in lattice units). This means that we can reconstruct the condensate values and errorbars from the figure with the accuracy of 0.00003. This is enough for the purposes of this paper. The other two aspects relevant for the comparison are: (a) [Levkova et al., 2006] used the R algorithm, that has integration step size dependence, while we used today's standard Rational Hybrid Monte Carlo algorithm, (b) for computational efficiency the MILC code works with scaled fermion matrix $2M$ rather than M, so our values in Table E.4 are twice the values computed by the MILC code, to match the [Levkova et al., 2006] standard normalization.

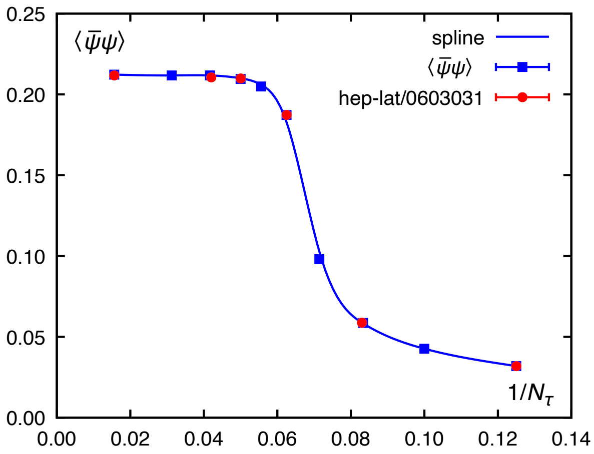

Figure E.1 Comparison of the chiral condensate $\langle\bar{\psi}\psi\rangle$ computed in [Levkova et al., 2006] (red points) and in our test runs at the same parameters, summarized in Table E.4 (blue points). Blue line is a spline interpolation to guide the eye.

APPENDIX F

TESTING THE AHISQ FERMION FORCE

Apart from the tests described in Appendix E, we performed other tests of the Rational Hybrid Monte Carlo pipeline. We ran the full aHISQ RHMC, but with the smearing coefficients set to 0, to reproduce the naive staggered results. Finally, to independently test the aHISQ fermion force calculation, we compared the force evaluated by the code in the way described in Sec. 4.4, where it is denoted by $f^F_{x,\mu}$ and defined in Eq. (4.19), with the computation of the force done by approximating the group derivative of the action with a forward finite difference:

$$\tilde{f}^F_{x,\mu} = T_A \frac{d}{ds} S_f \left[e^{isT_A} U_{x,\mu} \right] \Big|_{s=0} \simeq T_A \frac{S_f \left[e^{isT_A} U_{x,\mu} \right] - S_f \left[U_{x,\mu} \right]}{s}, \tag{F.1}$$

for small s. The norm of the difference between the approximation (F.1) and the actual force calculation (4.19) defined with the Frobenius measure as

$$|| f^F_{x,\mu} - \tilde{f}^F_{x,\mu} || = \sqrt{\mathrm{Tr}[(f^F_{x,\mu} - \tilde{f}^F_{x,\mu})^\dagger (f^F_{x,\mu} - \tilde{f}^F_{x,\mu})]} \tag{F.2}$$

is shown in Fig. F.1 for s ranging from $1/2$ down to $1/2048$ together with a linear fit.

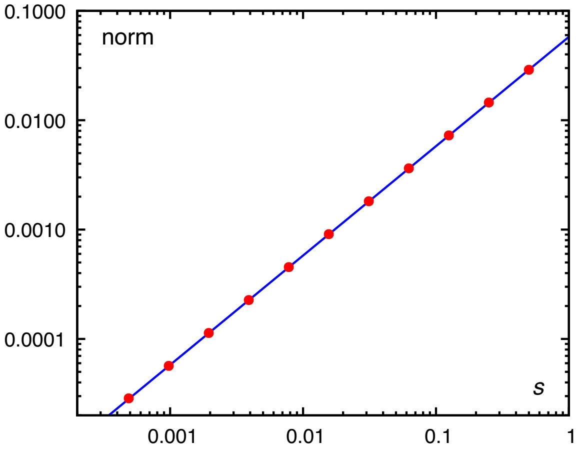

Figure F.1 The Frobenius norm of the difference, defined in Eq. (F.2) of the aHISQ force as calculated directly in the MILC code, Eq. (4.23), and from the finite difference (F.1) with s ranging from $1/2$ down to $1/2048$. The measurements are on a 6^4 lattice, at site (1,0,0,0), in the positive τ direction. The line represents a linear fit without a free term.